



HAL
open science

Oxidation, pickling and over-pickling mechanisms of high silicon alloyed steel grades.

Amine Alaoui Mouayd

► **To cite this version:**

Amine Alaoui Mouayd. Oxidation, pickling and over-pickling mechanisms of high silicon alloyed steel grades. . Chemical and Process Engineering. Université Pierre & Marie Curie - Paris 6, 2014. English. NNT: . tel-01360945

HAL Id: tel-01360945

<https://theses.hal.science/tel-01360945>

Submitted on 6 Sep 2016

HAL is a multi-disciplinary open access archive for the deposit and dissemination of scientific research documents, whether they are published or not. The documents may come from teaching and research institutions in France or abroad, or from public or private research centers.

L'archive ouverte pluridisciplinaire **HAL**, est destinée au dépôt et à la diffusion de documents scientifiques de niveau recherche, publiés ou non, émanant des établissements d'enseignement et de recherche français ou étrangers, des laboratoires publics ou privés.

Université Pierre et Marie Curie

Spécialité: Génie des Procédés et Technologies Avancées

Laboratoire Interfaces et Systèmes Electrochimiques

ArcelorMittal Maizières Research SA

Oxidation, pickling and over-pickling mechanisms of high silicon alloyed steel grades

Par Amine Alaoui Mouayd

Thèse de Doctorat

Présentée et soutenue publiquement le 30/01/2014

Devant un jury composé de :

Eliane Sutter, Professeure

Directeur de thèse

Bernard Tribollet, Directeur de recherche

Directeur de thèse

Ricardo Nogueira, Professeur

Rapporteur

Philippe Refait, Professeur

Rapporteur

Farzaneh Arefi-Khonsari, Professeur

Examineur

Alexey Koltsov, Ingénieur-Docteur

Examineur

Kevin Ogle, Professeur

Examineur

*A mes parents
A mes deux frères
A mes enseignants*

Remerciements

Je tiens à remercier mes directeurs de thèse Eliane Sutter et Bernard Tribollet ainsi que mon tuteur en entreprise Alexey Koltsov pour leur encadrement tout au long de la thèse. Grâce à leurs expertises complémentaires et leur générosité à me les transmettre, j'ai approfondi mes connaissances en métallurgie et électrochimie et surtout bien assimilé les approches scientifiques et industrielles lors de la rédaction des différents rapports et des présentations orales.

Je remercie chaleureusement les professeurs Ricardo Nogueira et Philippe Refait d'avoir accepté de juger mon travail de thèse en tant que rapporteurs et les professeurs Kevin Ogle et Farzaneh Arefi-Khonsari en tant qu'examineurs.

Je remercie ArcelorMittal et l'agence nationale de recherche et technologie pour le financement de ma thèse CIFRE.

Pour la période de la thèse passée au centre de recherche « Process » d'ArcelorMittal à Maizières-lès-Metz, je tiens à remercier Patrick Hug, Pascal Gardin, Didier Loison et Michel Picard pour leur accueil dans le département « Process Engineering ». Je remercie Alexey Koltsov mon tuteur ainsi que les autres collègues qui ont participé dans ce travail : Michel Picard et Evangeline Ahtoy pour la documentations et les explications sur la partie « oxydation » et Sophie Jacques pour son rapport bibliographique sur la partie « décapage », Marie-Christine Theyssier pour sa participation dans les discussions lors des revues de projet, Mario Crocenco pour la préparation des alliages, Soline de Diesbach et Patrice Alexandre pour l'oxydation des échantillons, Françoise Broquedis, Marie-José Cornu et Sébastien Cremel pour les caractérisations des échantillons, Daniel Bettinger et Christophe Mougel pour les mesures de rugosité, Marie-Claire Succi et Alain Galparoli pour les démarches administratives ainsi que tous les autres collègues qui m'ont habilité sur les différents postes de travail et aider d'une manière plus générale.

Pour la période de la thèse effectuée au Laboratoire Interfaces et Systèmes Electrochimiques à Paris. Je voudrais remercier chaleureusement le directeur du Laboratoire François Huet pour son accueil, mes deux directeurs de thèse Eliane Sutter et Bernard Tribollet pour leur encadrement ainsi que tous les collègues du laboratoire qui ont participé à ce travail : Axel Desnoyer de Marbaux et Daniel Rose pour la préparation des électrodes, Françoise Pillier pour les images MEB et Damien Bricault pour l'assistance en informatique et tous les autres permanents du laboratoire.

Enfin, je n'oublierai pas de remercier les collègues avec qui j'ai sympathisé et qui m'ont rendu service à plusieurs reprises : Patrice, Gabriel, Abdeldjalil, Stéphane, Benjamin, Maryl, Karim, Fanny, Claire... du côté d'ArcelorMittal et Zineb, Mohamed, Sameer, Alain, Nizar, Wafaa, Yasser et les autres non permanents du laboratoire.

I would like to thank Professor Mark Orazem for hosting me in his research team in the chemical engineering department of the University of Florida and his contributions to the interpretation of the impedance results. A special thank to Christopher for his help during my stay in Gainseville and to the other members of professor Orazem's team for their sympathy.

Summary

GENERAL INTRODUCTION	11
I. LITERATURE REVIEW	15
I. 2. Oxidation and pickling in steelmaking process	17
I. 2. 1. Overview of steelmaking process	17
I. 2. 2. The hot strip mill.....	18
I. 2. 3. The pickling baths.....	20
I. 3. Oxidation of steel	21
I. 3. 1. Steel substrate properties	21
I. 3. 1. 1. Low carbon steel	21
I. 3. 1. 2. Silicon alloyed steel	21
I. 3. 2. Oxidation conditions	21
I. 3. 2. 1. Oxidation in the Hot Strip Mill.....	21
I. 3. 2. 2. Oxidation in a pilot furnace	22
I. 3. 3. Oxidation of low carbon steel	23
I. 3. 3. 1. Oxidation kinetics	23
I. 3. 3. 2. LCS oxidation mechanism.....	24
I. 3. 4. Oxidation of silicon alloyed steels.....	24
I. 3. 4. 1. Influence of silicon on the kinetics of scale growth	24
I. 3. 4. 2. Influence of silicon on oxidation mechanism	26
I. 4. Scale and metal oxides properties	27
I. 4. 1. Hot strip mill (HSM) scales	27
I. 4. 1. 1. Low carbon steel (LCS) scales	27
I. 4. 1. 2. Silicon alloyed steel (SiAS) scales	28
I. 4. 2. Model scales.....	28
I. 4. 2. 1. LCS model scales.....	28
I. 4. 2. 2. Iron oxides properties	29
I. 4. 2. 3. SiAS model scales.....	30
I. 5. Pickling and over-pickling	32
I. 5. 1. Pickling of hot mild steels.....	33
I. 5. 1. 1. Pickling conditions.....	33
I. 5. 1. 2. Influence of pickling parameters on pickling time	34
I. 5. 2. Pickling mechanism of low carbon steels	35
I. 5. 2. 1. Pickling steps of LCS.....	35
I. 5. 2. 2. Pickling reactions of LCS	38
I. 5. 2. 3. Iron oxides dissolution.....	40
I. 5. 3. Effect of Silicon on pickling mechanism.....	41
I. 5. Conclusions.....	42
II. 1. Elaboration of steel grades samples.....	47
II. 1. 1 Steel chemical composition	47
II. 2. 2. Steel grains size	48

II. 2. Oxidation of steels	48
II. 2. 1. Oxidation experiments.....	48
II. 2. 2. Oxidation methods.....	50
II. 3. Scale Characterization after oxidation.....	51
II. 3. 1. Optical observations	51
II. 3. 2. Spectrometric methods	51
II. 4. Scale dissolution characterization	51
II. 4. 1. Electrochemical measurements	52
II. 4. 1. 1. Electrochemical set-up	52
II. 4. 1. 2. Electrochemical methods.....	55
II. 4. 2. ICP-AES setup and method.....	62
II. 5. Scale characterization after pickling and over-pickling.....	65
III. OXIDATION AND SCALE CHARACTERIZATION OF SILICON ALLOYED STEELS.....	67
III. 1. Introduction	69
III. 2. Steel substrate properties.....	70
III. 3. Oxidation mechanisms	70
III. 3. 1. Low carbon steel oxidation	70
III. 3. 1. 1. Oxidation kinetics	70
III. 3. 1. 2. Oxidation mechanism.....	72
III. 3. 2. Effect of Silicon content on oxidation.....	72
III. 3. 2. 1. Oxidation kinetics	72
III. 3. 2. 2. Oxidation mechanism.....	74
III. 4. Scale characterization	75
III. 4. 1. Low carbon steel scale properties	75
III. 4. 2. Silicon steel scales properties.....	76
III. 5. Conclusions.....	81
IV. PICKLING AND OVER-PICKLING MECHANISMS OF LOW CARBON STEEL.	83
IV. 1. Introduction.....	85
IV. 2. Model scale characteristics before pickling.....	85
IV. 3. Electrochemical dissolution of scale.....	86
IV. 3. 1. Corrosion potential E_{corr}	86
IV. 3. 2. Corrosion current I_{corr}	87
IV. 3. 2. 1. Tafel curves.....	87
IV. 3. 2. 2. Corrosion current evolution during scale dissolution	88
IV. 3. 3. Electrochemical Impedance Spectroscopy EIS.....	89
IV. 3. 3. 1. EIS diagrams	89

IV. 3. 3. 2. Evolution of charge transfer resistance R	90
IV. 3. 3. 3. Evolution of CPE parameters	91
IV. 3. 3. 4. Evolution of effective capacitance	92
IV. 4. Total dissolution of scale	94
IV. 5. Pickling and over-pickling mechanisms	95
IV. 5. 1. Pickling thermodynamics.....	95
IV. 5. 2. Pickling steps and reactions	96
IV. 5. 3. Over-pickling reactions.....	98
IV. 6. Influence of some parameters on pickling and O-P mechanism of LCS scales	99
IV. 6. 1. Scale composition and morphology	100
IV. 6. 1. 1. Influence of hematite on pickling	100
IV. 6. 1. 2. Pickling of an industrial scale	101
IV. 6. 2. Influence of acid concentration.....	102
IV. 6. 3. Influence of pickling bath temperature	102
IV. 6. 4. Influence of a cathodic applied potential	102
IV. 7. Steel surface after pickling and over-pickling.....	105
IV. 7. 1. Steel surface after insufficient pickling	105
IV. 7. 2. Steel surface after long over-pickling:	105
IV. 8. Conclusions.....	107
V. PICKLING AND OVER-PICKLING MECHANISMS OF HIGH SILICON ALLOYED STEEL GRADES.....	109
V. 1. Introduction	111
V. 2. Model scale characteristics before pickling	111
V. 3. Electrochemistry of scale dissolution.....	113
V. 3. 1. Corrosion potential E_{corr}	113
V. 3. 2. Corrosion current density I_{corr}	115
V. 3. 2. 1. Current-potential curves	115
V. 3. 2. 1. Evolution of the corrosion current density	117
V. 4. Total dissolution of scale.....	120
V. 4. 1. Total dissolution rate (TDR)	121
V. 4. 2. Electrochemical contribution in scale dissolution.....	122
V. 5. Pickling and over-pickling (O-P) mechanism.....	122
V. 5. 1. Pickling steps and reactions	123
V. 5. 2. Over-pickling steps and reactions	123
V. 6. Influence of some parameters on pickling and O-P mechanism.....	125
V. 6. 1. Scale morphology and composition	126
V. 6. 1. 1. Influence of fayalite morphology	126
V. 6. 1. 2. Behaviour of industrial scale	126
V. 6. 2. Influence of pickling bath temperature	127

V. 6. 3. Influence of acid concentration	128
V. 7. Steel surface after pickling and over-pickling	129
V. 7. 1. Steel surface after insufficient pickling	129
V. 7. 2. Steel surface after over-pickling.....	130
V. 8. Conclusions	133
GENERAL CONCLUSION.....	135
ANNEXES.....	141
REFERENCES	149

General introduction

One of the main activities of ArcelorMittal Group is the fabrication of flat carbon steels for the automotive industry, construction and packaging applications. Continuous research and development are held on the fabrication process of these steels to improve their quality and compatibility with the final product requirements.

Three priorities immerge in these R&D projects: cleanness of the steel strip (reduction of undesirable inclusions), thermo-mechanical properties of the steel strip and physico-chemical properties of the steel surface.

One of the major steps in fabrication of flat carbon steel is the hot strip mill. During this step, steel surface is in contact with humid air at high temperatures. These conditions favour steel surface corrosion and the formation of an oxide layer commonly called “scale”. The high temperature corrosion is commonly called “Oxidation” and has a negative effect on the steel surface properties.

This scale is first removed mechanically (de-scaling) then dissolved in acidic solutions to recover a clean and smooth steel surface and avoid defects formation and surface heterogeneities in the final product. This step is commonly called “Pickling” and implicates also “Over-pickling” which corresponds to the corrosion of the steel substrate.

Pickling of low carbon steel grades and low alloyed steel grades is efficient in standard pickling lines. The empirical studies on these grades were sufficient to optimize the pickling process and recover a good quality surface. On fellow fundamental pickling and over-pickling mechanisms of these samples were proposed in the literature.

Recently, new grades of Alloyed High Strength Steels (AHSS) were developed for their improved mechanical properties. These grades are highly alloyed with chemical elements such as silicon and aluminium forming in reheating furnace and hot strip mill mixed oxides at steel/scale interface and infiltrations in the steel substrate. These newly formed mixed oxides resist to pickling and can cause defects at steel surface if the pickling or even over-pickling time is not sufficient.

The PhD is a part of a research project of ArcelorMittal Global R&D to study and improve the efficiency of pickling of AHSS. In parallel with more applied studies of the pickling process, the PhD aim was to understand the fundamentals of pickling and over-pickling mechanisms of these steels.

Two representative steel grades were chosen in this work: A low carbon steel with very low alloying element content used as a reference and a silicon alloyed steel grade representing the AHSS.

In the first chapter, an overview of the flat carbon steel fabrication process and a focus on the hot strip mill and pickling baths steps are developed. The literature related to oxidation and pickling of low carbon steel and silicon steel grades was summarized and the few proposed mechanisms were presented.

In the second chapter, the different experimental set-ups and methods used in this work are presented. Some of these experimental protocols and methods were inspired from the literature and some were developed and adapted for this study. For oxidation study, scale growth kinetics was followed by thermo-gravimetric analysis and the resulting scale well characterized by crossing different high resolution techniques (scanning electrons microscopy, Raman spectroscopy...). For pickling and over-pickling experiments, a new electrode adapted for scale was developed. The pickling and over-pickling study combined, on one side, electrochemical methods such as open circuit potential, current-potential curves and electrochemical impedance spectroscopy (EIS) to quantify the electrochemical dissolution and model scale/solution interface, and on the other side, a total dissolution kinetic method using the inductively coupled plasma-atomic emission spectroscopy (ICP-AES) to evaluate the electrochemical and chemical contributions in pickling and over-pickling. The surface roughness after over-pickling was explored with interferometric analysis.

In the third chapter, oxidation of low carbon steel and a high silicon alloyed grades at hot strip mill conditions was studied. Oxidation mechanisms with their kinetic and phenomenological aspects for both grades were proposed and compared to the literature where different silicon content and oxidation conditions were studied.

In the fourth and fifth (last) chapters, representative model and industrial scales of low carbon steel grades and high alloyed silicon grades with different scale compositions and morphologies were chosen from the samples studied in the “oxidation” part of this work to study their pickling and over-pickling mechanisms.

After the interpretation and combination of the significant results of the complementary experimental methods already cited, pickling and over-pickling mechanisms with their different aspects (phenomenology, thermodynamics, kinetics and reactions) were proposed for model scales and industrial scales of the chosen grades and compared with the literature. The effect of some pickling parameters (temperature, acid concentration and applied potential) on pickling and over-pickling kinetics and steel surface was also explored.

In the general conclusion, the main results of this work are summarized and some perspectives for this research are proposed.

I. Literature review

Summary

I. 1. Introduction	17
I. 2. Oxidation and pickling in steelmaking process	17
I. 2. 1. Overview of steelmaking process	17
I. 2. 2. The hot strip mill.....	18
I. 2. 3. The pickling baths.....	20
I. 3. Oxidation of steel	21
I. 3. 1. Steel substrate properties	21
I. 3. 1. 1. Low carbon steel	21
I. 3. 1. 2. Silicon alloyed steel	21
I. 3. 2. Oxidation conditions	21
I. 3. 2. 1. Oxidation in the Hot Strip Mill.....	21
I. 3. 2. 2. Oxidation in a pilot furnace	22
I. 3. 3. Oxidation of low carbon steel	23
I. 3. 3. 1. Oxidation kinetics	23
I. 3. 3. 2. LCS oxidation mechanism.....	24
I. 3. 4. Oxidation of silicon alloyed steels.....	24
I. 3. 4. 1. Influence of silicon on the kinetics of scale growth	24
I. 3. 4. 2. Influence of silicon on oxidation mechanism	26
I. 4. Scale and metal oxides properties	27
I. 4. 1. Hot strip mill (HSM) scales	27
I. 4. 1. 1. Low carbon steel (LCS) scales	27
I. 4. 1. 2. Silicon alloyed steel (SiAS) scales	28
I. 4. 2. Model scales.....	28
I. 4. 2. 1. LCS model scales.....	28
I. 4. 2. 2. Iron oxides properties	29
I. 4. 2. 3. SiAS model scales.....	30
I. 5. Pickling and over-pickling	32
I. 5. 1. Pickling of hot mild steels.....	33
I. 5. 1. 1. Pickling conditions.....	33
I. 5. 1. 2. Influence of pickling parameters on pickling time	34
I. 5. 2. Pickling mechanism of low carbon steels	35
I. 5. 2. 1. Pickling steps of LCS.....	35
I. 5. 2. 2. Pickling reactions of LCS	38
I. 5. 2. 3. Iron oxides dissolution.....	40
I. 5. 3. Effect of Silicon on pickling mechanism.....	41
I. 5. Conclusions	42

I. 1. Introduction

The aim of this PhD is to understand the pickling mechanism and the influence of high silicon content in steel on both oxidation and pickling. As an industrial subject, part of related literature comes from steelmaking companies with a focus on technical and practical aspects of industrial samples.

In this literature review, a state of the art of published works on oxidation and pickling is presented in three parts:

- Industrial context of oxidation and pickling
- Literature review on oxidation of steel
- Literature review on pickling and over pickling

I. 2. Oxidation and pickling in steelmaking process

I. 2. 1. Overview of steelmaking process

Steelmaking process is divided into two main parts: hot and cold mills.

The hot mill starts from the raw materials and finishes at the hot coils (Figure I. 1). The main steps are the following:

- Preparation of raw materials and homogenization of ores
- Preparation of coke by coal burning
- Elaboration of cast iron in blast furnace
- De-sulfuration of cast iron
- De-carburation by pure oxygen blowing
- Continuous casting producing slabs with a typical thickness of 250 mm and a mass between 10 to 30 t
- Hot strip mill producing steel strips rolled in coils (thickness 1.5 to 12 mm)

The cold factory is divided into five main parts:

- Pickling baths: remove scale formed during hot strip mill step
- Cold strip mill: produces strips with thickness 0.5 to 1.2 mm
- Annealing: in bells or continuous line, re-crystallize the structure of steel modified during rolling operations
- Coatings: with zinc for automotive and household electrical appliances, with chromium and tin for packaging.

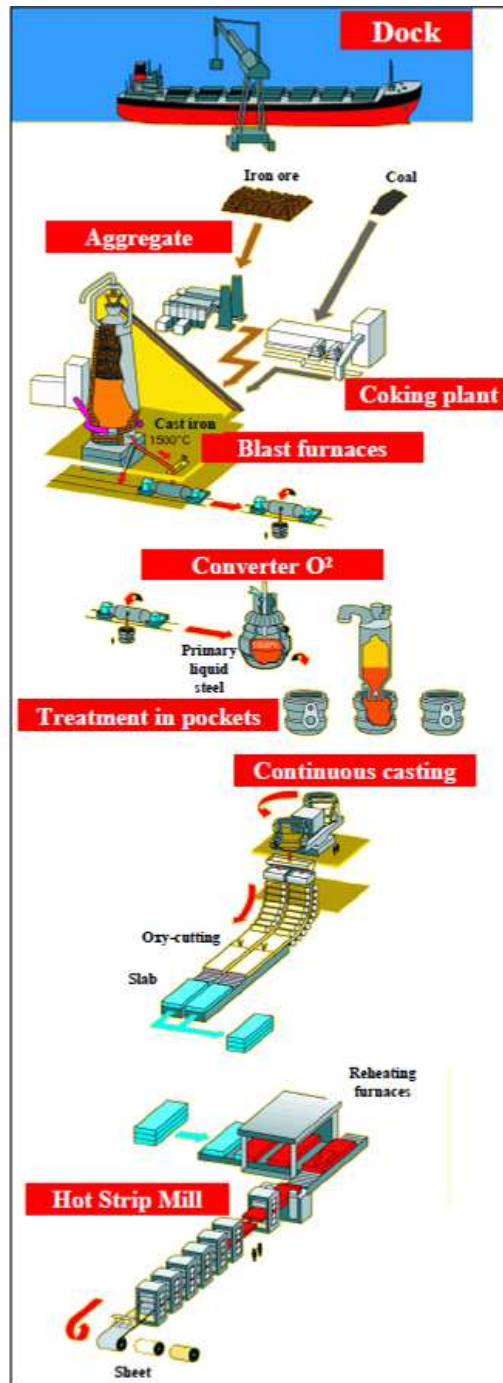


Figure I. 1: Hot Mill scheme of Fos-sur-Mer plant in France [1].

I. 2. 2. The hot strip mill

The Hot Strip Mill (HSM) is the last step of the hot mill (Figure I. 2).

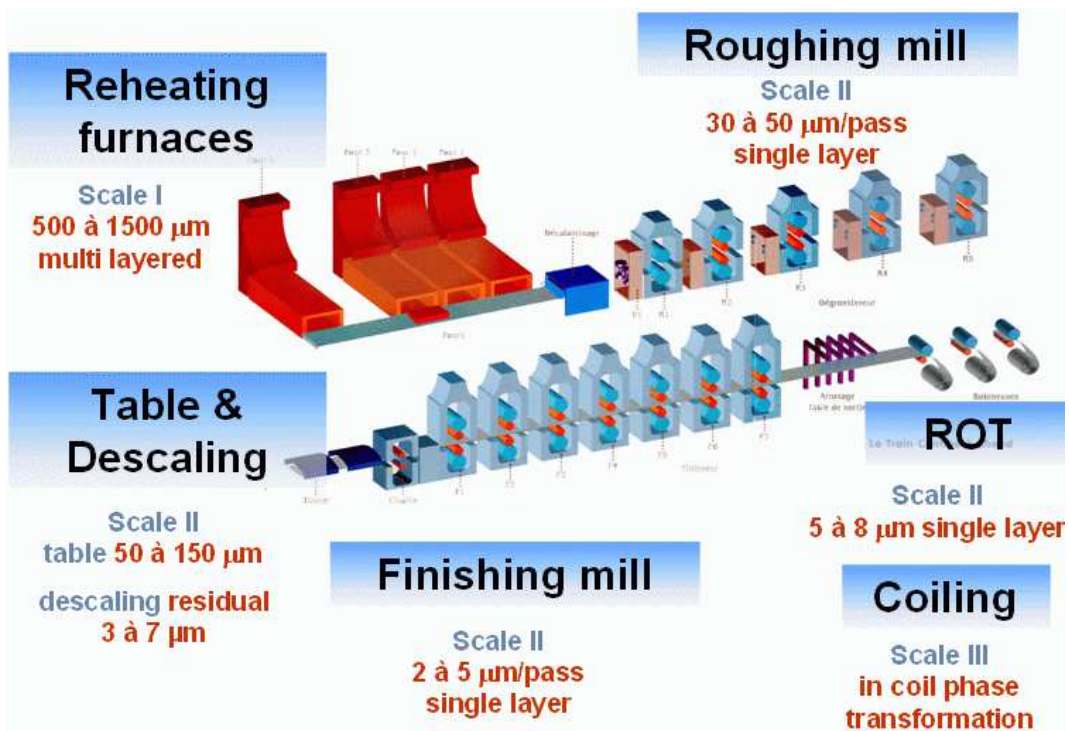


Figure I. 2: General Scheme of a Hot Strip Mill steps [2].

It transforms steel slabs of around 250 mm thickness into coiled steel sheets of 1.5 to 5 mm by a thermo-mechanical treatment in 6 main steps:

- Reheating furnace: the slab is heated for nearly 3 hours at 1200°C to have a homogenous metallurgical structure and chemical composition. An oxide layer called primary scale of 500 to 1000 µm thickness is formed on slab surface.
- RSB de-scaling (Roughing Scale Breaker): Primary scale formed in the reheating furnace is cracked and removed with high pressured water (150 bar) projected from nozzles surrounding the slabs. This step is necessary to avoid scale infiltration into metal surface at high temperature. Nevertheless, such infiltration can take place due to high grain boundaries oxidation or melted mixed oxides of some alloying elements. In this case the infiltrated oxides will appear in the rolled sheets as inherited defects.
- Roughing Mill: the de-scaled slab passes through a first stand of vertical rollers to control its width, then through 5 roughing mill stands with horizontal rollers. A de-scaling ramp is placed between stands to remove the growing scale and recover a better surface. At the exit, the slab is 30 to 40 mm thick at 1100°C and covered with a 600 to 100 µm thick scale.
- Crop shear and FSB de-scaling (Finishing Scale Breaker): the slab extremities deformed in the roughing mill are cut and the scale is removed to avoid rolled-in-scale defects in the finishing mill.

- Finishing Mill: Made of 5 or 7 identical stands. Every stand is composed of 2 work-rolls and 2 support-rolls to limit deformation under loading. The strip final thickness is 1.5 to 5 mm. After the last stand the strip is cooled on a table before being coiled.
- Coiling: The final steel sheet of 1.5 to 5 mm thickness and 700 m long is coiled for storage.

I. 2. 3. The pickling baths

Pickling is an important step of the steelmaking process. It is the interface between the hot factory and the cold factory, more precisely between hot rolling and cold rolling. It is the first step where the steel surface is revealed.

Pickling line can be divided into three main parts (Figure I. 3)

- An entrance section: black steel sheets covered with scale are de-coiled, welded and introduced in the accumulator where they are passed through crossed rollers (S form) to break scale.
- The pickling baths: steel sheets are immersed in successive acid baths containing high concentrated acid solutions (50 to 150 g/L for HCl and until 200 g/L for H₂SO₄) at high temperatures (50 to 90°C) to dissolve scale as fast as possible (< 1min). Sometimes steel corrosion inhibitors are added to limit over-pickling.
- Exit section: the pickled sheet is inspected, cut and coiled. If the surface quality does not meet customer standards, the coil can be put at the pickling entrance to be re-pickled.

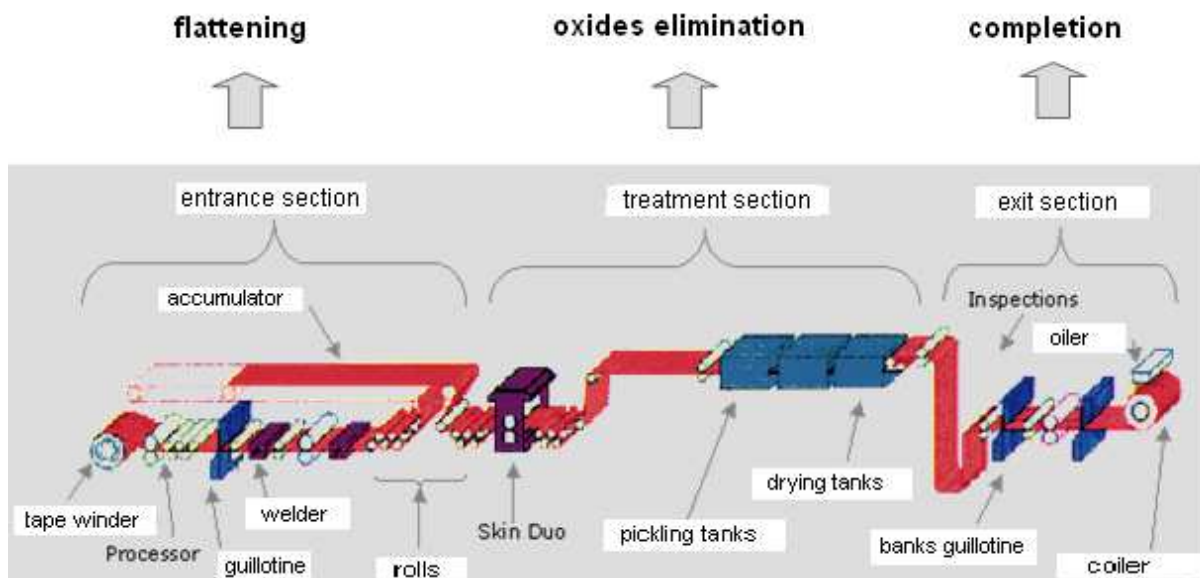


Figure I. 3: Scheme of a Pickling line.

I. 3. Oxidation of steel

A literature review on steel properties and thermal oxidation of low carbon and silicon steels simulating the hot strip mill conditions is presented in this section.

I. 3. 1. Steel substrate properties

The low carbon steels are often used as reference samples for oxidation and pickling studies of alloyed steels.

I. 3. 1. 1. Low carbon steel

Low carbon steels are soft and elastic; their composition is close to pure iron which makes them very corrodible. They are used mainly in packaging applications with protective coatings [3, 4].

I. 3. 1. 2. Silicon alloyed steel

Silicon is present in Alloyed High Strength Steels (AHSS) to improve their mechanical and corrosion resistance, as well as in electrical steels to improve the electrical resistivity, which is an important property for applications as the core material of electromagnetic devices such as motors [5-9].

I. 3. 2. Oxidation conditions

The thermal oxidation of steel takes place when the metallic surface is in contact with an atmosphere containing O_2 or H_2O at high temperatures. The oxide layer formed is called commonly scale [10].

Oxidation must not be confused with rusting which happens at low temperatures, takes longer time and produces iron hydroxides.

I. 3. 2. 1. Oxidation in the Hot Strip Mill

In the Hot Strip Mill, the thermal and atmospheric conditions favorable for scale formation are present. In addition to high temperature and humid air, the mechanical forces applied by rollers and de-scaling water nozzles on the growing scale modify its morphology continuously [11-14].

Steel surface follows a thermo-mechanical cycle during annealing. The steel sheet is globally cooled with temperature drops and scale loss at rollers. Scale growth occurs in passages between rollers (Figure I. 4).

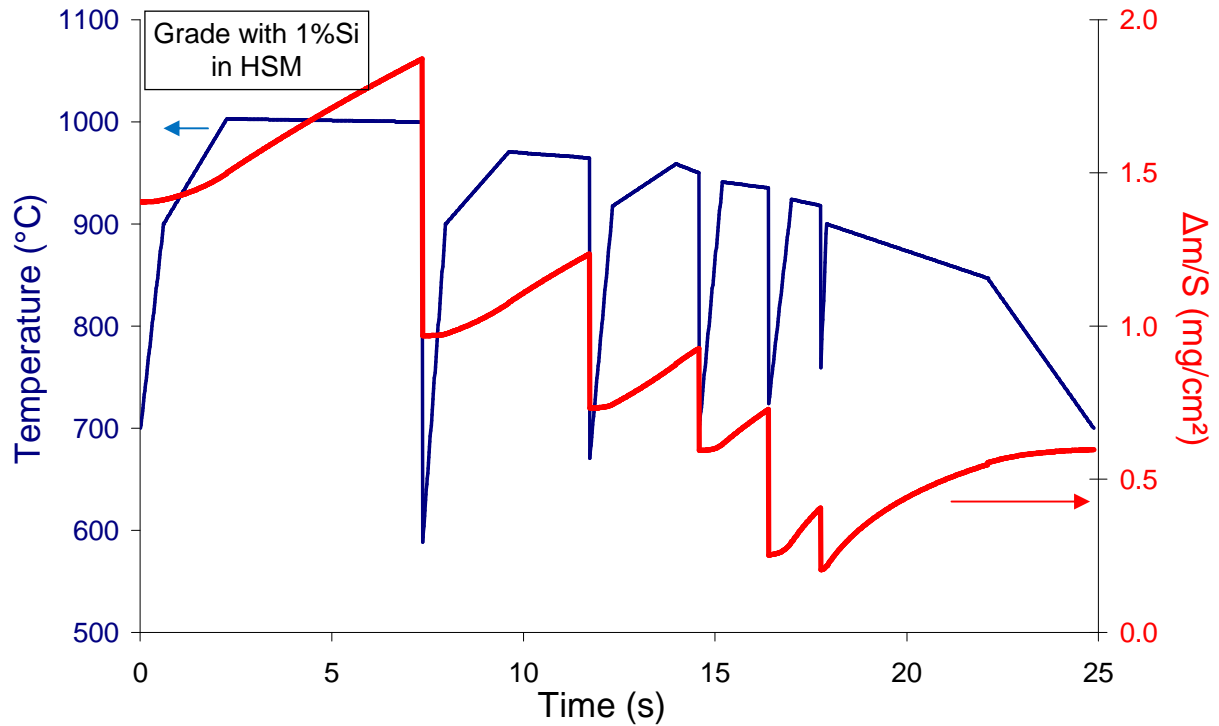


Figure I. 4: An example of modeling of oxidation in a hot strip mill of a steel containing 1%wt. Si [1].

In industrial conditions, at the exit of the hot strip mill, scales thickness varies from 5 to 20 μm . Chemistry and morphology of industrial scales are described in the section I. 4.

I. 3. 2. 2. Oxidation in a pilot furnace

In a pilot furnace, the mechanical effect on scale growth is absent. Only the heat cycle and oxidizing atmosphere are controlled, the furnace can be equipped with a thermo-gravimetric analyzer to study oxidation kinetics. Model scales are elaborated in pilot furnaces or thermo-gravimetric devices [15].

The literature review about the oxidation process and the resulting scale characteristics will be restricted to low carbon and silicon alloyed steel grades oxidized at high temperatures simulating the hot strip mill conditions.

I. 3. 3. Oxidation of low carbon steel

The oxidation of low carbon steel (LCS) and the characterization of the resulting scale were widely studied and its mechanism well defined.

I. 3. 3. 1. Oxidation kinetics

As oxidation is a reaction of oxygen and metal surface to form adherent oxides, the best method used to identify its kinetic profile is to follow the mass gain due to oxygen versus time during oxidation. If the curve fits a mathematical law, the extraction of kinetic parameters is then possible.

A set of mathematical laws for oxidation kinetics exists in literature: linear, parabolic, linear-parabolic, para-linear, logarithmic and sigmoid [16-18].

If no kinetic law can be extracted, we talk about chaotic or catastrophic scale growth.

Oxidation kinetic model and parameters depend on steel grade, oxidation temperature and atmosphere composition.

In low alloyed steel grades, the content of alloying elements is so low that their influence can be neglected. During oxidation at high temperatures only iron and its oxides are considered.

Scale growth kinetics for low alloyed steel grades obeys a mixed law depending on the oxidation stage. A short linear oxidation rate is observed at the beginning of oxidation followed by a longer parabolic rate [19-25].

- The first linear step:

$$(\Delta m / S) = k_l . t \quad (\text{I. 1})$$

- The parabolic step:

$$(\Delta m / S)^n = k_p . t \quad (\text{I. 2})$$

$\Delta m / S$: Mass gain for surface unit

k_l : Linear constant

k_p : Parabolic constant

t: oxidation time

n: parabolic power, $n > 1$ and $n = 2$ for long oxidation times

I. 3. 3. 2. LCS oxidation mechanism

The first linear period corresponds to the oxidation and de-carburation of the metallic surface of steel in an oxygen rich atmosphere (no limitation by gas supply) until the coverage of the entire metallic surface with iron oxide [26-28].

During the parabolic growth period, iron cations Fe^{2+} must diffuse through the newly formed wüstite $Fe_{1-x}O$ layers [29-32]. The vacancies of the non stoichiometric wüstite host the Fe^{2+} while diffusing to scale surface to react with the oxidizing atmosphere [10, 19-21, 23].

I. 3. 4. Oxidation of silicon alloyed steels

The elaboration of new silicon alloyed steel grades and the difficulties to pickle them triggered many recent studies and interest on the effect of silicon on oxidation kinetics and final scale morphology based on. Some of these studies proposed some oxidation mechanisms for silicon alloyed samples but were limited to medium silicon alloyed grades and/or did not correspond completely to the Hot Strip Mill conditions [1, 33-43].

I. 3. 4. 1. Influence of silicon on the kinetics of scale growth

The effect of silicon on scale growth rate profile depends mainly on silicon content and oxidation temperature and the final mass gain depends on oxidation duration. Two main scale growth regimes are observed depending on oxidation temperature [1].

For oxidation temperatures lower than 1100°C and silicon contents between 0.3 and 1 wt.% Si, an oxidation passivation period appears between the linear and the parabolic scale growth periods observed for low carbon steels (Figure I. 5).

At oxidation temperatures lower than 1177°C, the duration of the passivation period increases with silicon content. If the oxidation time is very long, the passivation period is masked by the long parabolic phase. The presence of silicon slows down oxidation and reduces oxidation kinetics parameters and final mass gain in comparison with low carbon steels [1, 2, 34, 36, 39, 41-44].

At oxidation temperatures higher than 1177°C, the passivation period disappears and scale growth profiles similar to low carbon steel grade are observed. Scale growth kinetic parameters and final mass gain increase with silicon content and they are higher than those of low carbon steels (Figure I. 6) [1, 2, 43].

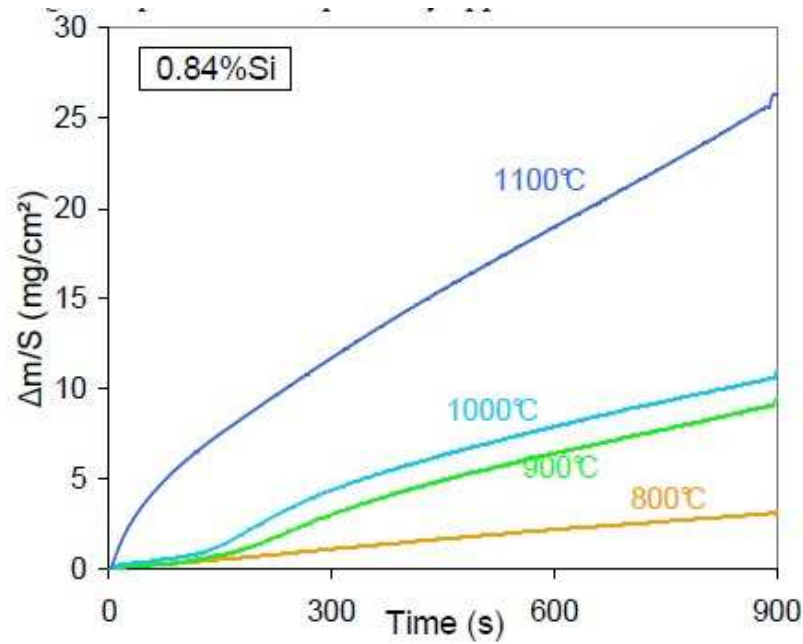


Figure I. 5: Mass gain for samples containing 0.84 wt.% Si; oxidations at 800°C, 900°C, 1000°C and 1100°C during 900 s under 20%O₂, 15%H₂O and N₂: when temperature increases, the passivation period shortens (800, 900 and 1000°C); at high temperatures (1100°C) there is no passivation [1].

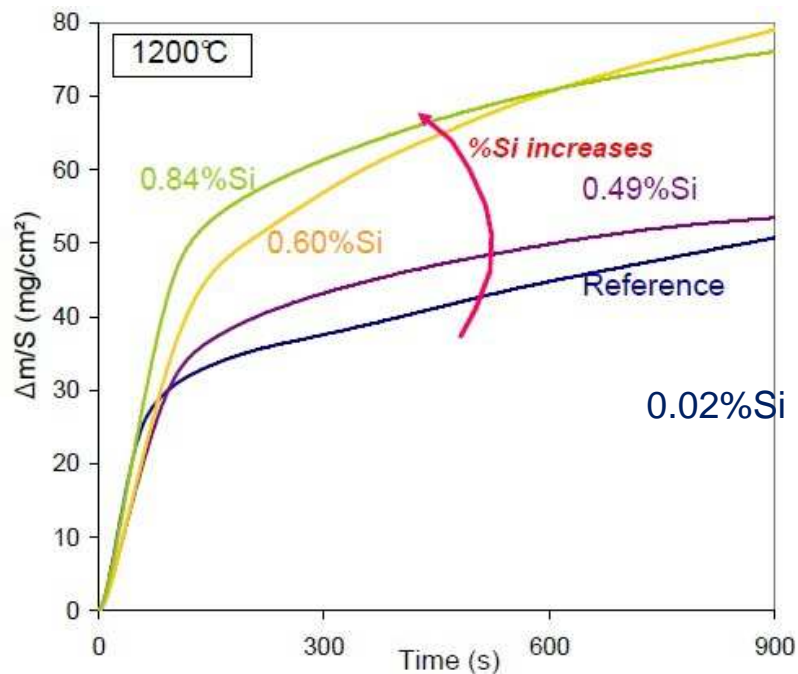


Figure I. 6: Oxidation of samples containing 0.02, 0.49, 0.60 and 0.84 (wt.%) of Si during 15 min under process atmosphere at 1200°C; higher the silicon content, higher is the mass gain [1].

I. 3. 4. 2. Influence of silicon on oxidation mechanism

The passivation period in Silicon alloyed steels oxidation seems to be due to the formation of a silica layer at the beginning of oxidation. It slows down the diffusion of Fe^{2+} towards the oxidizing atmosphere and therefore reduces oxidation rate. Presence of defects and cracks in the silica layer and the formation of solid fayalite-wüstite mixture lead to a post-diffusion parabolic oxidation regime with lower kinetic values in comparison with low carbon steels [45-48].

Silicon contained in steel has more affinity with oxygen than iron. It is first oxidized into silica which forms an interfacial sub-layer between wüstite and steel substrate. The internal oxidation of steel can also be observed (oxide particles inside the steel), especially for the steel containing more than 0.3 wt.%Si [33-36, 49].

Yang *et al.* [41] observed internal oxidation banded layers under metal/scale interface and proposed a mechanism of its formation in four steps:

- Super saturation of oxygen in the steel after external iron oxide formation
- Internal oxidation of silicon leading to silicon depleted zones
- Oxidation of iron in the silicon depleted zones, and
- Repeated processes of saturation-depletion to form the banded oxide scale.

If oxidation time is long enough, the silica thin layer at steel/scale interface and upper wüstite transform into a fayalite phase with the reaction:



While silica grains from internal oxidation remain in the steel substrate under fayalite-wüstite mixture layer [1, 50].

Scale adhesion is lower on silicon steels than that of FeO on pure iron. On the contrary, adhesion between silica or fayalite and the substrate is strong. It is more difficult to remove scale containing silicate phases during pickling due to this higher adhesion [51].

Above 1177°C, the FeO- Fe_2SiO_4 eutectic melt infiltrates scale and steel grain boundaries (Figure I. 7). The penetration depth into the scale increases with the silicon content, while that into the substrate varies slightly. The presence of a liquid phase improves the scale adherence for steels containing < 0.5 wt.%Si, but for higher Si contents (up to 1.5 wt.%) the tendency is inversed. The molten fayalite-wüstite eutectic enhances the iron ions diffusion rate and the oxidation rate is higher than for a pure FeO at the same temperatures [1, 31, 52, 53].

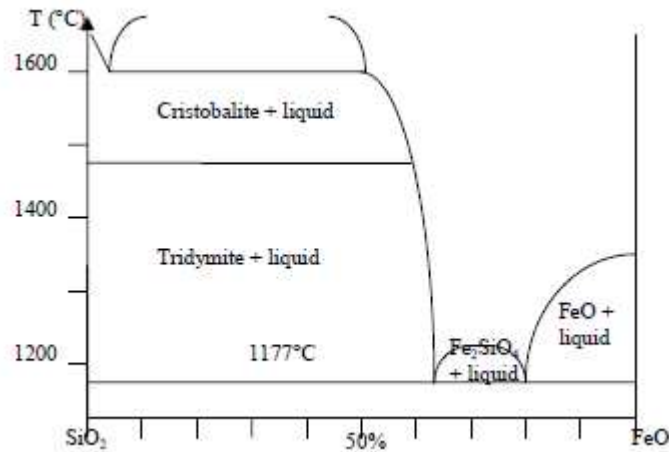


Figure I. 7: FeO-SiO₂ phase diagram [54].

I. 4. Scale and metal oxides properties

I. 4. 1. Hot strip mill (HSM) scales

At the exit of the finishing mill, steel sheets are recovered with scale. They are coiled immediately and stocked. The coils of the hot strip mill are commonly called black coils due to the dark colour of scale. Scale composition depends on coiling temperature, cooling rate and position on the strip.

I. 4. 1. 1. Low carbon steel (LCS) scales

Scales of black coils of LCS are mainly composed of a wüstite layer covered by magnetite and hematite superficial layers.

Depending on the cooling rate, wüstite is transformed partially or completely into magnetite and iron eutectoid (see also I.4.2.2 section and Figure I.9). Water quenching and high temperature coiling favor wüstite conservation. Air cooling and low temperature coiling enhances its transformation.

Scale is generally thin (of 5-20 μm in thickness), spread and brittle due to the mechanical pressure in the hot strip mill. Wüstite is plastic at high temperatures; it is rolled softly in the hot strip mill conditions and at lower temperatures it is brittle which facilitates de-scaling. Magnetite is less plastic than wüstite at high temperatures and less brittle at room temperatures, its cohesion and adherence are higher. Hematite is brittle and extremely hard. It is undesirable during rolling, cooling and also at room temperature [55-62].

I. 4. 1. 2. Silicon alloyed steel (SiAS) scales

Black coils of silicon alloyed steels coming from the hot strip mill have scales with fayalite grains and sometimes with fayalite infiltrations in steel at scale/metal interface. The outer scale is composed of thin and dense wüstite similar to that of low carbon steels. This is due to mechanical pressure of rollers. As fayalite is resistant to pickling, its infiltrations stay on pickled sheets surface and lead to later defects in cold rolling [56, 63].

I. 4. 2. Model scales

I. 4. 2. 1. LCS model scales

Model scales of low carbon steel grades obtained in laboratory furnaces at high temperature, humid oxidizing atmosphere and relatively short oxidation times (below 15 min) reproduce well the chemical composition of hot rolled scales. They are composed mainly of iron oxides; the effect of traces of alloying elements is neglected.

Three oxides are present as continuous parallel sub-layers classified by increasing oxidation degrees on steel: wüstite FeO, magnetite Fe₃O₄ and hematite Fe₂O₃. They are formed by iron ions vacancies diffusion and contact with oxygen. According to [23], the mean thickness ratio of hematite, magnetite and wüstite thicknesses in the total scale is 1:4:95 respectively (Figure I. 8).

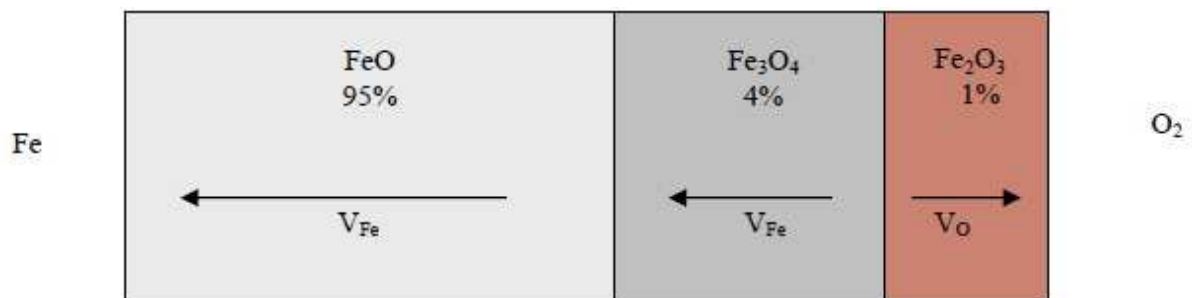


Figure I. 8: Scheme of iron oxides with vacancies diffusion directions and thickness ratios. [23]

Yang *et al.* [41] showed that very long oxidation time at high temperatures produces very thick and cracked scale at the metal/wüstite interface. The diffusion of Fe²⁺ to form wüstite is then blocked by the gap formed by the crack at the steel/wüstite interface and the excess of oxygen favors magnetite layer growth from wüstite and hematite iron supply. The final ratio of hematite, magnetite and wüstite thicknesses in the scale is 1:5:2 respectively [41].

In these conditions, magnetite is the dominant phase in comparison with Païdassi's results shown above [23, 41].

I. 4. 2. 2. Iron oxides properties

Iron oxides can be natural or synthetic. Thermal oxidation of iron or of low carbon steel is not the only way to obtain iron oxide films. It is chosen to better simulate scales of the hot strip mill.

In the literature, other forms of synthetic pure iron oxides such as bulk oxides, sintered powders or sputtered layers on a membrane were elaborated. They were studied in order to obtain information on the behaviour of oxides passive films. It has been shown that the electronic properties of synthetic iron oxides are in good agreement with the behaviour of natural passive films on iron [64-66].

Some properties of the three iron oxides are presented.

Wüstite

Fe_{1-x}O is a non stoichiometric oxide, it shows a p-type semi-conductivity (excess of anions), it is mainly composed of Fe^{2+} cations over-balanced by O^{2-} , $x \text{Fe}^{3+}$ compensate electrical charges loss due to Fe^{2+} vacancies inside the oxide. The concentration of vacancies increases with oxygen percentage and is responsible for cationic diffusion [27, 28, 67-69].

Below 570°C , wüstite is thermodynamically unstable: it transforms into iron and magnetite eutectoid (Figure I. 9).

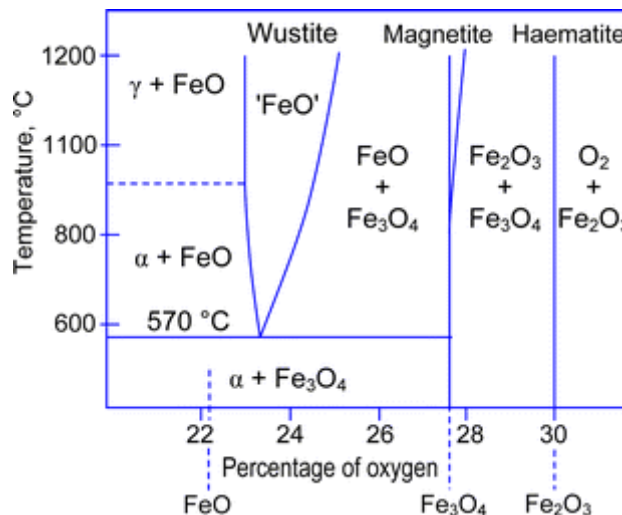


Figure I. 9: Iron-oxygen phase diagram [67].

Chemical reaction and Gibbs free energy of formation of Wüstite is:

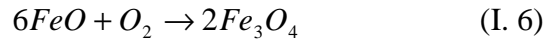


$$\Delta G(J.mol^{-1}) = -519582 + 125T \quad (I. 5) \quad [27, 28]$$

Magnetite

$Fe_{3-x}O_4$ is a non stoichiometric oxide. It shows a p-type semi-conductivity. It has more Fe^{3+} than Fe^{2+} sites in comparison with wüstite, which makes it less prone to oxidation. The number of iron vacancies in magnetite is less important than in wüstite. The diffusion through vacancies can be anionic (O^{2-}) or cationic (Fe^{+2}) [27, 28, 67-69].

Chemical reaction and Gibbs free energy of formation of magnetite is:

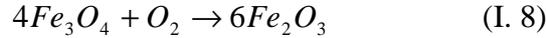


$$\Delta G(J.mol^{-1}) = -624879 + 250T \quad (I. 7) \quad [27, 28]$$

Hematite

Unlike the two other iron oxides, hematite or Fe_2O_3 is a semi-conductive oxide of n-type, with major oxygen vacancies. Diffusion through the vacancies is therefore anionic. Hematite can be formed from magnetite between 200 and 400°C or from iron at ambient temperature [27, 28, 67-69].

Chemical reaction and Gibbs free energy of formation of hematite from magnetite is:



$$\Delta G(J.mol^{-1}) = -499279 + 282T \quad (I. 9) \quad [27, 28]$$

I. 4. 2. 3. SiAS model scales

Scale morphology and chemistry after oxidation of silicon steels in a furnace depends on the combination of different factors such as silicon content, oxidation temperature, atmosphere and time.

In all cases, silicon oxides or iron silicon oxides are present at the steel/scale interface and as grains in the steel substrate under this interface [1, 2, 34, 36, 39, 41, 43, 63, 70, 71].

For short oxidation times, steel surface is covered partially with silica nodules or completely with a silica porous layer (Figure I. 10) [1, 2, 63].

For longer oxidation times and high temperatures but below 1177°C, an intermediate layer composed of fayalite Fe_2SiO_4 grains in a wüstite matrix is present between steel and wüstite layer (Figure I. 11) [1, 2, 39, 70, 71].

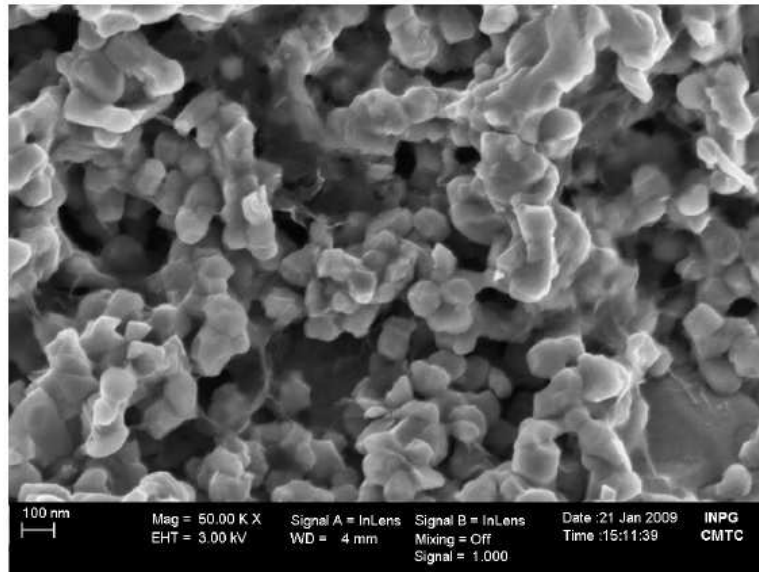


Figure I. 10: SEM observation of the internal layer of a sample containing 0.49 wt.%Si oxidized during 315 s at 900°C: scale layer is porous and is formed by a silica skeleton [1].

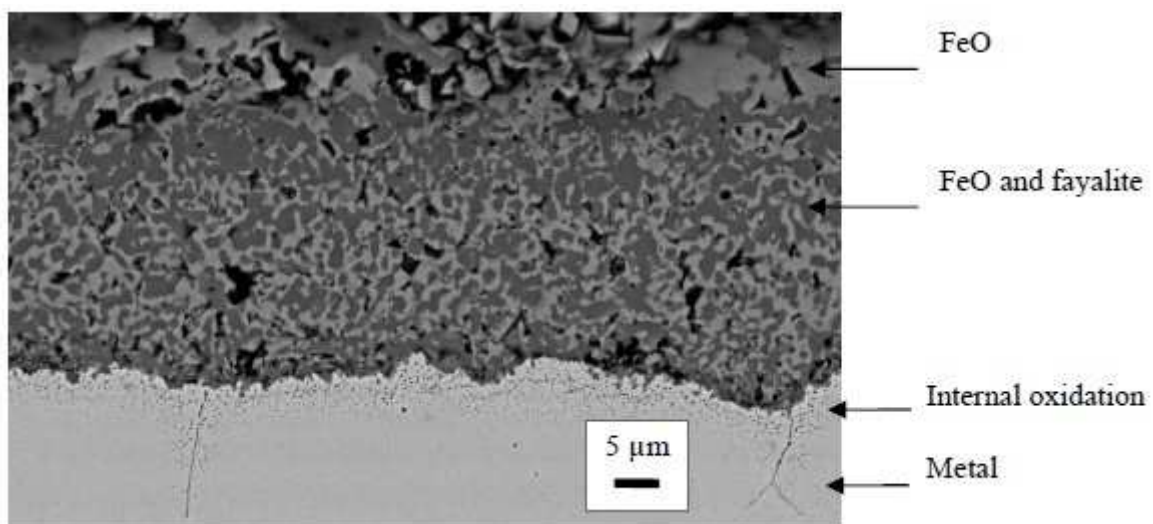


Figure I. 11: Cross-section of a sample with 0.84 wt.%Si oxidized at 1100°C during 15 min. Wüstite appears in light grey, fayalite in dark grey [1].

This intermediate layer is present as a continuous fayalite layer with infiltrations into the steel substrate for oxidation temperatures above 1177°C (Figure I. 12) [43, 71].

Scale nodules with a hematite outer layer surrounded by a supposed silica layer are observed on the surface after oxidation of high silicon alloyed steels at temperatures below 1000°C (Figure I. 13). The nodules are composed of iron oxides layers: hematite, magnetite and wüstite and a fayalite-wüstite mixture layer at steel/wüstite interface [34, 36, 39]

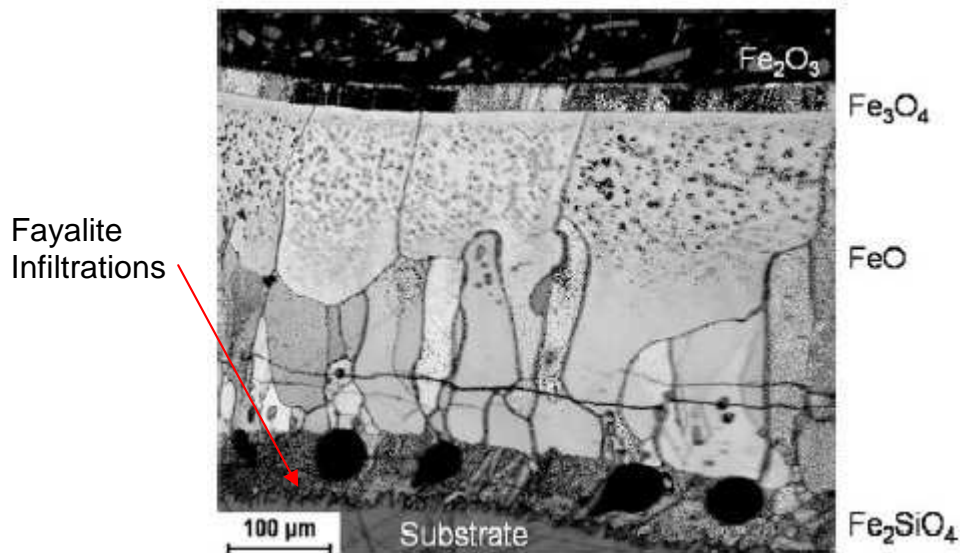


Figure I. 12: Cross section of the oxide grown in an electric furnace on the 2 wt.% silicon steel at 1200°C for 8 min [43].

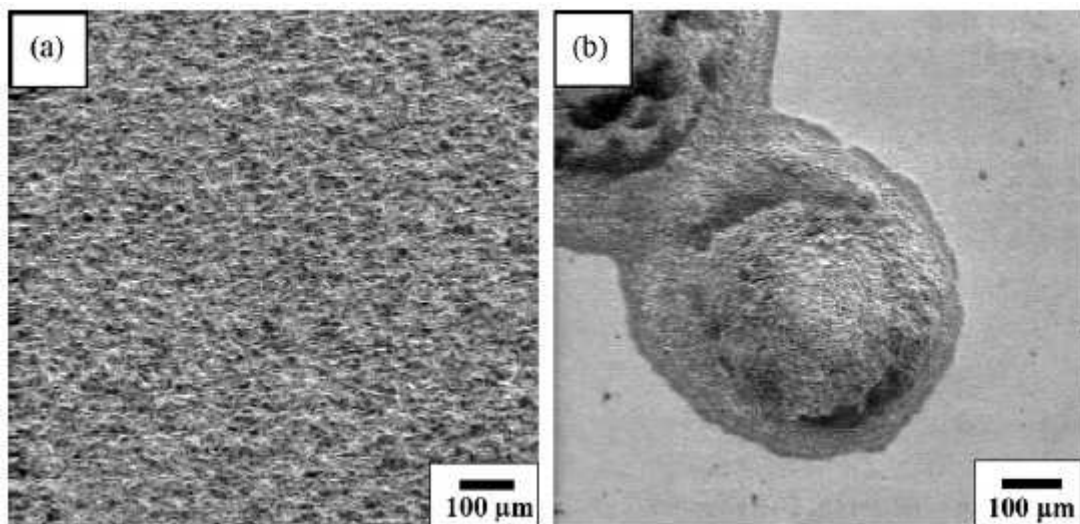


Figure I. 13: SEM micrographs of (a) 0.02 wt.%Si and (b) 1.9 wt.%Si steel oxidized in air at 900°C for 10 h.

I. 5. Pickling and over-pickling

The aim of pickling is the dissolution of the oxide layer or scale in an acid solution. When the acid solution reaches the metal/scale interface, the metal starts to corrode and we talk about over-pickling [72, 73].

In this part, the literature review on pickling and over-pickling of low carbon steels and silicon alloyed steels will be summarized. As the objective of this thesis is the

understanding of the pickling mechanism, a literature review on the dissolution of iron oxides and silicon oxides obtained by processes other than thermal oxidations is also included.

I. 5. 1. Pickling of hot mild steels

Unlike oxidation, where scale growth is controlled by the atmospheric and temperature conditions in the hot strip mill, pickling is a step where the operator can manage the strip speed to obtain complete scale removal and good surface quality.

I. 5. 1. 1. Pickling conditions

The majority of plants uses the same pickling line to remove the scale on classical low carbon steel grades and alloyed steel grades. Sometimes, on alloyed grades surface defects can be generated by mixed oxides, due to insufficient time or inadequate conditions of pickling [74].

Pickling conditions vary from one plant to another; the main pickling conditions are listed below:

- **Pickling line:** it can be continuous, continuous coupled or push-pull.
- **Acidic solution:** Hydrochloric acid (predominant) or Sulfuric acid (mainly for Packaging steels) are used.
- **Corrosion inhibitors:** are generally commercial solutions coming from De Leuze, Kebo, Henkel,... suppliers. Their concentrations depend on the type of inhibitor. The maximum concentration is about 1.5 g.L^{-1} [74].
- **Acid concentration:** it depends on the tank and line and varies between 10 and 230 g.L^{-1} for HCl from the first to the last line tank, where injection of fresh acid is provided.
- **Iron concentration:** it depends on the tank and line and varies between 3 and 400 g.L^{-1} from the last to the first line tank.
- **Line speed:** it varies between 50 and 270 m.min^{-1} , depending on the line geometry (length and tank number), steel grade and bath conditions (acid type, concentration and temperature).
- **Bath temperature:** It is comprised between 70 and 90°C for HCl and up to 100°C for H_2SO_4 .

Kop *et al.* elaborated a laboratory pickling cell to simulate pickling conditions at the laboratory. The scale sample is put in a rotating holder simulating the hydrodynamics. The pickling bath with the industrial acid solution and the inhibitor types and concentrations is heated with a thermostatic circulating fluid [75, 76].

I. 5. 1. 2. Influence of pickling parameters on pickling time

The objective of pickling is to dissolve the entire scale layer in a short time to increase productivity and at the same time, to protect steel from mass loss and high surface roughness due to an excessive over-pickling. Actually, optimal pickling time is defined when all scale is removed with pickling and over-pickling.

Pickling time depends on the metal and scale characteristics and the pickling conditions:

- **Scale thickness:** it increases with the rolling and coiling temperature and is different at the centre and tail of the sheet due to slower cooling. The required pickling time depends on the scale thickness and chemistry [77-79].
- **Scale composition:** for low carbon steel scales, hematite and magnetite dissolution is very slow compared to that of wüstite. For example, in a 88 g.L⁻¹ HCl solution at 80°C, the dissolution rates of Fe₃O₄ and FeO are 0.1 g.m⁻².min⁻¹ and 1.6-2.0 g.m⁻².min⁻¹ respectively. FeO decomposition into Fe₃O₄ and Fe can accelerate its dissolution up to a factor 10 [79-81].
- **Scale morphology:** scale cracking and elongation of 1 to 2 % accelerates pickling with a factor 2 to 3 [82].
- **Bath temperature:** pickling efficiency increases with bath temperature. Pickling is usually performed at 70-90°C [79, 83].
- **Acidic solution:** scale is dissolved quickly in highly concentrated and hot HCl or H₂SO₄ acid solutions. For given concentration and temperature, HCl is more efficient [75, 79, 84].
- **Iron cations concentration (Fe²⁺ and Fe³⁺):** in an HCl medium, the unfavorable effect of Fe²⁺ does not appear below 80 g.L⁻¹, and remains in every case more moderate than in H₂SO₄ medium. The ferric ions Fe³⁺ are known to decrease the pickling time and facilitate the attack reaction of the base metal. But their concentration must be well controlled to avoid over-pickling, mainly for grades which can be pickled rapidly. Generally, the salt concentrations are 50-100 g.L⁻¹ for FeCl₂ and 3-5 g.L⁻¹ for FeCl₃ at the end of pickling [74, 76, 79].
- **Alloying elements concentration:** PO₄³⁻, Mn²⁺, Cr³⁺ coming from steel dissolution increase slightly pickling time.
- **Corrosion inhibitors:** steel is protected from over-pickling by adding small quantities of corrosion inhibitors [85].
- **Hydrodynamics:** Pickling rate is controlled by two phenomena: the dissolution reaction of scales and the diffusion through the boundary layer, which renews the acid consumed on the steel surface. The pickling rate of steels is therefore dependent on the hydrodynamics, which

defines the boundary layer thickness. Indeed, the dissolution reaction rate at the scale surface is determined by the acid concentration, which depends on H^+ diffusion rate through the boundary layer and scale dissolution rate. The hydrodynamics induces a decrease of the boundary layer thickness and an increase of the pickling rate. Ultrasound can also accelerate pickling by detaching scale particles [71, 75, 76, 86].

Pickling parameters and their influence on pickling time are summarized in Table I. 1.

Pickling time ↗	Pickling time ↘
scale thickness ↗	cracks density in scale ↗
$T_{\text{coiling}} \nearrow$	phases mixture / simple oxides ↗
$T_{\text{rolling}} \nearrow$	presence of FeO soluble in HCl / Fe_2O_3 and Fe_3O_4
$T_{\text{bath}} \searrow$	HCl instead of H_2SO_4
[acid] ↘	$[Fe^{3+}] \nearrow$
[impurities] ↗	hydrodynamic ↗
[inhibitor] too high	

Table I. 1: Summary of parameters and their influence on pickling time [74].

Modern pickling lines are controlled by software. Empirical methods are used to correlate the optimal pickling conditions and time. The preset values are then entered in the software and adapted to each steel grade [75, 87].

I. 5. 2. Pickling mechanism of low carbon steels

Scale of low carbon steels is composed of iron oxides. These oxides form parallel layers in the following order from the interface with steel: wüstite, magnetite and hematite. Scale of black coils is a mixture of wüstite, magnetite and iron coming from the wüstite transformation (see also §I.4).

I. 5. 2. 1. Pickling steps of LCS

The evolution of scale morphology and electrochemical state during pickling and over-pickling were observed by coupling an open circuit potential OCP monitoring with a series of cross-section micrographs of scale at significant OCP values [88].

Figure I. 14 shows the evolution of the open circuit potential and scale morphology of a continuous and thick model scale of low carbon steel, dissolved in H_2SO_4 acid. The pickling and over-pickling steps are well separated with an open circuit potential drop once the acid reaches the steel/scale interface [88-90].

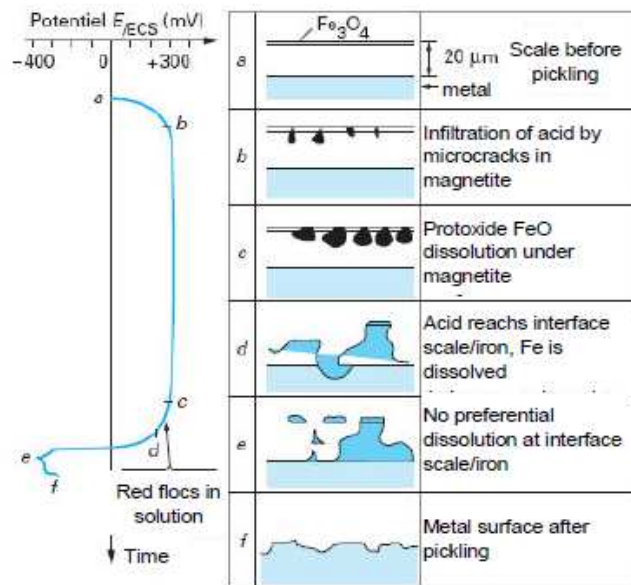


Figure I. 14: Pickling steps and the corresponding electrochemical values during pickling in H_2SO_4 solution of a non cracked scale of low carbon steel [88-90].

According to [88, 89], the evolution of the open circuit potential of a low carbon steel model scale immersed in a H_2SO_4 acid is correlated to the following pickling stages:

- Acid infiltration through the micro-cracks of the superior oxides layer, reaching the wüstite FeO layer (step a-b). Superior oxides are practically not dissolving; these layers keep for a long time a good cohesion. The value of the rest potential increases until the potential of FeO dissolution (approximately + 300 mV/SCE) is reached.

This proposition shows some weaknesses. Indeed, the potential increase from 0 V/SCE to + 300 mV/SCE could be attributed to the acquisition system of the potentiostat starting from 0 V/SCE and not to the dissolved phase nature. A corrosion potential curve of a similar scale will be presented in chapter IV.

- Chemical dissolution of FeO (step b-c). When the sample is thermally treated (quenching and tempering for example), the superficial layer, initially grey-blue (or dark brown), takes an orange color due to a modification of the layer hydration. According to the conditions (temperature, chemical nature of the pickling reagent, characteristics of the scale...), this step will be more or less fast. The potential value remains positive (+ 300 mV/SCE approximately) during this period.

- Acid reaches the metallic interface (step c-d). Hydrogen bubbles come from cracks due to the reaction between acid and iron. A fast decrease of the open circuit potential is observed. Insoluble fragments get loose and stay in suspension in the solution;

- Electrochemical dissolution of oxides (step d-e). The potential takes the value of the cell oxide/acid/iron and is approximately - 420 mV/SCE. The iron is the anode of the electrochemical cell; iron is thus going to dissolve at the same time as FeO.

This proposition is not convincing. Indeed, the negative corrosion potential is the result of the anodic dissolution of the steel substrate by the H^+ of the acid and not the electrochemical cell proposed above (see chapter IV).

At the bottom of cavities dug in FeO, the concentration of acid decreases and that of $FeCl_2$ (for HCl solutions) salt increases. The protoxide continues to dissolve thanks to the agitation which renews the acid in contact with FeO. Corrosion inhibitors allow to avoid a too important attack of the metal and to reduce the quantity of acid consumed.

- Obtaining of well pickled surface (step e-f). The intensity of gaseous release decreases due to the adsorption of inhibitor. The metal is then well pickled. In some cases, residues of scale which are adherent and difficult to eliminate by rinsing remain. We observe a slight increase of the potential value.

The open circuit potential profiles of scale during its dissolution in H_2SO_4 and HCl acids are similar, only potential values are slightly different. In H_2SO_4 bath, specific values are +300 mV/SCE for the positive plateau and - 420 mV/SCE for the negative plateau (Figure I. 14). In HCl bath, the positive and negative plateau values are + 320 mV/SCE and - 360 mV/SCE respectively [89].

There are few differences between the two mechanisms. For the first step, there is a widening of the micro-cracks of external oxides in HCl solutions and not simple infiltration. The surface after pickling presents rounded holes and not angular one as for H_2SO_4 ; this can explain a more beautiful aspect of surface of steel sheets pickled in HCl [89].

According to [82], pickling steps depend also on initial scale composition and morphology (Figure I. 15):

- If scale is composed only of continuous magnetite and hematite layers, the acid may not reach the metal due to the low dissolution rates of these two phases unless they are cracked.

- In triple phase scale, the acid infiltrates the hematite and magnetite continuous layers slowly through micro-cracks and dissolves the underneath wüstite forming growing holes and detaching blocks of the outer magnetite and hematite.

- Wüstite decomposition into magnetite and iron eutectoid enhances dissolution and holes widening. It is due the formation of numerous Fe/ Fe_3O_4 couples which behave as electrodes for an electrochemical coupling in presence of the acid electrolyte.

The high value of the corrosion potential during wüstite dissolution is not compatible with the anodic dissolution of iron (more cathodic). An alternative mechanism implicating the oxidation of magnetite and wüstite seems to be more coherent (chapter IV).

- Big cracks in scale let the acid reach quickly the metal. The Fe/Fe₃O₄/acid electrochemical cell is formed and enhances scale dissolution.

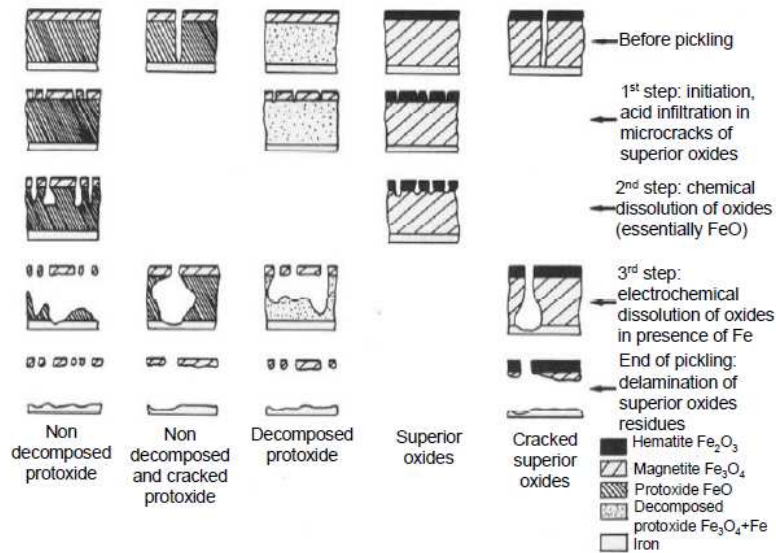


Figure I. 15: Pickling steps for different low carbon steel initial scale compositions and morphologies [82].

I. 5. 2. 2. Pickling reactions of LCS

Pickling reactions and mechanism depend mainly on scale composition and morphology and secondly on the nature of the acid. Many mechanisms were proposed for pickling of low carbon steels.

Hematite and magnetite dissolution:

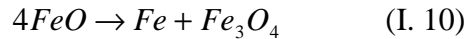
Acid “infiltrates” through micro-cracks of superior oxides to reach wüstite or iron [88, 89, 91]. The two phases are insoluble [91] or almost not dissolved [88, 89] in pickling conditions.

If scale is cracked, a Fe₃O₄/acid/Fe electrochemical cell is formed. The Fe₃O₄ can be reduced by iron coming from wüstite or metal substrate [82]. This mechanism is not convincing and will be criticized in chapter IV.

Wüstite dissolution:

Non decomposed wüstite is dissolved chemically [88, 89] in acid solutions: HCl [75, 76, 79] or H₂SO₄ [75, 76].

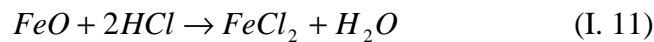
The partial or complete transformation of wüstite at temperatures lower than 570°C produces a mixture of wüstite, iron and magnetite.



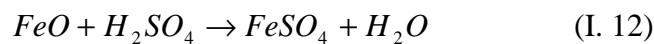
According to Bullough [91], the electrochemical dissolution of wüstite after its transformation takes place in a small electrochemical cell between iron particles, acid and magnetite. Iron and magnetite produced by wüstite transformation plays the role of anode and cathode respectively. The anodic dissolution of iron produces iron cations Fe^{2+} and the cathodic reaction is the reduction of Fe_3O_4 producing more Fe^{2+} . This proposition is not convincing and an alternative mechanism will be presented in chapter IV.

Non stoichiometric wüstite $Fe_{1-x}O$ has an excess of Fe^{3+} . The x Fe^{3+} sites can be reduced by iron coming from steel substrate or wüstite decomposition [92].

The main **chemical reaction** of scale during pickling corresponds to the dissolution of wüstite in the acid, the dissolved iron cations were presented in a form of salts with chlorides and sulfides. In HCl, FeO dissolves with the chemical reaction [79]:



And in H_2SO_4 with the chemical reaction [75, 76]:



In pickling baths, the salt form seems theoretical since the concentration of the anions does not reach the solubility limit of the salts.

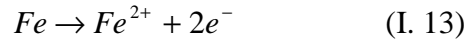
Steel dissolution:

Once the acid reaches the metal/scale interface, electrochemical dissolution of the remaining oxides starts with the formation of Fe/acid/oxides electrochemical cell where iron is the anode and the oxides are the cathode [88, 89]. This proposition is not convincing and an alternative mechanism will be presented in chapter IV.

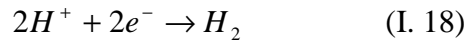
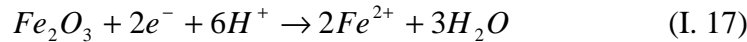
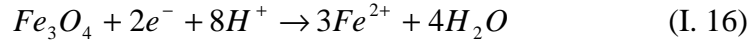
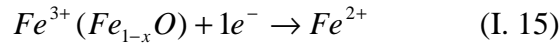
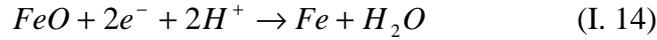
In addition to the electrochemical cell mechanism, the acid attacks any metallic surface producing hydrogen. The majority of this hydrogen is in molecular form. H_2 bubbles assist mechanical removal of scale and another part diffuses through steel and can cause some embrittlement [91].

The **electrochemical reactions** take place in iron/acid/iron oxides electrochemical cells. The **anodic** reaction is the dissolution of **iron** and the **cathodic** reaction is the **reduction of iron oxides** in the acid solution. Iron comes from wüstite dismutation during pickling and steel substrate during over-pickling. Protons reduction also takes place as cathodic reaction on metallic surface during pickling and over-pickling.

- Anodic reaction [92, 93] :

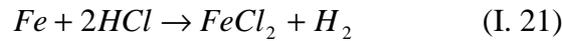


- Cathodic reactions [92, 93]:



Some of these reactions cannot take place at the same corrosion potential. They will be placed in the right corrosion potential ranges in chapter IV.

As for the chemical reactions, the dissolved iron cations coming from the electrochemical reactions can form salts with chlorides and sulfides. The yield reactions in HCl [79] can be written as:



In pickling baths, these salts are not observed since their concentration does not reach their solubility limit.

I. 5. 2. 3. Iron oxides dissolution

As seen in the section I. 5. 2. 2 above, the majority of studies on pickling of low carbon steel were empirical and basic mechanisms were proposed. In these mechanisms, the dissolution of the iron oxides in scale can be chemical and/or electrochemical and often implicates a mixture of iron and iron oxides phases.

To gain a better insight in the overall mechanism, in the literature, a large amount of work has been carried out on natural and synthetic pure iron oxides to characterize their dissolution mechanism [94-102].

The main difficulty is to find experimental methods which allow distinguishing the chemical and electrochemical dissolutions mechanism [98, 100-102]. For instance, in situ X-ray absorption near-edge spectroscopy (XANES) was used simultaneously with electrochemical methods on synthetic oxide to determine the nature of the dissolution reaction, leading to the conclusion that dissolution of hematite and magnetite is mainly

chemical in the anodic potential range, and that electrochemical dissolution of magnetite has to be taken into account in the cathodic range [100, 101].

I. 5. 3. Effect of Silicon on pickling mechanism

After oxidation in the hot strip mill, silicon oxides (silica and fayalite) concentrate at the steel/scale interface in many forms; silica thin layer, fayalite grains in wüstite, fayalite infiltrations and silica internal oxidation grains in steel substrate.

The upper iron oxides layer dissolves easily but the low solubility of silicon oxides present at steel/scale interface increases the pickling time. In the fayalite infiltrations and high internal oxidation cases, a long over-pickling step is necessary to suppress fayalite and oxides at the grain boundaries [80, 89, 103].

According to [104] a relatively long pickling time is necessary to suppress completely the scale of a 3 wt.% Si steel, whatever the nature of acidic solution. In HCl bath, the addition of nitric acid induces a more reactive bath towards the metallic surface. The addition of HF acid increases the pickling efficiency without increasing the metal dissolution, due to its efficiency to dissolve silicon oxides.

Chattopadhyay et al. [105] studied the effect of silicon contents from 0.06 to 2 wt % in automotive steels on pickling time in 5, 8, 11 and 14% HCl solution at 82°C simulating the industrial process. The different steel grades have the same scale thickness but do not clean at the same pickling rate. This is due to differences in scale composition. Fayalite $\text{Fe}_{2.44}\text{Si}_{0.55}\text{O}_4$ appears for silicon content higher than 0.35 wt. % and has a negative effect on pickling. Pickling time increases with silicon content (Figure I. 16).

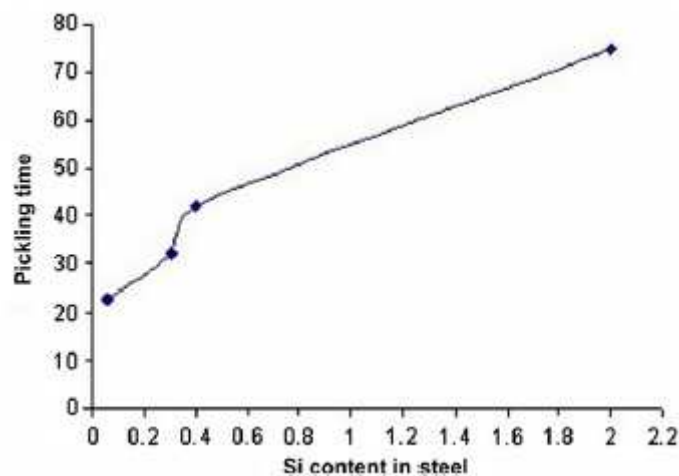


Figure I. 16: Relationship between the Silicon content (wt.%) in steel and the pickling time (seconds).

The role of silicon and aluminum contents on pickling time of a low alloyed hot rolled steel sheet has been investigated by Y.N. Chang [106]. The increase of silicon content from 0.5 to 2 wt.% induces an increase of the amount of FeO required combining with SiO₂ to form Fe₂SiO₄ at high temperature. The Fe₃O₄ transformation was reduced at room temperature. The pickling rate was thus slightly promoted as mentioned by Chattopadhyay et al. [105]. However, an addition of 0.4 wt. %Al was detrimental to pickling due to the formation of segregated FeAl₂O₄ at the scale/base metal interface.

I. 5. Conclusions

Oxidation of low carbon steels was widely studied and its mechanism is well described. Scale growth follows first a linear then parabolic law. The linear step corresponds to the oxidation of steel surface and the parabolic to iron ions oxidation after diffusion in scale. Scale is composed of iron oxides with increasing oxidation degree for iron: wüstite (FeO), magnetite (Fe₃O₄) and hematite (Fe₂O₃). Wüstite is unstable below 570°C, it transforms partially into iron and magnetite eutectoid. The scale of black coils is composed of thin and brittle wüstite due to mechanical pressure in the hot strip mill.

The presence of silicon slows down the oxidation rate and a passivation period appears between the linear and parabolic steps. This passivation period disappears for oxidation temperatures higher than 1177°C and the oxidation rate is higher than the one of low carbon steels. Silicon is first oxidized into silica SiO₂, it forms a barrier layer for iron diffusion towards oxygen and reduces oxidation rate. Silica can also appear in the steel substrate, due to internal oxidation at grains boundaries. Silica and wüstite are transformed into fayalite Fe₂SiO₄ and form a fayalite-wüstite internal layer. Above 1177°C, molten fayalite enhances iron diffusion and oxidation rate, and after cooling forms an internal layer with infiltrations in steel.

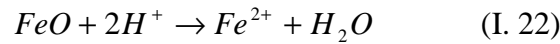
The oxidation and scale characterization of low carbon steels are well known while there are some points to study or confirm in the oxidation of high silicon alloyed steels especially in humid atmospheres and at high temperatures.

The first part of this work will be the exploration of the oxidation conditions to form model scales of low carbon steel and high silicon alloyed steel and the well characterization of iron-silicon oxides.

Pickling and over-pickling steps of low carbon steel were extrapolated from the evolution of electrochemical potential of a non cracked scale. Hematite and magnetite resist to

pickling, they are slowly infiltrated by the acid. Wüstite is easily dissolved by formation of holes and widening of cracks. Once acid reaches metal, the electro-chemical potential drops and over-pickling starts.

As wüstite is the main component of low carbon steels scale, its chemical dissolution reaction is considered to be the reference reaction for pickling:



According to Bullough [91] and Quantin [89], iron coming from wüstite dismutation or scale/wüstite interface is assumed to be dissolved in a micro-electrochemical cell where iron and magnetite plays the role of anode and cathode respectively.

For silicon steels, silica and fayalite at steel/scale interface resist to pickling and increases pickling time. If fayalite infiltrations and silica grains are important, a long over-pickling step is necessary to remove them.

The literature review shows some critical points in the proposed pickling mechanisms for low carbon steel scales. Only empirical studies were conducted on silicon alloyed steels to estimate the effect of Si-containing phases on pickling time.

In the second part of this work, model scales of low carbon steels and high silicon steels will be pickled in soft conditions. The modelling of scale/acidic solution interface and the chemical and electrochemical contributions during scale dissolution will be presented.

II. Experimental and methods

Summary

II. 1. Elaboration of steel grades samples	47
II. 1. 1 Steel chemical composition	47
II. 2. 2. Steel grains size	48
II. 2. Oxidation of steels	48
II. 2. 1. Oxidation experiments.....	48
II. 2. 2. Oxidation methods.....	50
II. 3. Scale Characterization after oxidation	51
II. 3. 1. Optical observations	51
II. 3. 2. Spectrometric methods	51
II. 4. Scale dissolution characterization	51
II. 4. 1. Electrochemical measurements	52
II. 4. 1. 1. Electrochemical set-up	52
II. 4. 1. 2. Electrochemical methods.....	55
II. 4. 2. ICP-AES setup and method.....	62
II. 5. Scale characterization after pickling and over-pickling	65

II. 1. Elaboration of steel grades samples

A new quick and simple way to fabricate samples of steel with different grades was elaborated in ArcelorMittal Maizières Research, it uses a 1 kg (Annex I) furnace where a de-rusted bloc of low carbon steel called Si00 is heated with induction until melting state then adequate masses of silicon are added to create the desired grades. After each addition, molten steel pencils are extracted with a glass tube and let at room temperature for cooling. Once the solidification completed and the pencils are at room temperature, the glass tubes are broken. The pencils have a cylindrical form with a 4 mm diameter and 120 to 150 mm length; they are cut with a SiC disc motor saw to reach nearly 5 mm length. In the case of elaboration of one steel grade, no pencils are extracted after silicon addition; the final steel bloc is recovered after cooling and cut with a SiC disc motor saw into parallelepipeds of 5x10x20 mm maximum dimensions.

Samples of steel grades from industrial lines (example of Si00) are recovered as large sheets cut from black coils at the exit of the hot strip mill. The large sheets are cut into smaller sheets of an A4 paper size. Discs of 25 mm diameter are extracted from the small sheets with a mould put under high pressure in an automatic vice. Small blocs of parallelepiped form of 5x10x20 mm maximum dimensions are cut with a SiC disc motor saw. The samples surfaces are then polished with a SiC-paper up to grade 800, cleaned in ethanol and then dried in air before oxidation tests in order to remove rust and scale before oxidation. The same surface polishing and cleaning is provided for scale free samples before pickling experiments.

II. 1. 1 Steel chemical composition

In this study, samples of three grades with high silicon content for oxidation then pickling experiments are chosen: Si00, Si16 and Si32. To determine the real composition of the three grades, especially the silicon mass fraction, chemical analysis with an Optical Emission Spectrometer is done on a sample of each grade (Table II. 1). This spectrometer makes a correlation between the intensity of an emitted light at a given frequency specific to an element and the mass fraction of that element.

The tolerated error for the OES is about 0.2%, the values obtained are close to the composition of the target and respect the error interval. The Si00 is a low carbon steel with few alloying elements, their influence on oxidation and pickling is weak. The other grades chosen for oxidation and pickling Si16 and Si32 have both high enough silicon concentration to have a significant effect on oxidation and pickling.

Sample	Elements (wt%)								
	C	Si	Mn	P	Cr	Ni	Cu	N	Fe
Si00	0.04	0.02	0.19	0.01	0.025	0.017	0.025	0.01	Balance
Si16	0.04	1.55	0.19	0.01	0.025	0.017	0.025	0.01	Balance
Si32	0.04	3.25	0.19	0.01	0.025	0.017	0.025	0.01	Balance

Table II. 1: Chemical composition of the three steel grades with optical emission spectroscopy (OES).

II. 2. 2. Steel grains size

The observations of Si00 and Si16 surfaces after Nital attack are shown in Figure II. 1. The majority of grains have an average size of 150 μm that is almost identical for the three grades. The grains sizes and their distribution will not have any influence on oxidation rate between the samples.

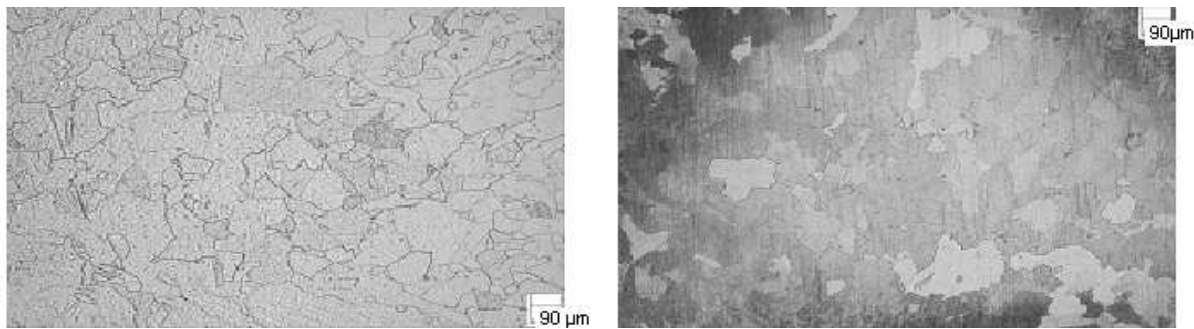


Figure II. 1: Grains size by optical microscope. Left: Si00. Right: Si16.

II. 2. Oxidation of steels

Scale free steels were oxidized in adapted furnaces simulating the hot strip mill conditions and their oxidation kinetics followed with a thermo-gravimetric method.

II. 2. 1. Oxidation experiments

The oxidation experiments with continuous mass change measurement are conducted in a Linseis[®] Thermo-Gravimetric Analyser (TGA). The TGA setup used for this study is shown in Figure II. 2 and Annex II.

It uses an electrical resistor for heating, an outer water circuit for cooling and electromagnetic mass change analyser. The oxidation tests are programmed and the mass change and temperature data are recorded with a Linseis[®] domestic software.

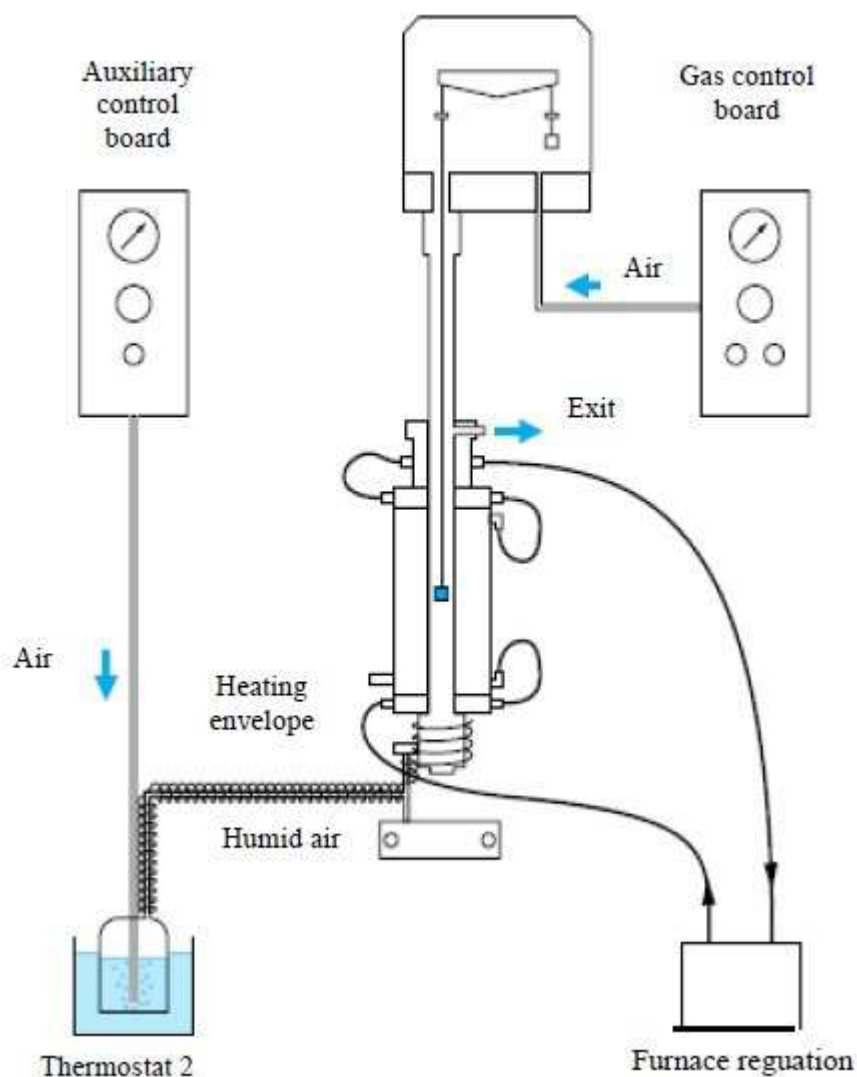


Figure II. 2: General set-up of the Linseis Thermo-gravimetric Analyser used for oxidation tests.

Before oxidation tests, the sample is ground with a SiC-paper up to grade 800, cleaned in ethanol, dried in air and suspended in the TGA sample holder with a welded hook. The TGA chamber is depressurized then filled with nitrogen continuous flow.

The mass change is recorded continuously. The sample is heated in a nitrogen atmosphere at a rate of 40°C/min and 5°C/min for the last 50°C to avoid over-heating once the desired oxidation temperature is reached. All oxidations of this study are isothermal in the temperature range 850-1200°C, in a 15% humid air during 15 minutes (samples heating until the desired temperature is provided under inert gas (N₂) atmosphere). Some additional experiments have been performed at lower durations for characterization purposes or specific scales. After the test, the TGA chamber is cooled in a N₂ atmosphere down to room temperature with a 40°C/min rate (Figure II. 3).

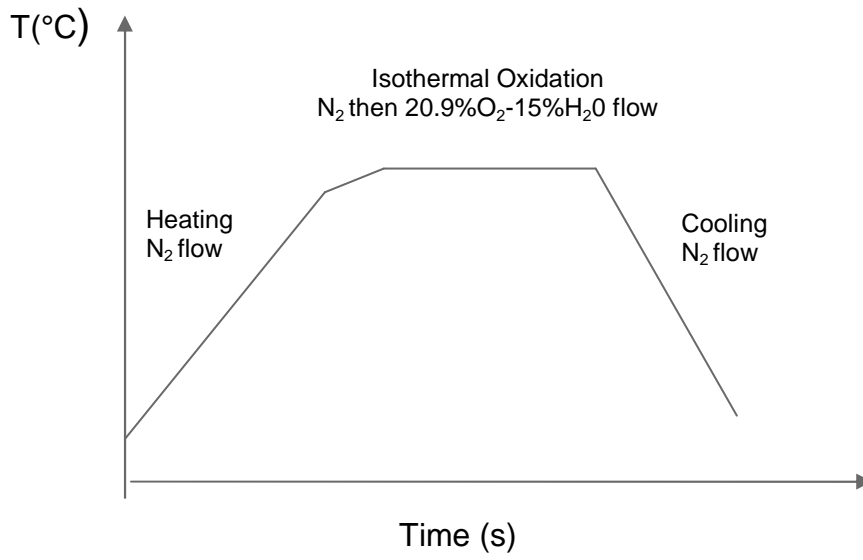


Figure II. 3: Typical oxidation temperature profile and atmosphere compositions.

In the TGA, only one sample can be oxidized and the sample holder size is limited to maximum 20x10x5 mm, larger samples can damage the thermocouple at the base of the TGA sample holder during oxidation. For oxidations of a set of samples with bigger sizes, an Orion[®] pilot furnace with a large and flat sample holder (40x80 mm) is used. The samples are deposited on the flat sample holder with the face to be oxidized on the top; one sample is sacrificed to measure the current temperature with a welded thermocouple. The samples preparation and oxidation conditions program with the Orion[®] Pilot domestic software are the same as for TGA, except mass change measurement, an option not available in the pilot furnace.

II. 2. 2. Oxidation methods

Oxidation of metal is a high temperature corrosion reaction between a metal surface and an oxygen based atmosphere - O₂ or H₂O or both are often used as the oxidizing species due to their presence in the hot strip mill atmosphere - where a certain amount of oxygen atoms are fixed on the metal surface increasing the mass of the new metal-oxide bloc. The correlation between mass change and oxidation kinetics is therefore evident and made the thermo-gravimetric analysis the best method for this study.

The mass change obtained with TGA is divided by the sample surface to give a normalized mass change per surface unit versus time curve:

$$\Delta m / S = f(t) \quad (\text{II. 1})$$

$\Delta m/S$: Mass change per surface unit

t: oxidation time

The curve profiles are analyzed to see if they fit some common mathematical functions (linear, parabolic; exponential...), the corresponding kinetic law and constants can therefore be estimated. In the case of random profile, the oxidation is considered chaotic.

II. 3. Scale Characterization after oxidation

II. 3. 1. Optical observations

After oxidation in the thermo-gravimetric analyser or pilot furnace, the samples are moulded in a cold resin and ground with SiC papers up to grade 4000 to obtain cross-sections micrographs. For scale external surface observations, no treatment is needed after oxidation.

Cross-section and surface micrographs of scale phases are obtained with an Optical Microscope (OM) integrated in a Raman spectroscopy device and a Scanning Electron Microscopy (SEM) device.

II. 3. 2. Spectrometric methods

The nature of phase is identified using Raman spectroscopy analyses and estimation of elements content given by Energy Dispersive Spectroscopy (EDS). Some samples are analysed by X-rays Photoelectron Spectroscopy (XPS) and Auger-FEG. The XPS setup used for characterizations is a Perkin-Elmer PHI 5500 with monochromatic Al $K\alpha$ X-ray source of 187 eV (for survey spectra) and 11 eV (for high resolution spectra) pass energies of the analyzer. XPS characterizations show a depth resolution of 10 nm. Analyzed area is of $0.8 \times 2 \text{ mm}^2$. Auger-FEG characterizations are performed with a Jeol Jamp 9500F device. Analyses are done at an acceleration voltage of 15 kV, a beam current of $1 \times 10^{-8} \text{ A}$ and a sample tilt of 0° .

II. 4. Scale dissolution characterization

Pickling and over-pickling tests are conducted on three types of samples:

- Black coils coming from the hot strip mill.

- Model samples with scales grown in the thermo-gravimetric analyzer (TGA) or the pilot furnace.

- Scale free steel cylinders or blocs.

Samples preparation for pickling tests depends firstly on their initial form and size (sheets, cylinders, discs, parallelepipeds) and nature (scale free steel or scaled steel) and secondly on the pickling cell and measurement method.

Two pickling experimental setups are used:

- Electrochemical set-up for corrosion potential, corrosion current and electrochemical impedance spectroscopy measurements.

- Inductively Coupled Plasma – Atomic Emission spectroscopy (ICP-AES) coupled with a potentiostat for total dissolution rates coupled with corrosion potential and corrosion current measurements.

II. 4. 1. Electrochemical measurements

Electrochemical measurements during pickling and over-pickling were done in an experimental setup adapted to steel samples covered with scale. It consists of an electrochemical cell connected to a potentiostat and frequency response analyzer.

Different electrochemical methods were programmed to extrapolate the different aspects and contribution of electrochemical processes in pickling and over-pickling mechanism.

II. 4. 1. 1. Electrochemical set-up

The electrochemical cell used for pickling and over-pickling experiments is composed of three electrodes immersed in an acid bath and connected to a potentiostat:

- **Reference electrode:** has a constant potential in the same range of temperature. All potential values are given versus this potential. As pickling and over-pickling experiments in this study are conducted in hydrochloric acid (HCl) solutions, the saturated calomel electrode (SCE) with KCl solution was used to avoid contamination of the acid solution by foreign ions (K^+ is inert and Cl^- is already present in the acid solution). A saturated KCl extension tube is used to protect the reference electrode during high temperature dissolutions.

- **Auxiliary electrode:** is a platinum grid with a surface high enough to avoid current saturation. The potential is applied between the reference electrode and the working electrode. The current is measured in the circuit made of the WE and the auxiliary electrode.

- **Working electrode:** A rotating electrode with a three cylindrical pieces sample holder was elaborated (Figure II. 4). The outer piece is open partially at the bottom to expose the sample surface to the solution. Acid infiltration into the sample holder is prevented with a rubber circular joint between the outer piece bottom and the sample. The intermediate piece is screwed on the bottom piece pressing the sample on the rubber joint. The central piece made of stainless steel is screwed on the intermediate piece ensuring electrical contact between the back of the sample and the head of the rotating electrode.

To fit in the holder, the sample must have a disc form with 25 mm diameter and a maximum thickness of 5 mm.

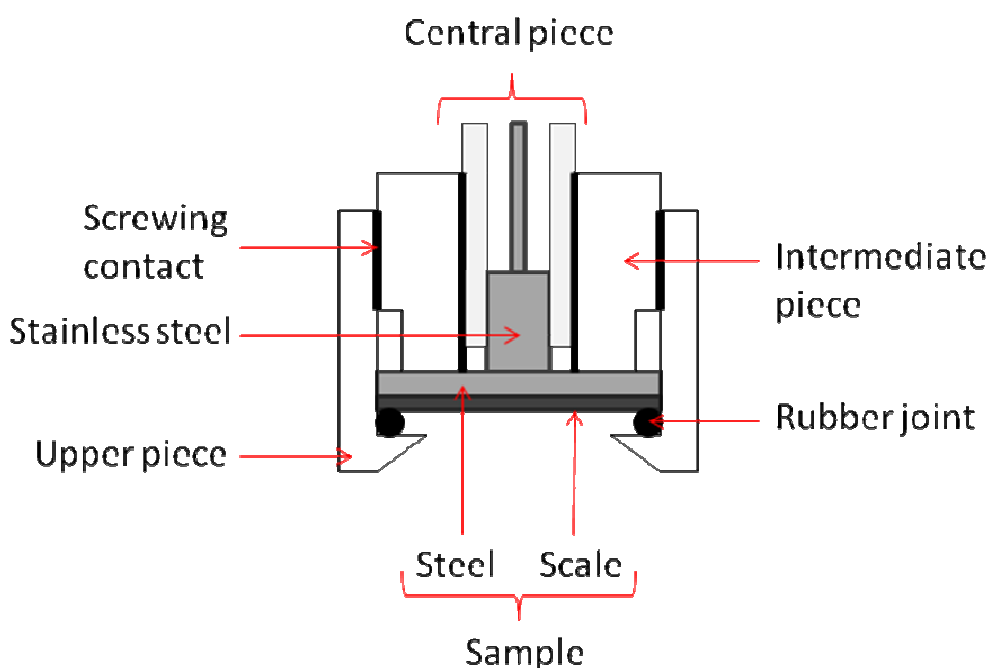


Figure II. 4: Scheme of a cross-section of the sample in the rotating electrode sample holder.

The elaboration of the working electrode with a disc form and specific size requirements depends on the origin of the sample:

- Directly from the black coils sheets: discs are extracted from the sheets with a cylindrical mould with 25 mm diameter put under pressure in an automatic vice, polished on the back face to ensure electrical conductivity and put in the rotating electrode sample holder with the scaled face at the bottom in contact with the rubber joint. The intermediate and central pieces are screwed gently to avoid scale cracking on the rubber joint. For scale free measurements both disc faces are polished before being put in the sample holder.
- For samples oxidized in the Thermo-gravimetric analyzer (TGA): due to limited sample holder size in the TGA, only cylinders with 4 mm diameter and 5 mm length are oxidized in

this device. The difference of size is compensated with a cold resin poured around the small sample in a 25 mm diameter mould (Figure II. 5). The scale surface of one disc face of the sample is protected from the resin with a soft paste spread on the bottom of the mould; the sample bottom surface penetrates a little bit in the soft paste to avoid any infiltration of the resin under the sample. After solidification of the cold resin, the enlarged sample is removed from the mould; the soft paste is removed from the sample face to be pickled. Before putting the enlarged sample in the rotating electrode sample holder, the other face is polished until removing all resin and scale to ensure electrical conductivity.

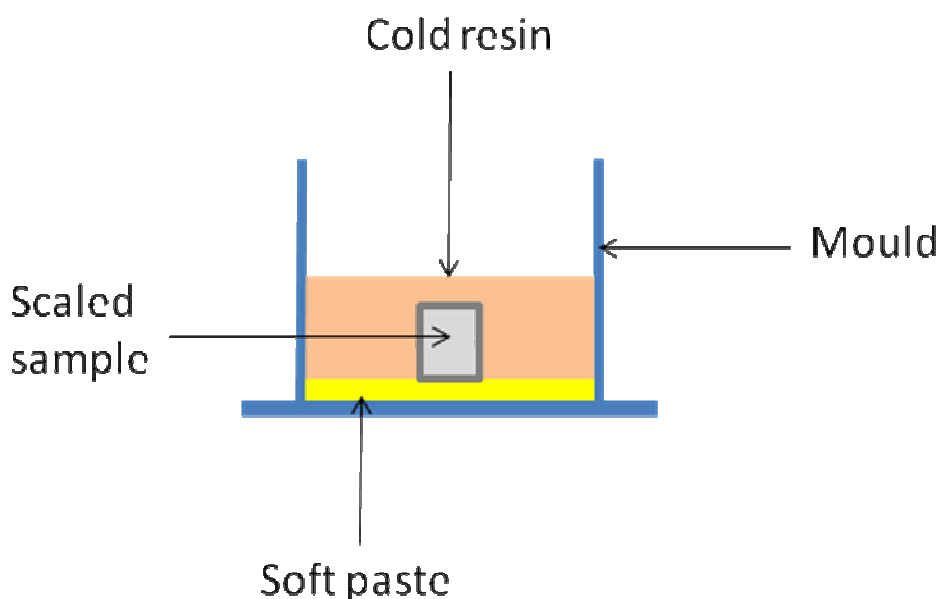


Figure II. 5: Cross section scheme of a resin sample enlargement mould.

- Oxidation in the pilot furnace: the oxidized samples in this case are discs with 25 mm diameter. After oxidation, the disc surface in contact with the flat sample holder of the furnace is polished to ensure the electrical conductivity. The sample is placed in the rotating electrode sample holder with scale at the bottom in contact with the rubber joint. The intermediate and central pieces must be screwed gently to avoid scale cracking on the joint rubber.

The acid solutions with the desired concentration are prepared by dilution of a concentrated hydrochloric acid solution 37% in mass and kept in phials in a hood.

The acid solution is poured in a double layer container where a thermostat fluid circulates to fix the temperature of the bath. The reference and auxiliary electrodes and a thermometer are immersed in the bath while it is heating (Figure II. 6). Once the bath reaches the desired temperature and the sequence of the electrochemical methods is programmed in the potentiostat pilot software, the working electrode is immersed and the measurement sequence is launched immediately.

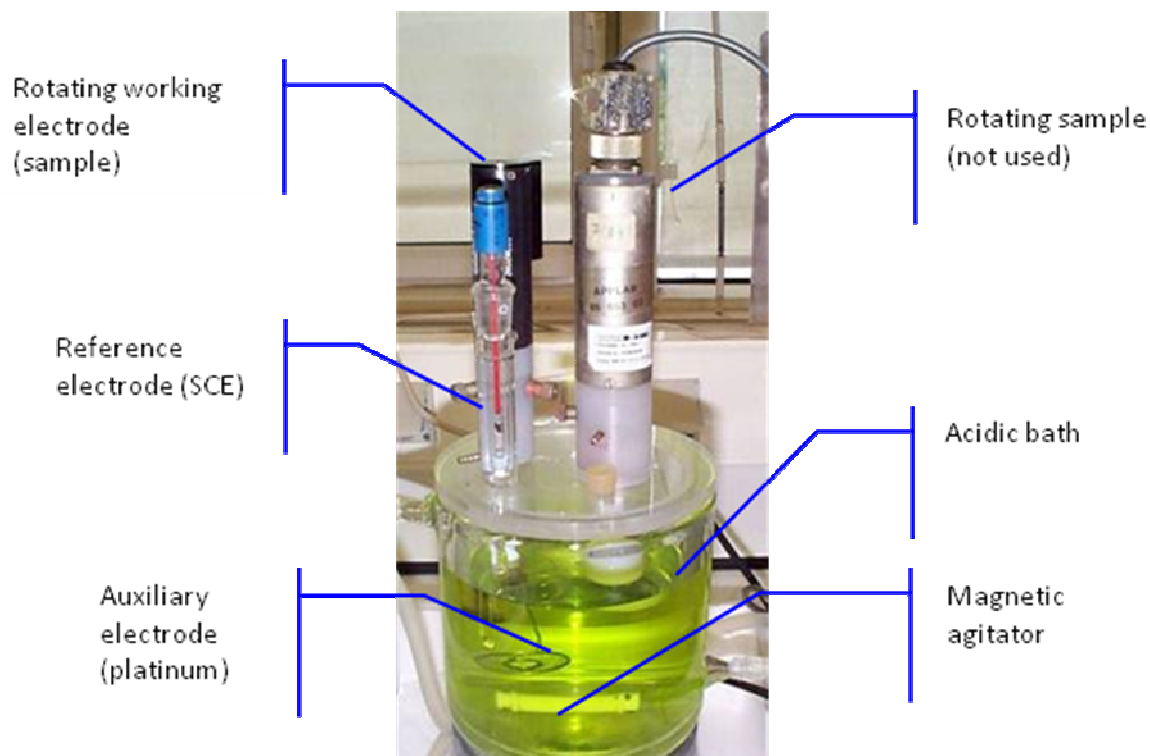


Figure II. 6: Electrochemical cell with pickling bath.

Two potentiostats were used for electrochemical studies: a Schlumberger® Solartron® SI 1286 potentiostat coupled with a Schlumberger® Solartron® Frequency Response Analyser, with Corrwave® and Zplot® as pilot softwares and a VoltaLab® 80 with VoltaMaster® as pilot software.

II. 4. 1. 2. Electrochemical methods

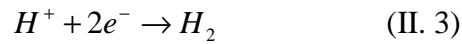
In a pickling or over-pickling process, a solid phase – scale and steel – is dissolved in an acid solution. To evaluate the electrochemical contribution and characteristics in this dissolution, different methods were used.

Corrosion is the result of the electrochemical transformation of a metallic substrate or oxide into cations dissolved in aqueous solution. In the case of the metallic substrate, the corrosion occurs according to the **anodic reaction**:



This reaction is thermodynamically possible if the system is in the corrosion domain of the pH-E or Pourbaix diagram. The boundary between the immunity and corrosion domains is given by the Nernst Potential of the reaction.

A **cathodic reaction** is always parallel to the anodic reaction. The corrosive species are reduced by the electrons lost by the metal. In the case of metallic substrate corrosion in an acidic solution, the reduction of protons is the main cathodic reaction:



Four methods were used to study the electrochemistry of pickling and over-pickling for each sample of this study:

Open Circuit Potential (OCP)

The open circuit potential in this study corresponds to the corrosion potential. It is measured and recorded continuously during pickling and over-pickling experiments:

$$E_{corr} = f(t) \quad (\text{II. 4})$$

E_{corr} : Corrosion potential (V/SCE)

t: Dissolution time (t)

The corrosion potential value indicates the electrical state of the sample in the solution. It is a mixed potential fixed by the equality between the anodic and cathodic currents. At corrosion potential the resulting current is null:

$$I_{OCP} = I_a + I_c = 0 \quad (\text{II. 5})$$

By convention: $I_a \geq 0$ and $I_c \leq 0$

This method does not disturb the system. The corrosion potential values evolution depends on the nature of the phases reached by the acid solution during scale dissolution and gives an estimation of the time needed for the acid to cross each phase.

Current density:

Electrochemical corrosion kinetics are evaluated with the anodic corrosion current I_{anod} , it measures the electrical charge transfer velocity between the dissolved anode and the oxidant species at the electrode surface in contact with the solution. If the anodic reaction is identified, the anodic current can be expressed with mass loss or moles of the corroded solid phase according to Faraday's law:

$$I = \frac{dq}{dt} = \frac{z \cdot F}{M} \cdot \frac{dm}{dt} = z \cdot F \cdot \frac{dn}{dt} \quad (\text{II. 6})$$

I: corrosion current (A: Ampère)

q: electrical charge (C: Coulomb)

t: time (s: seconds)

M: molar mass ($\text{g} \cdot \text{mol}^{-1}$)

m: mass (g: gram)

n: number of moles (mol)

F: Faraday's constant (96500 C.mol⁻¹)

z: number of electrons exchanged

In general, corrosion current rate is expressed as current density. The current values are normalized with the electrode surface to be comparable with literature and reference values. Therefore, the mass and mole loss rates are also normalized with the electrode surface. The common surface unit is cm².

The corrosion current at a constant applied potential E_i is monitored with the chrono-amperometry method:

$$I_{corr} = f(E_i, t) \quad (\text{II. 7})$$

At open circuit potential, the resulting current is null (equation II. 5), no direct measurement is possible. The anodic (or cathodic) current must be extrapolated with indirect methods.

The Tafel curves extrapolation method [107] was used to evaluate the corrosion current at discrete times of pickling and over-pickling. The Tafel behaviour is only observed if the half reaction is controlled by the charge transfer rate, this is usually the case for the H⁺ reduction in acidic solutions (pH < 3). It consists of a potential scan deviation from the corrosion potential toward negative values for the cathodic curve and positive values for the anodic curve with a chosen potential scan rate and interval. Both curves are represented in the same semi-logarithmic graph:

$$\text{Log}(I) = f(E) \quad (\text{II. 8})$$

A Tafel corrosion process is controlled by the activation energy, the anodic or cathodic reaction can be expressed by the equation:

$$I = I_0 \cdot e^{bE} \quad (\text{II. 9})$$

The Tafel constant b is defined by the equation:

$$b = \frac{\alpha_t \cdot z \cdot F}{RT} \quad (\text{II. 10})$$

Where α_t is the transfer coefficient with $0 \leq \alpha_t \leq 1$, R the universal gas constant (8.31 J.mol⁻¹.K⁻¹) and T the absolute temperature (K).

As the total current is the sum of the anodic and cathodic currents it is expressed with the following equation:

$$I = I_a + I_c = I_{a0}e^{b_a E} + I_{c0}e^{b_c E} \quad (\text{II. 11})$$

By considering the corrosion potential E_{corr} as the reference potential the equation becomes:

$$I = I_{\text{corr}} (e^{b_a \Delta E} - e^{b_c \Delta E}) \quad (\text{II. 12})$$

With:

$$\Delta E = E - E_{\text{corr}} \quad (\text{II. 13})$$

For a Tafel reactive system, if ΔE is high enough, the anodic (or cathodic) contribution is dominant, and the anodic (or cathodic) curve is linear in a semi log graph. The anodic (or cathodic) current is extrapolated from the anodic (or cathodic) straight line at the corrosion potential.

A long sequence of repeated anodic and cathodic Tafel curves separated by an open circuit potential period between each couple of Tafel curves measurement is programmed automatically with the potentiostat pilot Software to avoid data loss. The same potential and scan rate and interval is entered for all Tafel measurements. The sequence is launched immediately after immersion of the working electrode. At the end of the experiment, all data are recovered as text files and treated with an Excel Macro.

The Tafel method was applied to extrapolate the anodic and cathodic currents. To compensate the experimental and data treatment effects on the current values, the corrosion current is given as an average of the anodic and cathodic experimental values.

$$I_{\text{corr}} = \frac{I_a + |I_c|}{2} \quad (\text{II. 14})$$

The discrete corrosion potential and current couples versus their corresponding times are presented in a double ordinates axis to follow their evolution during pickling and over-pickling process. Both pickling steps and electrochemical contribution in pickling kinetics can be shown with this method.

$$(E_{\text{corr}}, I_{\text{corr}}) = f(t_i) \quad (\text{II. 15})$$

E_{corr} : Discrete corrosion potential values

I_{corr} : Discrete corrosion current values

t_i : Discrete dissolution times

Electrochemical Impedance Spectroscopy:

Impedance Z of an electrochemical system is the ratio between an oscillating potential excitation ΔE around a potential E applied on the system and the oscillating current ΔI response of this system.

If ΔE is a sinusoidal excitation, ΔI is also a sinusoidal response but with a phase difference.

$$\Delta E = |\Delta E| \sin(2\pi f t) \quad (\text{II. 16})$$

$$\Delta I = |\Delta I| \sin(2\pi f t + \theta) \quad (\text{II. 17})$$

$|\Delta E|$: Potential oscillation amplitude (V)

$|\Delta I|$: Current oscillation amplitude (A)

f : Frequency (Hz)

θ : Phase change (rad)

Z is a complex number with a resistance dimension. For practical reasons, it is expressed with a resistance by surface dimension.

$$Z = \frac{\Delta E}{\Delta I} = Z_r + jZ_j = |Z| e^{j\theta} \quad (\text{II. 18})$$

Z : Impedance ($\Omega \cdot \text{cm}^2$)

Z_r : Real part of impedance ($\Omega \cdot \text{cm}^2$)

Z_j : Imaginary part of impedance ($\Omega \cdot \text{cm}^2$)

$|Z|$: Modulus of impedance ($\Omega \cdot \text{cm}^2$)

θ : Phase of impedance (rad)

The Electrochemical Impedance Spectroscopy method gives impedance values versus decreasing excitation frequencies spectra. The results are represented in impedance diagrams where combination of impedance elements is chosen to emphasize on specific electrical aspects of the system.

The objective of interpretation of impedance diagrams and values is to elaborate a model describing the electrochemical interface. The model can be represented by an equivalent circuit or general kinetic equation which fit the experimental values and correspond to the physical reality of the electrochemical system.

In this study, the EIS was used to elaborate a model describing scale and metallic substrate dissolutions and to estimate electrical resistance, effective capacitance and effective surface during pickling. Impedance measurements were conducted on scaled and scale free samples at discrete times of pickling.

The EIS results have shown an equivalent circuit represented by an electrolyte resistance R_E in series with a constant phase element CPE parallel to a polarization resistance R_P . In this study, the parallel polarization resistance corresponds to the charge transfer resistance R_T :

$$R_P = R_T \quad (\text{II. 19})$$

The impedance of a CPE is given by:

$$Z_{CPE} = \frac{1}{Q(j2\pi f)^\alpha} = \frac{1}{Q(2\pi f)^\alpha} [\cos(\frac{\alpha\pi}{2}) - j \sin(\frac{\alpha\pi}{2})] \quad (\text{II. 20})$$

α : CPE parameter, dimensionless, $\alpha < 1$, $\alpha = 1$ for a perfect capacitor

Q : CPE parameter, ($F s^{(\alpha-1)} cm^{-2}$), has a capacitance dimension for $\alpha = 1$.

CPE parameters α and Q can be extracted graphically. On the imaginary part of impedance versus the frequency curve plotted in a logarithmic diagram, α corresponds to the inverse of the slope of the regression straight line at the high frequency range.

Once α estimated, Q values are calculated from the imaginary part Z_j with:

$$Q = -\frac{1}{Z_j(f)(2\pi f)^\alpha} \sin(\frac{\alpha\pi}{2}) \quad (\text{II. 21})$$

Q is almost constant in the high frequency range; its average value is calculated in this range and sometimes written as Q_{HF} .

The electrolyte resistance R_E and the parallel resistance R_T values were obtained by regression method using CPE parameters values extracted graphically and the equivalent circuit global equation:

$$Z = R_E + \frac{R_T}{1 + (j2\pi f)^\alpha R_T Q} \quad (\text{II. 22})$$

The effective capacitance C_{eff} was extrapolated from the CPE parameters and resistances with two different approaches:

Power law model

This model was developed by [108-111] to analyze the impedance response of a passive film with a CPE behaviour caused by a **normal distribution** of time constants (Figure II. 1).

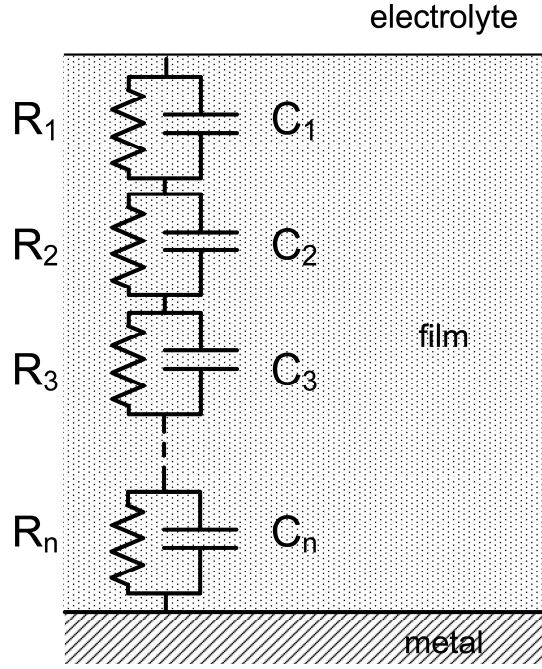


Figure II. 7: Schematic representation of a normal distribution of time constants resulting in a distributed time-constant behaviour that, for an appropriate time-constant distribution, may be expressed as a CPE [112].

According to this model, the CPE parameters Q and α can be related to physical parameters of the film with the equation:

$$Q = \frac{(\epsilon\epsilon_0)^\alpha}{g\delta\rho_\delta^{1-\alpha}}$$

ϵ : permittivity of the film

ϵ_0 : permittivity of vacuum, $8.85 \cdot 10^{-14} \text{ F.cm}^{-1}$

δ : film thickness, cm

ρ_δ : resistivity at the film/electrolyte interface, $\Omega \cdot \text{cm}$

g : numerical function given by:

$$g = 1 + 2.88(1 - \alpha)^{2.375} \quad (\text{II. 23})$$

By definition, the capacitance is related to the film thickness with the equation:

$$C = \frac{\epsilon\epsilon_0}{\delta} \quad (\text{II. 24})$$

The effective capacitance of the Power Law model C_{PL} can be estimated from the CPE parameters with equation:

$$C_{PL} = (\epsilon\epsilon_0)^{1-\alpha} gQ\rho_\delta^{1-\alpha} \quad (\text{II. 25})$$

Brug's model

This model was developed by [113] to analyze the impedance response of electrodes showing a CPE behavior caused by a **surface distribution** of time constants and to extract the effective capacitance (Figure II. 8).

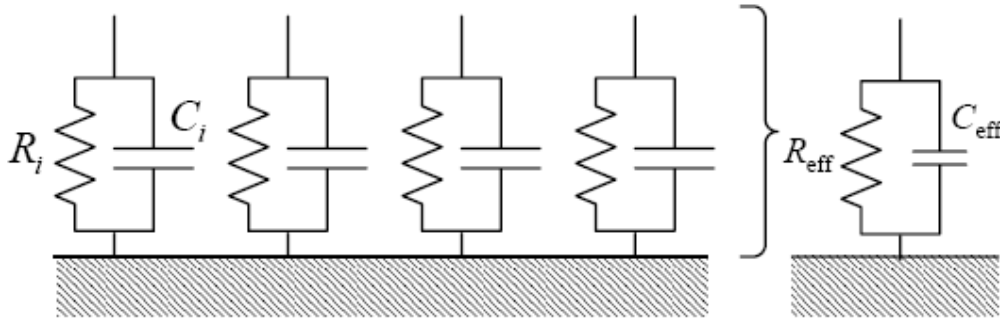


Figure II. 8: Schematic representation of a surface distribution of time constants resulting in a distributed time-constant behaviour that, for an appropriate time-constant distribution, may be expressed as a CPE [112].

According to [113], the effective capacitance is related to the CPE parameters with the formula:

$$C_{Surf} = \frac{(RQ)^{1/\alpha}}{R} \quad (\text{II. 26})$$

Where R is defined by:

$$\frac{1}{R} = \frac{1}{R_E} + \frac{1}{R_T} \quad (\text{II. 27})$$

In the case of $R_T \gg R_E$, $R = R_E$. For conductive phases, the effective capacitance C_{eff} corresponds to a double layer capacitance C_{DL} :

$$C_{DL} = \frac{(R_E Q)^{1/\alpha}}{R_E} \quad (\text{II. 28})$$

CPE parameters Q and α , charge transfer resistances R_T and effective capacitances C_{PL} or C_{DL} were estimated from impedance diagrams with the most adequate model and plotted versus scale dissolution time.

II. 4. 2. ICP-AES setup and method

An electrochemical cell coupled with an ICP-AES (Inductively Coupled Plasma Atomic Emission Spectroscopy) device was developed by [114-116] in ArcelorMittal

Maizières Research centre to quantify continuously the amount of dissolved elements at open circuit potential, potentiostatic or galvanostatic conditions.

The global experimental setup connecting the electrochemical cell and its potentiostat on one side and the ICP-AES bloc on the other side is shown in Figure II. 9.

To fit in the electrochemical cell, the sample must have at least two flat and parallel surfaces and a 10x20 mm² dimensions for the dissolved surface. The surface to be dissolved of the sample is pressed against the hole of the flow solution chamber with a hydraulic piston. A rubber joint is placed around the solution chamber hole to avoid air or solution leaks during solution pumping. The contact between the solution and the sample surface is made on a 5x15mm² surface. A thin and small metallic sheet is placed between the polished surface of the sample and the hydraulic piston; it is connected to the working electrode wire with pincers to ensure the electrical contact with the potentiostat.

Before placing the different electrodes in their compartments, the system is purged with the electrolyte to remove contaminations. The reference and auxiliary electrodes are immersed in the compartment separated from the solution flow chamber by a semi selective membrane to avoid metallic cations contaminations. A by-pass is used to diversify the electrolyte flow from the cell while placing the sample.

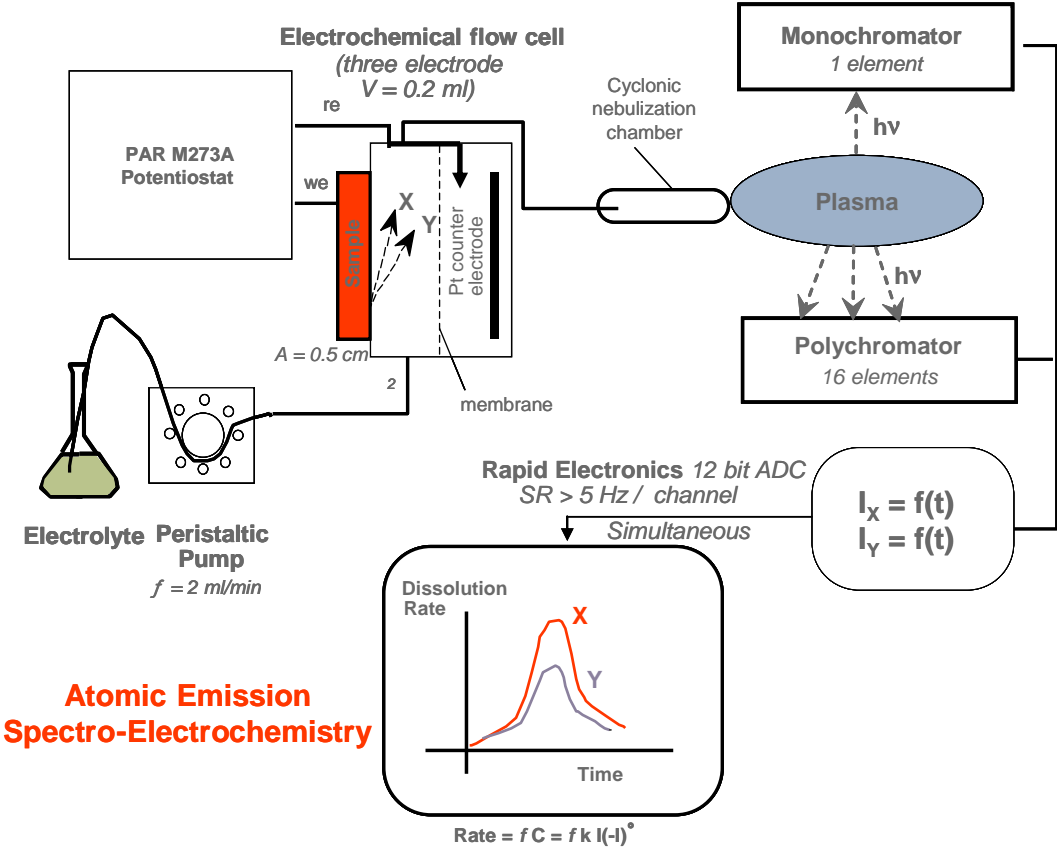


Figure II. 9: ICP-AES experimental setup inspired from [116]

The ICP-AES allows the multi-element analysis in the electrolyte downstream from the dissolution cell, but in the present case only the iron and silicon concentrations were followed. The spectrometer is a commercial set-up from Jobin-Yvon, Inc. (JY ULTIMA 2) using an argon plasma source consisting of a 40 MHz, 1 kW inductively coupled plasma, into which the electrolyte sample is continuously aspirated. In the flow cell used, the working electrode of the electrochemical cell is in an anodic small compartment (0.2 mL of electrolyte), which is separated by a membrane from an adjacent compartment containing the reference and counter electrodes. The electrolyte passes through the cell with a flow rate of about 2.5-3 mL/min and the iron and silicon composition of the electrolyte is measured in real time. Previous calibration of the set-up allowed the establishment of the relationship between dissolution rate and concentration, taking into account the time resolution of the hydraulic system.

In the ICP-AES software iron and silicon were chosen as monitored elements. Solutions at three well defined concentrations of each element are passed with a fixed debit in ICP to obtain the correlation between the AES intensity unit and the corresponding mass or mole numbers units. The electrochemical data coming from the potentiostat are also transformed into AES intensities expressed with AES arbitrary units. The same procedure is followed for the potential and current by using a dummy cell in potentiostatic and galvanostatic modes.

Two sequences were programmed in the ICP-AES software giving different curves after data treatment with a Macro spreadsheet.

- Open circuit potential: the total dissolution measured without perturbation of scale

$$(n_{Fe}, n_{Si}, E) = f(t) \quad (\text{II. 29})$$

- Applied potential: reveals the effect of an applied potential on the total dissolution rate

$$(n_{Fe}, n_{Si}, I) = f(t) \quad (\text{II. 30})$$

n_{Fe} : number of mole of iron passed in the solution ($\text{mmol.s}^{-1}.\text{cm}^{-2}$)

n_{Si} : number of mole of silicon passed in the solution ($\text{mmol.s}^{-1}.\text{cm}^{-2}$)

E: open circuit potential (V/SCE)

I: Corrosion current at a fixed applied potential (mA)

The ICP-AES gives the total dissolution rate of each element. The comparison between these values and the corrosion current values obtained by Tafel method gives an estimation of the electrochemical contribution in pickling at the corrosion potential.

II. 5. Scale characterization after pickling and over-pickling

After pickling or over-pickling tests in the electrochemical cell, the rotating electrode is extracted from the acid solution, the sample is removed from the rotating electrode sample holder, cleaned with ethanol to remove the acid solution drop and remaining scale and put under vacuum to protect the surface from dust and atmospheric corrosion. In the ICP-AES cell, the sample is removed from its lodge and follows the same treatment as for the one in the electrochemical cell.

The sample surface was observed with a LEICA[®] S440 SEM or Zeiss[®] Ultra 55 SEM-FEG after a low pressure carbon deposition treatment to facilitate electrical charges evacuation. A global first micro-graph is taken to identify the phases on the surface corresponding to different pickling levels; they are distinguished with their brightness in the SEM backscattered electrons mode. Then zooms on each zone are performed to observe the form and roughness of the surface with the secondary electrons mode and identify its composition with EDS.

For over-pickling tests done on polished steel samples at different temperatures and applied potentials, an optical microscope and a Zygo[®] NewView[®] interferometric microscope observations were performed on over-pickled surfaces after increasing immersion times. Sample surface is cleaned with ethanol after each test and observed immediately in parts of the surface to evaluate its roughness and morphology. The surface roughness data were treated with a MountainsMap[®] proTM[®] software. The results were presented as roughness cartographies or parameters. Two roughness parameters were chosen:

- **Sq**: the standard deviation of the height distribution of the surface.
- **Sz**: the average difference between the highest height peaks and lowest valleys.

The evolution of these two parameters and the roughness cartographies during over-pickling were analysed to study the distribution and amplitude of roughness.

III. Oxidation and scale characterization of silicon alloyed steels

Summary

III. 1. Introduction 69

III. 2. Steel substrate properties 70

III. 3. Oxidation mechanisms 70

III. 3. 1. Low carbon steel oxidation 70

III. 3. 1. 1. Oxidation kinetics 70

III. 3. 1. 2. Oxidation mechanism..... 72

III. 3. 2. Effect of Silicon content on oxidation..... 72

III. 3. 2. 1. Oxidation kinetics 72

III. 3. 2. 2. Oxidation mechanism..... 74

III. 4. Scale characterization 75

III. 4. 1. Low carbon steel scale properties 75

III. 4. 2. Silicon steel scales properties..... 76

III. 5. Conclusions 81

III. 1. Introduction

In the hot strip mill process, steel surface is in contact with humid air at high temperatures: from nearly 1200°C (reheating furnace) to nearly 700°C (coiling). At these conditions an oxide layer called commonly “scale” is formed. It is usually removed by dissolution in an acid bath to recover a clean steel surface. For non alloyed steels, scale is mainly composed of iron oxides and dissolved easily in pickling baths.

Some alloying elements such as Si, Mn, Al are added to steel to reach high level of mechanical properties like elasticity limit, strain strength, elongation, formability and crash worthiness. These elements segregate at high temperatures towards the scale/metal interface forming mixed oxides for silicon and aluminium or solid solutions in scale for Mn [59, 61, 117]. The presence of these oxides in scale and at the steel/metal interface affects the pickling efficiency.

In this study, the focus is put on silicon effect on scale formation kinetics and chemistry during oxidation at hot strip mill temperatures. Silicon is present in Alloyed High Strength Steels (AHSS) to improve their mechanical and corrosion resistance, as well as in electrical steels for improving the electrical resistivity, which is an important property for applications as the core material of electro-magnetic devices such as motors [5, 7, 9].

The elaboration of new silicon alloyed steel grades and the difficulties to pickle them triggered many recent studies on the effect of silicon on oxidation kinetics and final scale morphology. Some of these studies proposed some oxidation mechanisms for silicon alloyed samples but were limited to medium silicon alloyed grades and did not correspond completely to the Hot Strip Mill conditions [12, 21, 37, 43, 49].

According to Atkinson [35] and Adachi *et al.* [36] silicon contained in steel is first oxidized into silica which forms an interfacial sub-layer between wüstite and steel. The internal oxidation of steel can be also observed (oxide particles inside the steel), especially for the steel containing more than 0.3 wt.%Si. Genève [118] pointed out that scale adhesion is lower on Si steels than in that of FeO on pure Fe. On the contrary, adhesion between silica or fayalite and the substrate is strong: leading to an increased difficulty to remove scale containing silicate phases during pickling. Above 1177°C, FeO-Fe₂SiO₄ [54] eutectic melts and infiltrates scale and steel grain boundaries. The penetration depth into the scale increases with the Si content, while that into the substrate varies slightly. The presence of liquid phase improves the scale adhesion for steels containing less than 0.5 wt.%Si, but for higher Si contents (up to 1.5 wt.%) the tendency is inversed.

In our study, temperature and humidity conditions corresponding to those in the hot strip mill were applied on a medium and a highly silicon alloyed steel grades to determine the silicon effect on scale formation kinetics and the chemistry of the resulting scale.

III. 2. Steel substrate properties

Three grades with silicon contents 0.02 wt.%Si (Si00), 1.6 wt.%Si (Si16) and 3.2 wt.%Si (Si32) were chosen, their chemical composition is given in Table II.1. Si00 is the low carbon steel reference. Si16 and Si32 are the intermediate and high silicon alloyed grades respectively.

III. 3. Oxidation mechanisms

III. 3. 1. Low carbon steel oxidation

III. 3. 1. 1. Oxidation kinetics

The mass gain per surface unit ($\Delta m/S$) of non-alloyed sample Si00 during oxidation in 15% humid air, at temperatures 900-1200°C is reported in Figure III. 1. For non-alloyed sample Si00 at all oxidation temperatures, scale growth first follows a linear law (1) then a parabolic law (2).

Mass gain laws can be described by following formulas:

- First linear step:

$$(\Delta m / S) = k_l . t \quad (\text{III. 1})$$

- Parabolic step:

$$(\Delta m / S)^n = k_p . t \quad (\text{III. 2})$$

With $n > 1$

$$k_i = k_{i0} . e^{-\frac{Q}{RT}} \quad (\text{III. 3})$$

According to Arrhenius law (III. 3) k_i is the kinetic constant (k_l for the linear part and k_p for the parabolic part), Q is the activation energy and R the gas constant. The value of n in the parabolic law varies from 1 to 2 during the linear-parabolic transition period before being fixed to 2 after few minutes of oxidation.

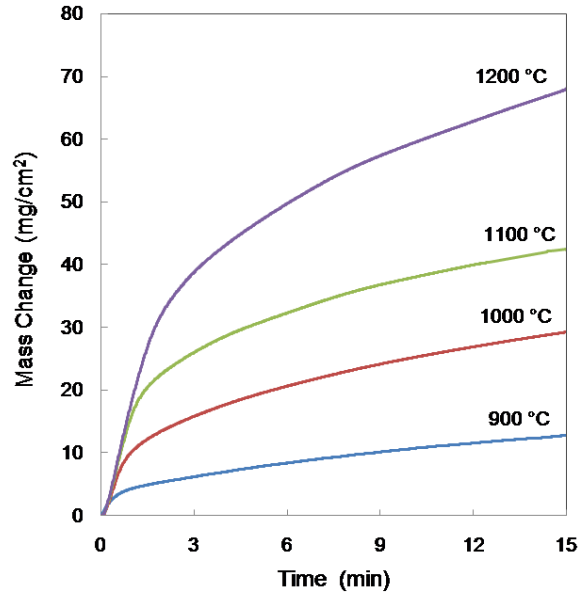


Figure III. 1: Mass gain of Si00 during oxidation in 15% humid air at temperatures 900-1200°C.

Kinetics parameters for linear and parabolic parts of oxidation of Si00 were evaluated at the four tested temperatures. They are reported in Table III. 1 (k_l and k_p for the different oxidation temperatures and silicon contents). On an Arrhenius diagram representing the variation of the linear and parabolic kinetics constants as a function of $(1/T)$ on a logarithmic scale, the slope of the regression straight line gives an estimation of the activation energy Q for the linear and parabolic steps of oxidation: $Q_l = 54 \text{ kJ mol}^{-1}$ and $Q_p = 144 \text{ kJ mol}^{-1}$, as well as the origin of the kinetics constants $k_{l0} = 2.4 \times 10^3 \text{ mg cm}^{-2} \text{ min}^{-1}$ and $k_{p0} = 3.04 \times 10^7 \text{ mg cm}^{-2} \text{ min}^{-1}$.

(a)

T \ Sample	Si00	Si16	Si32
900°C	8.50	4.69	1.60
1000°C	14.98	3.95	1.55
1100°C	19.13	1.88	1.50
1200°C	20.55	28.31	32.60

(b)

T \ Sample	Si00	Si16	Si32
900°C	10.50	7.18	1.50
1000°C	47.46	14.98	0.11
1100°C	88.00	84.58	0.09
1200°C	238.00	460.94	975.90

Table III. 1: Oxidation kinetics parameters: (a) k_l ($\text{mg cm}^{-2} \text{ min}^{-1}$) and (b) k_p ($\text{mg}^2 \text{ cm}^{-4} \text{ min}^{-1}$).

Linear and parabolic kinetics constants, as well as the resulting mass gain values during oxidation in 15% humid air for non alloyed steels, increase with temperature (Table III. 1)

III. 3. 1. 2. Oxidation mechanism

The first linear step, which takes some seconds, corresponds to the formation of continuous iron oxide layer (scale) on the steel surface, and then the scale growth is decelerated in a transition regime to follow a parabolic law. This indicates that the oxidation reaction is controlled by the diffusion of Fe^{2+} through the scale layer vacancies towards the surface in contact with the oxidizing atmosphere [22, 23, 48].

III. 3. 2. Effect of Silicon content on oxidation

III. 3. 2. 1. Oxidation kinetics

The effect of intermediate content of silicon on mass gain during oxidation of Si16 in the same temperature range 900-1200°C is shown in Figure III. 2. For oxidation temperatures lower than 1100°C, the mass gain follows the initial linear law but for a very short time, less than 10 seconds, then stagnates during 30 seconds to 2 minutes depending on oxidation temperature. After this passivation period, the scale growth follows a parabolic law at all temperatures. The mass gain of Si16 at 1200°C shows higher values compared to lower temperatures. The curve profile is also different; the passivation period has completely disappeared and the linear then the parabolic steps similar to those of Si00 are observed.

Oxidation kinetics parameters of Si16 are reported in Table III. 1. The intermediate content of silicon reduces the initial linear constants values compared to Si00 at the same oxidation temperatures except for 1200°C where a higher k_l is observed. The post passivation period kinetics constant k_p increases with increasing oxidation temperatures.

In Figure III. 3, the high silicon content of Si32 induces much longer passivation periods especially at 1000°C and 1100°C in comparison with Si16. This passivation effect disappears at 1200°C.

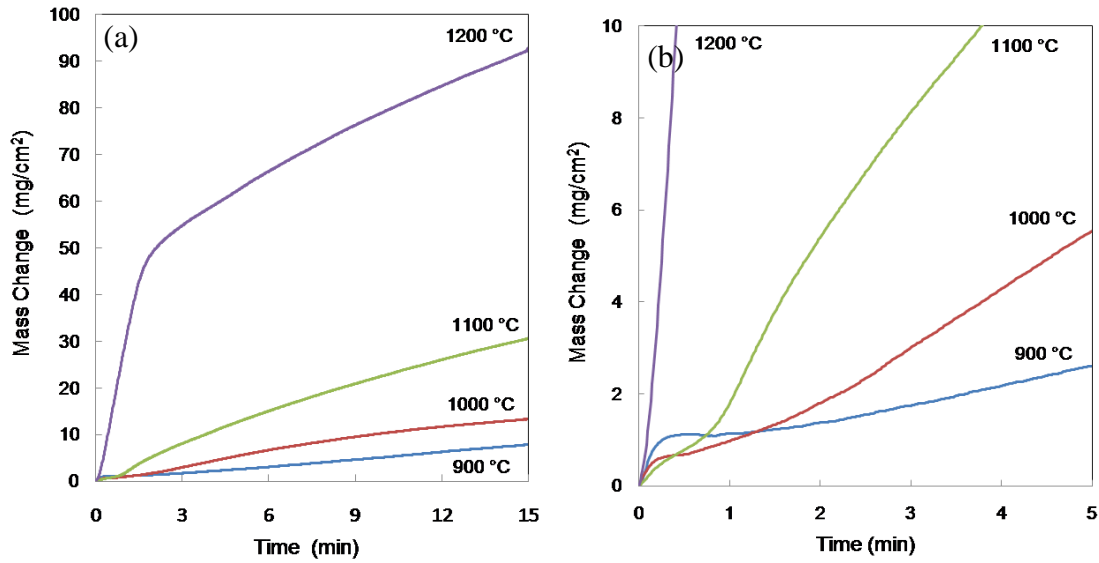


Figure III. 2: Mass gain of Si16 during oxidation in 15% humid air at temperatures 900-1200°C (a) with a zoom on the passivation period (b).

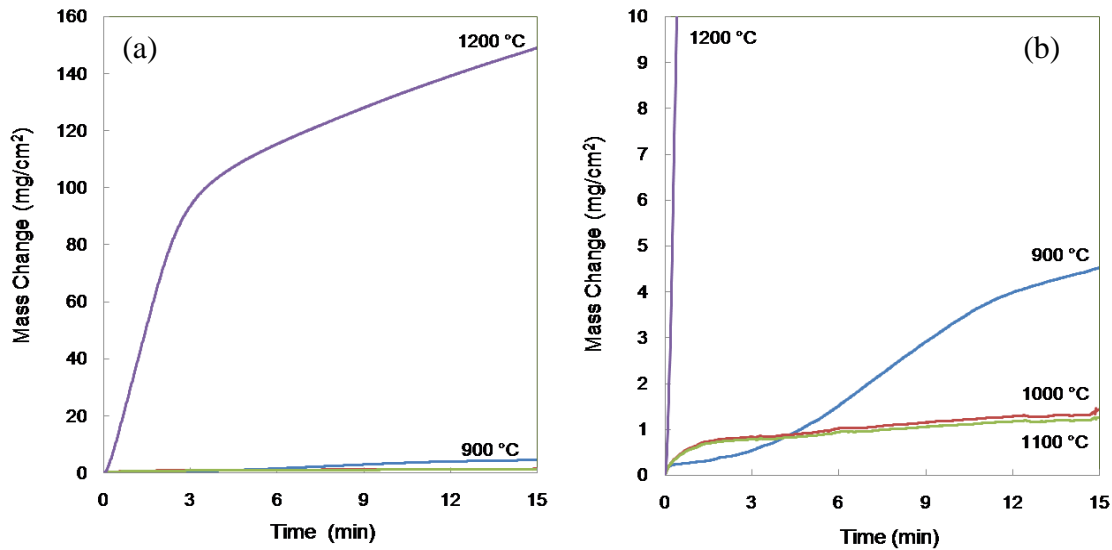


Figure III. 3: Mass gain of Si32 during oxidation in 15% humid air at temperatures 900-1200°C (a) with a zoom on temperatures $\leq 1100^\circ\text{C}$ (b).

The oxidation kinetics parameters k_l and especially k_p for Si32 are significantly affected by the long passivation period since their values are much lower compared to Si16 at 1000°C and 1100°C. However, higher k_l and k_p values are observed for oxidation at 1200°C (Table III. 1).

In Figure III. 4, the comparison of the final mass gain after 15 minutes of oxidation for all tests, confirms the switching effect of increasing silicon content for temperatures higher than 1100°C where the passivation is replaced by an acceleration of oxidation.

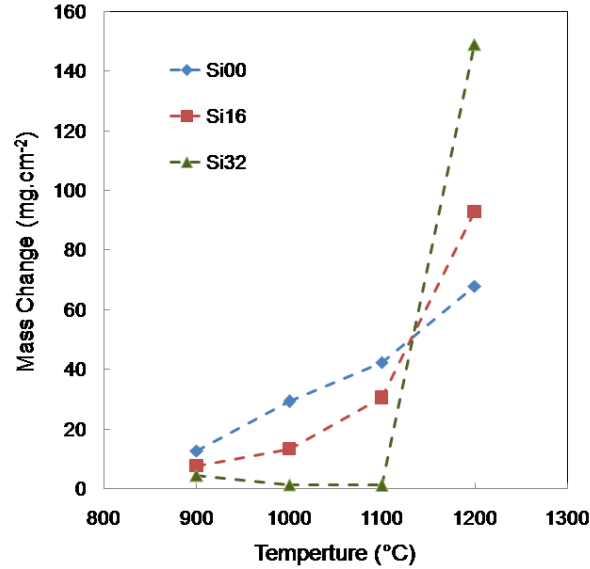


Figure III. 4: Effect of Si content and temperature on final mass change after oxidation in 15% humid air during 15 minutes.

The higher concentration of silicon and its random distribution on steel surface and the short oxidation time compared with experiments found in literature [1, 41] can explain the random kinetics values in our case and the difficulty to calculate the activation energy.

III. 3. 2. 2. Oxidation mechanism

As it will be demonstrated in the Section III.4., the passivation period is due to the formation of a thin silica layer as Si is more prone to oxidation than iron. This layer dramatically slows down the diffusion of Fe^{2+} towards the surface in contact with the oxidizing atmosphere [33, 49]. This effect increases with silicon content and temperatures between 950°C and 1100°C favourable for silica. The resulting scale is thin but rich in SiO_2 .

The oxidation passivation effect disappears at 1200°C, this is due to the formation of a Wüstite-Fayalite eutectic at temperatures higher than 1177°C [54]. This melting phase favours the diffusion of iron ions to the external oxidizing atmosphere and oxygen to the interface, accelerating the external and internal oxidation rates [1]. The diffusion coefficients of iron and oxygen in the liquid oxides (D_{Fe} in molten $FeO-SiO_2$ around $8 \times 10^{-5} \text{ cm}^2 \text{ s}^{-1}$ at 1250°C [53], D_O (or D_{Fe}) in liquid iron oxides around $2.5 \times 10^{-3} \text{ cm}^2 \text{ s}^{-1}$ at 1400°C and $3 \times 10^{-3} \text{ cm}^2 \text{ s}^{-1}$ at 1615°C [31, 32]) are higher by several orders of magnitude than the diffusion coefficients in the solid silicon oxide (D_{Fe} in silica around $1.5 \times 10^{-10} \text{ cm}^2 \text{ s}^{-1}$ at 1100°C [1, 52]).

III. 4. Scale characterization

III. 4. 1. Low carbon steel scale properties

In the oxidation conditions of this study, the resulting non alloyed steel (Si00) scale is homogenous and essentially composed of a wüstite layer covered by a magnetite thinner layer (Figure III. 5a). Below 570°C wüstite is unstable: it transforms into iron and magnetite eutectoid. However, this transformation enables very low cooling rates. Considering a post oxidation cooling speed of about 40 °C min⁻¹ in all experiments of this study, the wüstite transformation can be assumed for low part of scale volume, which is not clearly visible on SEM even at high magnification [19, 58].

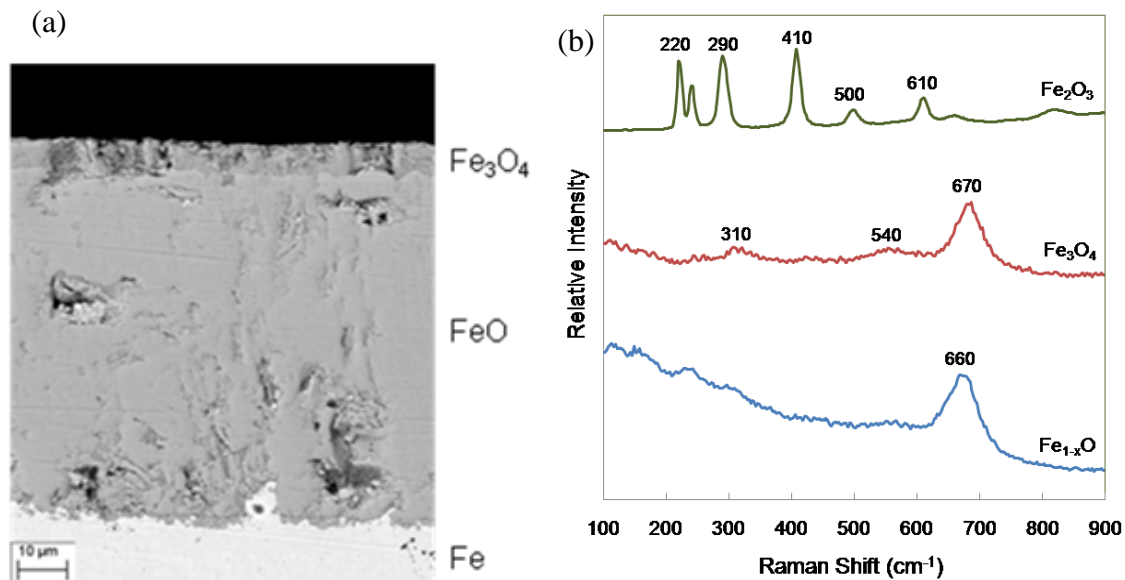


Figure III. 5: (a) Cross-section SEM micrograph of Si00 after oxidation at 850°C in 15% humid air during 15 minutes with (b) Raman spectra of its scale phases: hematite external surface, magnetite layer and wüstite layer.

Si00 scale layers and their Raman spectra are presented in Figure III. 5b. On the scale top surface, Raman analysis reveals the presence of a hematite layer with intense peaks at 220 cm⁻¹ and 290 cm⁻¹ and 410 cm⁻¹, as well as small peaks at 500 and 610 cm⁻¹. This layer is very thin and not visible on SEM micrograph of the sample cross-section. Raman characterizations performed on cross-section do not distinguish clearly magnetite from wüstite. The Raman spectrum provided on external layer corresponds well to the spectrum of magnetite (Fe₃O₄) with characteristic peaks at 310 cm⁻¹, 540 cm⁻¹ and 670 cm⁻¹. Wüstite phase (FeO) is cubic and should not be visible on Raman spectra. However, a peak at 660-670 cm⁻¹ was observed

during Raman analyses on the internal layer [105, 119]. This peak could be attributed to the presence of vacancies in the wüstite microstructure (wüstite Fe_{1-x}O with relatively large x variation according to the phase diagram [19]) or partial wüstite transformation during cooling into $\text{Fe} + \text{Fe}_3\text{O}_4$ eutectoid (presence of magnetite areas).

EDS analyses gives the chemical composition of the low carbon steel scale layers. The external and internal layers compositions are close to Fe_3O_4 and FeO respectively (Table III. 2).

Element (at. %)	Phase		
	Magnetite	Wüstite	Fayalite
Fe	43.6	49.4	35.0
O	56.4	50.6	48.9
Si			16.1

Table III. 2: Chemical composition of scale phases with EDS.

The presence of the two external layers with iron oxidation degrees higher than that of wüstite comes from the continuous oxidation of iron diffusing through lattice vacancies and the presence of oxygen at high concentration in the outer scale layers [57].

The increase in the oxidation temperature and duration increases the scale thickness. For very high oxidation temperatures and durations, a gap appears at the scale/metal interface due to the difference of dilatation coefficients of steel and scale limiting the diffusion of iron to form wüstite. This leads to the formation of thicker magnetite and hematite layers above wüstite [23, 41].

III. 4. 2. Silicon steel scales properties

As for the scale growth kinetics, the scale morphology for silicon alloyed steels is very dependent on silicon content and oxidation temperature.

For Si16 grade, wüstite and magnetite layers similar to those of Si00 are observed as external layers. Between steel and wüstite, an internal sub-layer composed of silicon-iron oxides appears. The morphology of this phase depends on oxidation temperature (Figure III. 6 and Figure III. 7).

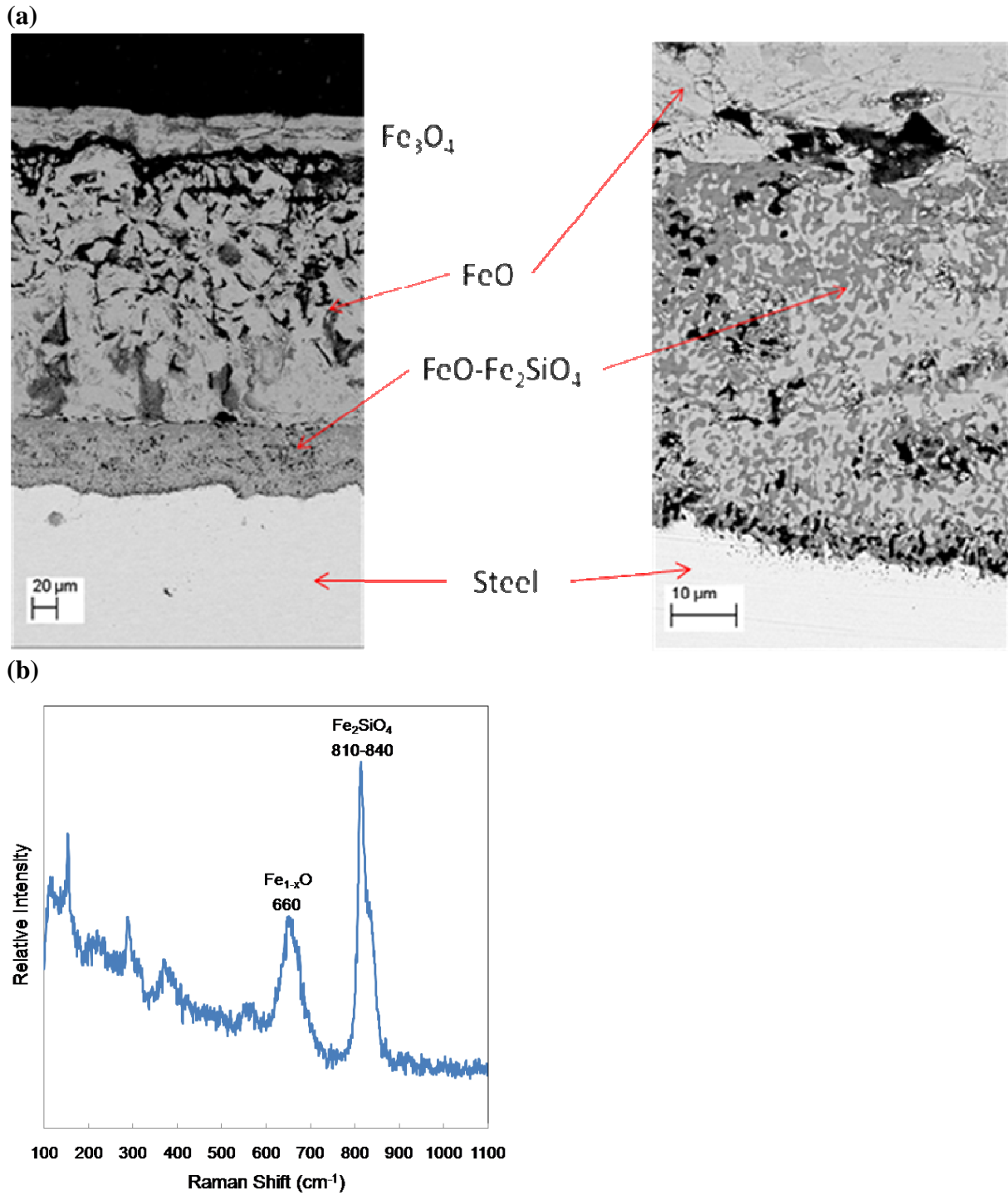


Figure III. 6: (a) Cross-section SEM micrograph of Si16 oxidized at 1100°C in 15% humid air during 15 minutes with a zoom on fayalite-wüstite mixture layer. (b) Raman spectrum of fayalite grains in wüstite.

According to Raman and SEM analyses, between 950°C and ~1177°C (melting point of FeO + Fe₂SiO₄ eutectic) grains of fayalite appear in the wüstite matrix of the internal layer. Fayalite is clearly detected by Raman spectrometry due to its characteristic double peak at 810 and 840 cm⁻¹ (Figure III. 6) [120, 121].

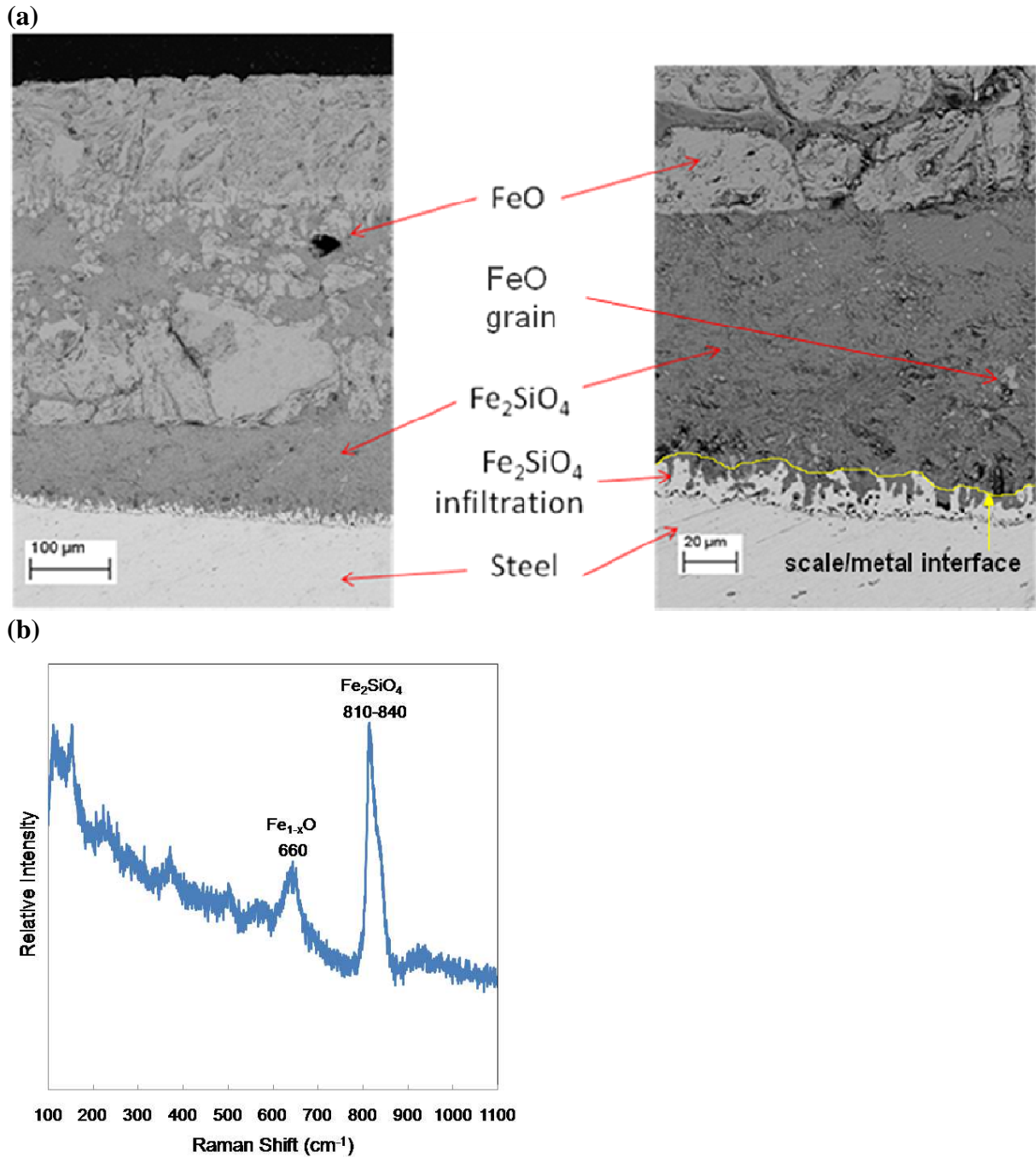


Figure III. 7: (a) Cross-section SEM micrograph of Si16 oxidized at 1200°C in 15% humid air during 1 minute with a zoom on fayalite layer. (b) Raman spectrum of fayalite layer with small wüstite grains.

Above 1180°C, a continuous layer of fayalite is observed at the steel/wüstite interface with some infiltrations at the grain boundaries of steel and wüstite layer (Figure III. 7). This layer is formed at the melting of $\text{FeO} + \text{Fe}_2\text{SiO}_4$ eutectic at these temperatures. Some wüstite small grains appear in the fayalite layer (Figure III. 7). For long oxidation times, the presence

of the thick fayalite layer leads to break-down at the steel/scale interface due to volume shrinkage during solidification and thermo mechanical stresses.

EDS analysis on fayalite zones of the internal layer confirms Raman spectroscopy results. Iron, oxygen and silicon respective atomic ratios in the iron-silicon oxide phase correspond to fayalite Fe_2SiO_4 (Table III. 2).

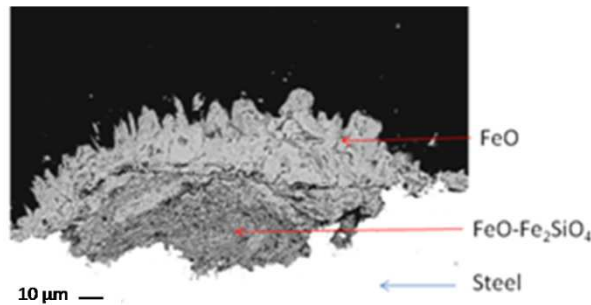


Figure III. 8: Cross-section SEM micrograph of Si32 oxidized at 1100°C in 15% humid air during 15 minutes.

For Si32 sample, the long passivation period observed at 1000°C and 1100°C during scale growth produces discontinuous scale composed of islands surrounded by a very thin passivating layer. The islands are composed of an external curved wüstite and an internal curved wüstite matrix containing fayalite grains (Figure III. 8). These islands can be formed after local rupture of the barrier layer and enhanced iron diffusion through defects or film grain boundaries [41].

To determine the nature of the passivation layer, XPS analysis were performed on the Si32 sample oxidized at 1100°C during 2 min corresponding to the beginning of passivating regime (Figure III. 9). XPS survey spectrum performed at 45° from spectrometer axis indicates the presence of iron, silicon, manganese, oxygen and carbon at the sample surface (Figure III. 9a). On oxygen (O1s) high resolution spectrum silicon oxide of SiO_2 type and hydroxide phases are clearly distinguished (Figure III. 9b). The iron and manganese oxides are also present on the sample surface, they are revealed by a peak at 529.5 eV in Figure III. 9b. The silicon (Si2p) high resolution spectrum (Figure III. 9c) reveals three elementary components: two different oxide phases containing silicon and a metallic form of silicon. The first one of the oxide phases corresponds typically to the SiO_2 [122] whereas the second one can be attributed to SiO_x ($x < 2$) or fayalite (Fe_2SiO_4).

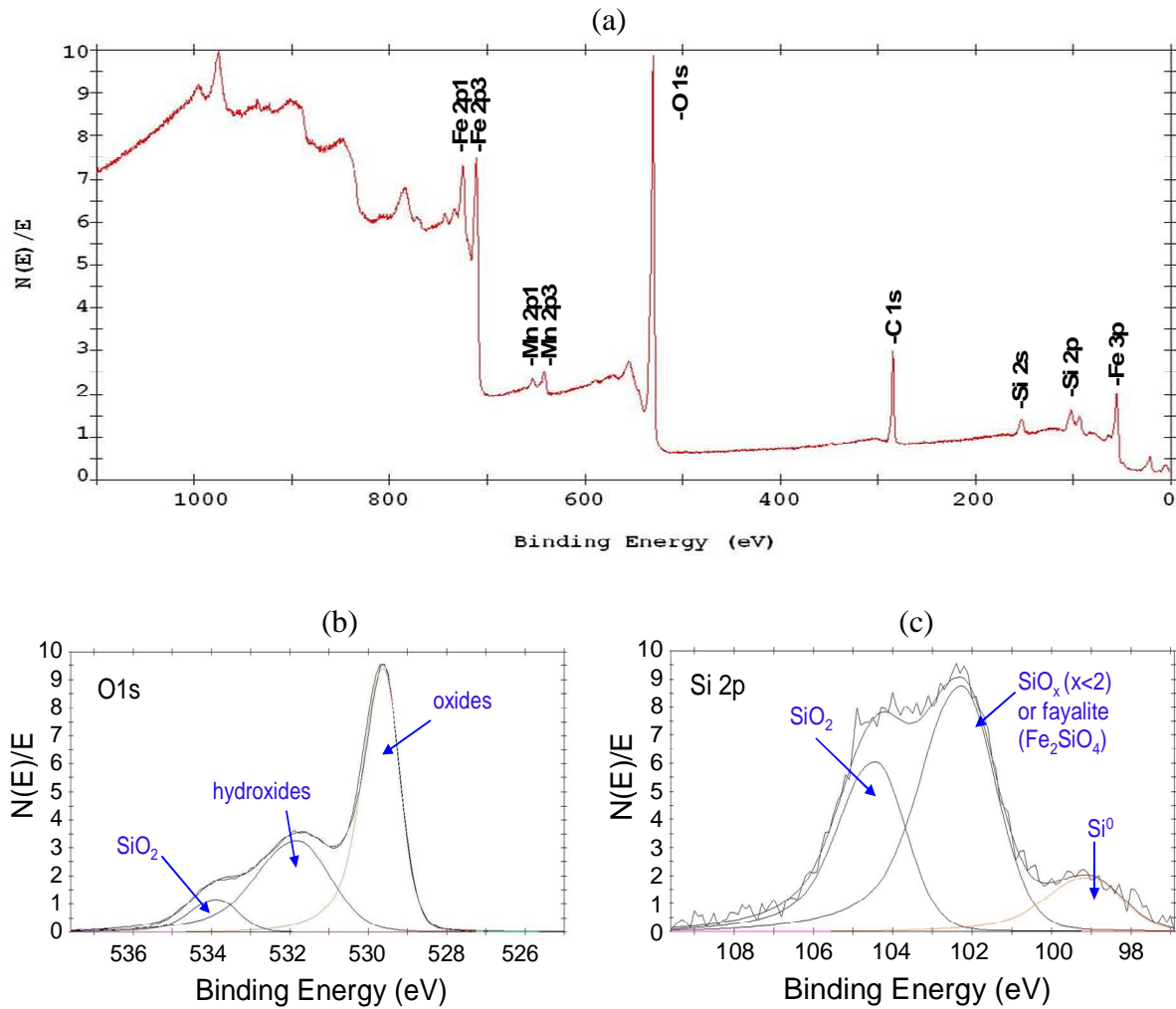


Figure III. 9: XPS analysis of Si32 sample surface after 2 minutes of oxidation at 1100°C in 15% humid air: 45° survey (a), high resolution XPS spectra of O 1s (b) and Si 2p (c).

XPS results are confirmed by SEM observations and Auger microanalysis of the sample surface (Figure III. 10). Auger spectra performed in differentiated mode show silicon enrichment in smooth areas of the sample surface corresponding to the presence of silicon oxide film (Si peak at 1619 eV and O peak at 505 eV in Fig. III. 10b). The presence of iron oxides can be seen on the surface of islands (Fe triplet transition at 598, 651 and 703 eV and O peak at 505 eV in Fig. III. 10c). These results are in good agreement with the XPS conclusions suggesting the presence of a SiO₂ layer at the surface in smooth areas between iron oxide islands. This also corroborates the observations made in the kinetics study concerning the silicon oxide layer. Formed during the first instants of oxidation, it slows down the diffusion of iron and, consequently, the scale growth (passivation period). Nevertheless, the scale continues to grow during the passivation period, yet at a small rate, a consequence of the low diffusion coefficient of iron in silicon oxide. This diffusion can occur

at the SiO₂ layer defects such as grain boundaries leading to the formation of islands (Figure III. 10a).

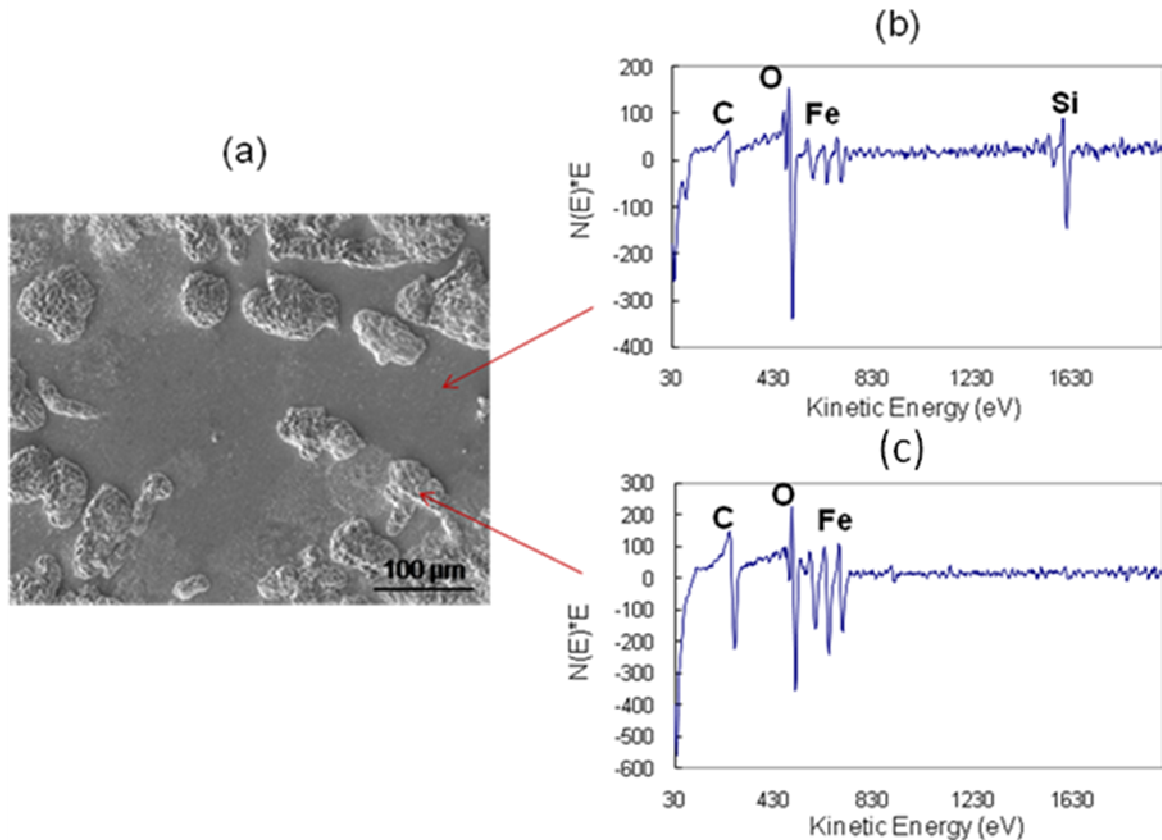


Figure III. 10: (a) SEM micrograph of Si32 sample surface after 2 minutes of oxidation at 1100°C in 15% humid air with Auger spectra in differentiated mode performed in (b) the smooth areas of the surface and (c) on iron oxide islands.

III. 5. Conclusions

Oxidation of low carbon steels follows a linear law at the beginning of oxidation then a parabolic law after a transition period. All kinetic parameters increase with temperature.

Scale of low carbon steel grade is composed of three parallel sub-layers with decreasing oxygen ratio toward the steel substrate. The hematite Fe₂O₃ outer layer is very thin and observable only on sample surface. The magnetite intermediate layer with a mixture of Fe³⁺ and Fe²⁺ is thick enough to be observable in SEM cross-section micro-graphs. The main scale sub-layer is wüstite FeO. Below 570°C, FeO is unstable and transforms partially or completely into Fe₃O₄ and Fe.

In steel oxidations at high temperatures (850-1200°C) in humid air (15% H₂O) during a short time (15 min), the addition of high amounts of silicon to steel (1.6 and 3.2 wt.%)

slows down drastically the scale growth for temperatures below 1177°C with the formation of a silica sub-layer at the beginning of oxidation.

The passivation effect disappears with the formation of FeO-Fe₂SiO₄ eutectic above 1177°C and the enhancement of Fe²⁺ diffusion. Silicon oxides are concentrated at the metal/scale interface and their morphology depends on the oxidation temperature. Fayalite grains in wüstite matrix appear between 900°C and 1100°C and continuous layer of fayalite-wüstite eutectic above 1177°C. For silicon content of 3.2 wt.% the passivation effect is so high that the resulting scale is discontinuous with islands surrounded by a silica layer.

IV. Pickling and over-pickling mechanisms of low carbon steel.

Summary

IV. PICKLING AND OVER-PICKLING MECHANISMS OF LOW CARBON STEEL.	83
IV. 1. Introduction	85
IV. 2. Model scale characteristics before pickling	85
IV. 3. Electrochemical dissolution of scale	86
IV. 3. 1. Corrosion potential E_{corr}	86
IV. 3. 2. Corrosion current I_{corr}	87
IV. 3. 2. 1. Tafel curves	87
IV. 3. 2. 2. Corrosion current evolution during scale dissolution	88
IV. 3. 3. Electrochemical Impedance Spectroscopy EIS	89
IV. 3. 3. 1. EIS diagrams	89
IV. 3. 3. 2. Evolution of charge transfer resistance R	90
IV. 3. 3. 3. Evolution of CPE parameters	91
IV. 3. 3. 4. Evolution of effective capacitance	92
IV. 4. Total dissolution of scale	94
IV. 5. Pickling and over-pickling mechanisms	95
IV. 5. 1. Pickling thermodynamics	95
IV. 5. 2. Pickling steps and reactions	96
IV. 5. 3. Over-pickling reactions	98
IV. 6. Influence of some parameters on pickling and O-P mechanism of LCS scales	99
IV. 6. 1. Scale composition and morphology	100
IV. 6. 1. 1. Influence of hematite on pickling	100
IV. 6. 1. 2. Pickling of an industrial scale	101
IV. 6. 2. Influence of acid concentration	102
IV. 6. 3. Influence of pickling bath temperature	102
IV. 6. 4. Influence of a cathodic applied potential	102
IV. 7. Steel surface after pickling and over-pickling	105
IV. 7. 1. Steel surface after insufficient pickling	105
IV. 7. 2. Steel surface after long over-pickling:	105
IV. 8. Conclusions	107

IV. 1. Introduction

Since the literature review showed that iron oxide dissolution in acid solutions is simultaneously a chemical and an electrochemical process [98, 100-102], experimental methods which allow the two mechanisms to be distinguished have to be found. While electrochemical methods provide information on the rate of electrochemical dissolution, additional analytical techniques are necessary to determine the total dissolution rate. In reference [100, 101], in situ X-ray absorption near-edge spectroscopy (XANES) was used simultaneously with electrochemical methods on synthetic oxide to determine the nature of the dissolution reaction, leading to the conclusion that dissolution of hematite and magnetite is mainly chemical in the anodic potential range, and that electrochemical dissolution of magnetite has to be taken into account in the cathodic range. Inductively coupled plasma-atomic (or optical) emission spectroscopy (ICP-AES or ICP-OES) has been shown to be a useful method for the in situ determination of material dissolution, using solution analysis in a flow cell [114, 115]. A similar approach was used in the present work on oxide layers grown on a steel substrate. Electrochemical methods such as polarization curves and impedance spectrometry were applied to estimate the rate of electrochemical dissolution, whereas the overall rate of iron dissolution in the pickling solution was followed in situ, using an analytical set-up composed of an inductively coupled plasma optical emission spectrometer (ICP-OES) placed downstream from the electrochemical flow.

From the comparison between the electrochemical dissolution rate and the rate of total iron enrichment in the pickling bath, estimation of the chemical dissolution rate will be performed.

A model low carbon scale and soft pickling conditions were chosen to study the pickling mechanism fundamentally. Then, an exploration of some oxidation and pickling parameters similar to those present on industrial lines will be done to correlate the proposed pickling mechanism with the effect of these parameters

IV. 2. Model scale characteristics before pickling

Among the different model scales described in chapter III, only the model steel scale with a homogenous layered structure was studied, for easier modeling of the dissolution mechanism. As shown previously, it is essentially composed of wüstite covered by a magnetite layer (Figure IV. 1) and an outer very thin hematite layer. The mean thickness of

the scale was about 70 μm . Below 570°C, wüstite is known to be unstable and to transform into iron and magnetite eutectoid. However, this transformation needs very low cooling rates, and, since in these experiments the cooling rate was about 40 $^{\circ}\text{C}\cdot\text{min}^{-1}$, it can be assumed that this transformation only affected a small part of the scale volume (chapter III).

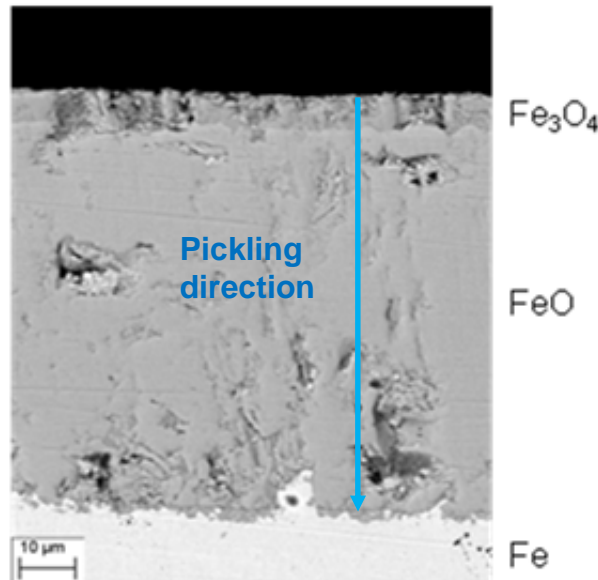


Figure IV. 1: Cross-section SEM micrograph of Si00 model scale after oxidation at 850°C in air with 15% relative humidity during 15 minutes.

The low carbon steel model scale will be called **Si00-model scale** in this chapter. The phases in contact with acid during pickling will be the hematite, the magnetite and the partly decomposed “wüstite”, containing wüstite, magnetite and iron and at the end the steel substrate starting over-pickling.

IV. 3. Electrochemical dissolution of scale

IV. 3. 1. Corrosion potential E_{corr}

From an experimental point of view, the corrosion potential of the sample during the pickling process is easy to follow continuously. The results are given in Figure IV. 2. At the beginning of immersion, the open circuit potential (OCP) was well defined and had a value of about + 0.4 V/SCE. Such a positive value has also been reported for sputtered hematite and magnetite and was attributed to a passive-like behaviour [101]. During the first 9 hours of immersion, the OCP decreased to + 0.15 V/SCE and then increased again to + 0.3 V/SCE. This value was maintained for a period of 3 hours, after which an almost instantaneous jump

was observed to a value of - 0.5 V/SCE, which is close to the OCP measured on bare steel in the same electrolyte. After the jump the OCP kept a roughly constant value.

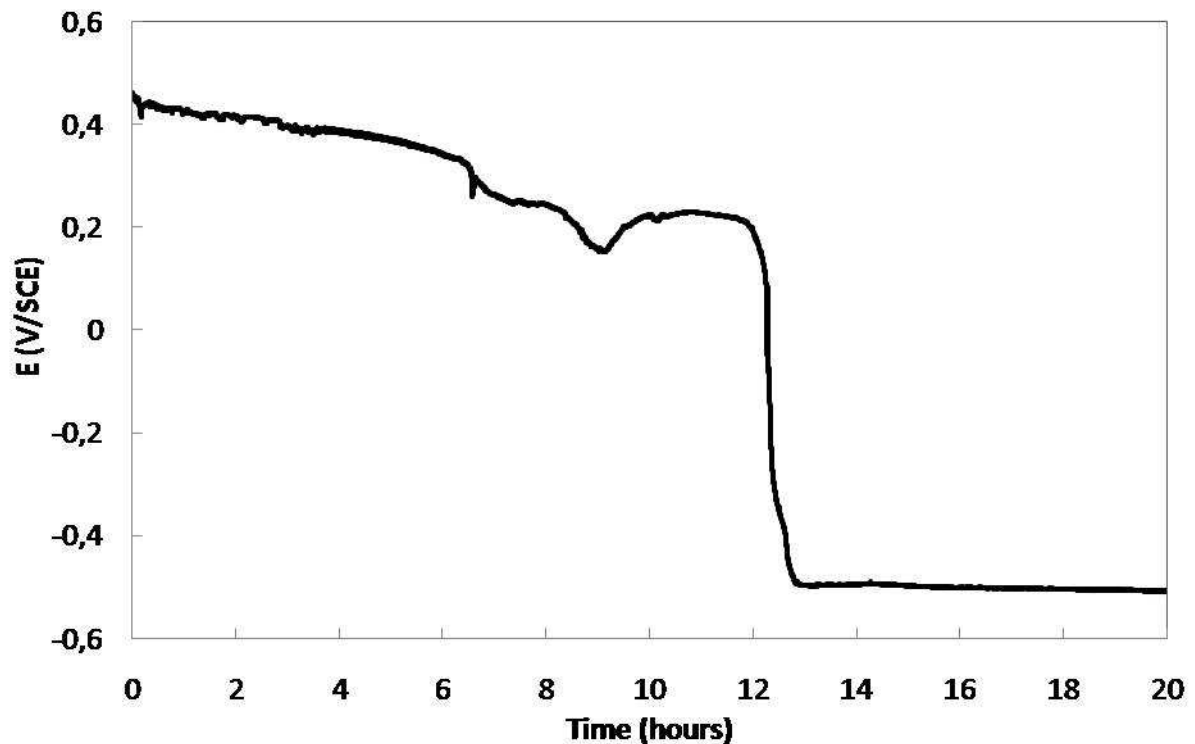


Figure IV. 2: Evolution of corrosion potential during scale dissolution in 1M HCl acid solution at room temperature.

IV. 3. 2. Corrosion current I_{corr}

IV. 3. 2. 1. Tafel curves

Potentiodynamic measurements were performed in the anodic and cathodic potential ranges, showing a Tafel behaviour in the cathodic range. The corrosion current (I) could then easily be determined by extrapolating $\log I$ to the OCP.

Every 0.5 hour, current density-potential curves were recorded around the OCP, but in a restricted potential range to avoid significant modification of the scale by polarization. Three examples of these curves are given in Figure IV. 3. In addition, the current density-potential curves for a steel electrode without oxide are also plotted as a reference, leading to an estimate of $80 \mu\text{A}\cdot\text{cm}^{-2}$ for the corrosion current density ($E_{\text{corr}} = - 0.5 \text{ V/SCE}$).

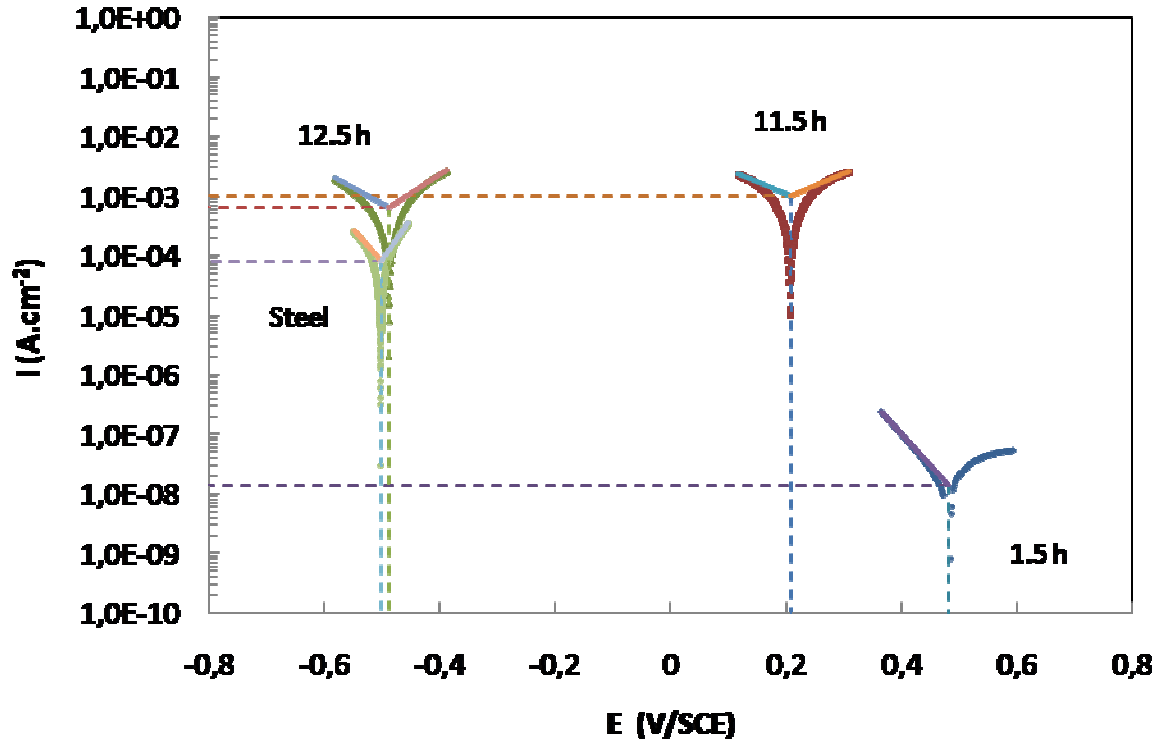


Figure IV. 3: Current-potential curves (scan rate 1 mV/s) plotted for different immersion times (1.5 h, 11.5 h and 12.5h), for scale covered and scale free steel electrodes.

IV. 3. 2. 2. Corrosion current evolution during scale dissolution

The corrosion current density determined from current-potential curves is plotted as a function of immersion time in Figure IV. 4. The corresponding OCP value is also reported, and appears to vary similarly to the variations given in Figure IV. 2. The differences between the temporal evolutions of potential reported in Figure IV. 2 and Figure IV. 4 are likely to be due to the perturbation of the sample by the polarization measurements imposed each 30 minutes for the corrosion current determination.

At the beginning of immersion, the corrosion current density was very low, with a value of about $5 \times 10^{-2} \mu\text{A}\cdot\text{cm}^{-2}$. This low value is in agreement with the presence of a hematite layer and with the value usually measured in the presence of a passive layer. The current increases monotonically, up to the potential jump which is observed after 12 hours. The increase in the corrosion current density is likely to be linked to the decrease of the area protected by the hematite and to the penetration of the electrolyte in the oxide layer. It is noticeable that after 12 hours of immersion the corrosion current density reached a value of $1 \text{ mA}\cdot\text{cm}^{-2}$ and kept about the same value after the potential jump. This result is surprising, because due to the potential jump of about 700 mV the electrochemical reactions are normally

expected to be completely different before and after the potential jump. As shown in Figure IV. 4, within a period of 12 hours of immersion, the corrosion current density increased by more than 4 orders of magnitude passing from 5.10^{-5} to 1 mA.cm^{-2} .

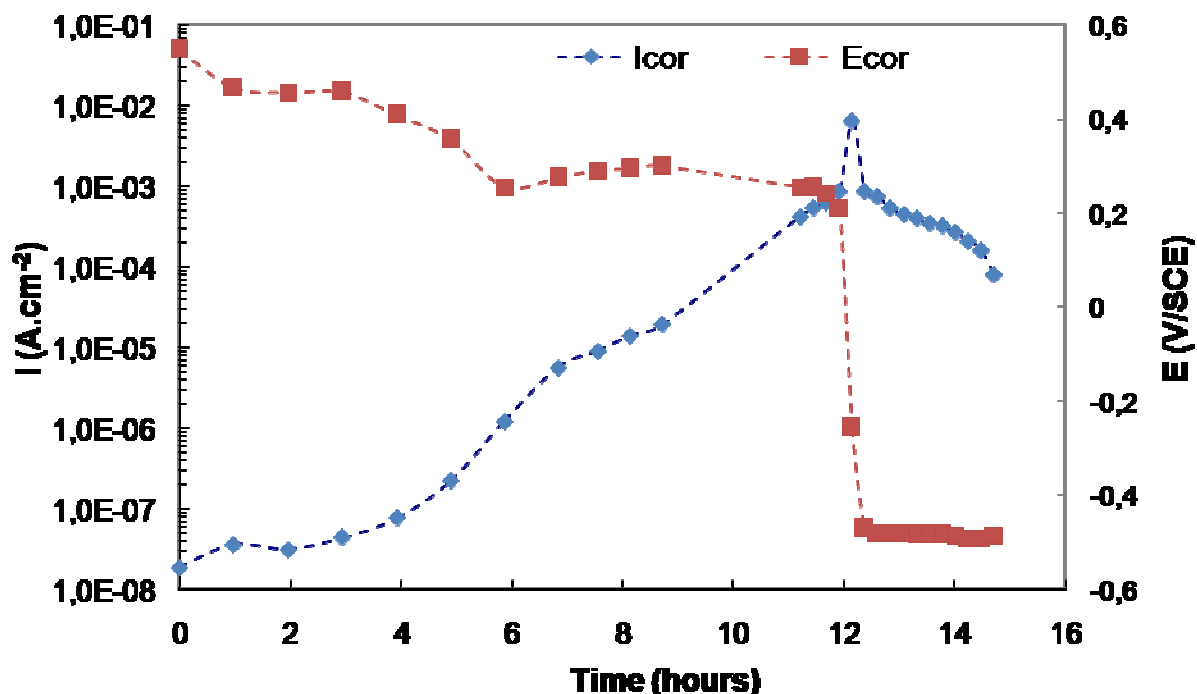


Figure IV. 4: Evolution of corrosion potential and corrosion current during scale dissolution in $\text{HCl } 1 \text{ mol.L}^{-1}$ at room temperature.

IV. 3. 3. Electrochemical Impedance Spectroscopy EIS

IV. 3. 3. 1. EIS diagrams

During the immersion period, the electrochemical impedance was measured at the open-circuit potential every 15 minutes. A representative impedance spectrum, obtained after 15 minutes of immersion, is presented in Figure IV. 5 in Nyquist format. The shape of the impedance diagram corresponds to a portion of a depressed semicircle. The lowest measured frequency was fixed to 0.2 Hz to enable measurement of the impedance diagram in period less than 2 minutes. This diagram was analyzed by use of an equivalent circuit composed of a resistor in parallel with a constant phase element CPE (inset of Figure IV. 5). The impedance of the CPE is given by $Z_{\text{CPE}} = (Q(j2\pi f)^\alpha)^{-1}$ where α and Q ($\text{F s}^{(\alpha-1)} \text{ cm}^{-2}$) are the CPE parameters.

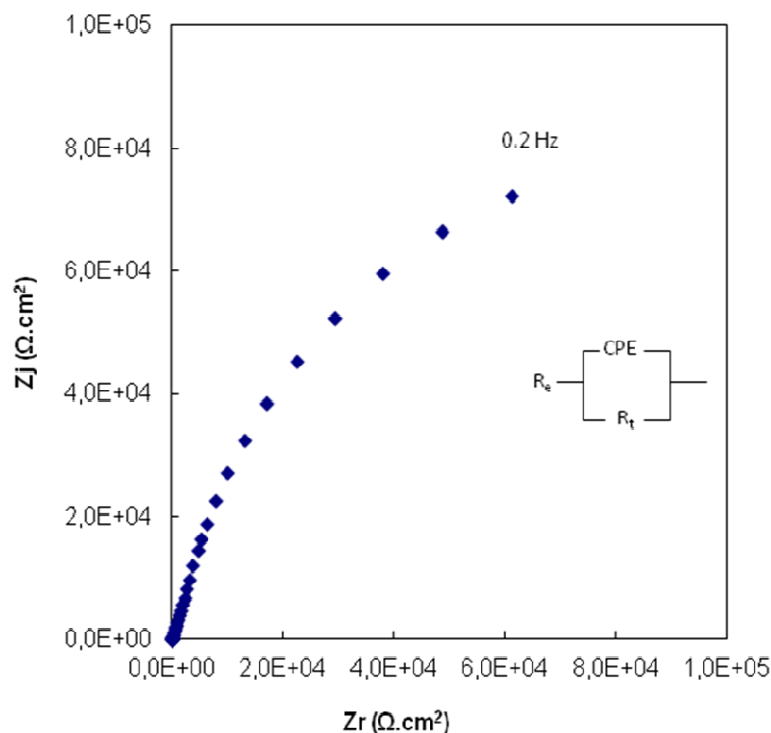


Figure IV. 5: Typical impedance diagram in Nyquist format measured after 15 minutes of immersion of the sample in 1M HCl at the corrosion potential (400 mV/SCE). The inset shows the equivalent-circuit used to analyze the spectrum.

IV. 3. 3. 2. Evolution of charge transfer resistance R

Similar to the variation of the corrosion current shown in Figure IV. 4, the polarization resistance varied by a few orders of magnitude within the immersion duration. For each immersion time, the CPE parameters (Q and α) and the polarization resistance (R) were obtained by a regression procedure using the software SIMAD developed in LISE. The inverse of the polarization resistance (R^{-1}) is presented as a function of the immersion time in Figure IV. 6. If the polarization resistance is assumed to be the charge transfer resistance (R_t), then the product of the corrosion current and charge transfer resistance should be proportional to the Tafel slope β , i.e., $R_t I_{\text{corr}} = \beta/2.303$.

The comparison between the temporal variation of I_{corr} (Figure IV. 4) and that of R^{-1} shows some differences, since the charge transfer resistance varies over more than three decades; whereas, the corrosion current density varies over more than four decades. This difference could be due to the fact that, according to the dissolution time, the reactions involved in the different processes are different and then the value of the Tafel slope β

corresponding to the product $R_t I_{\text{corr}}$ can vary with time. Nevertheless the variation of the two parameters shows the same tendency.

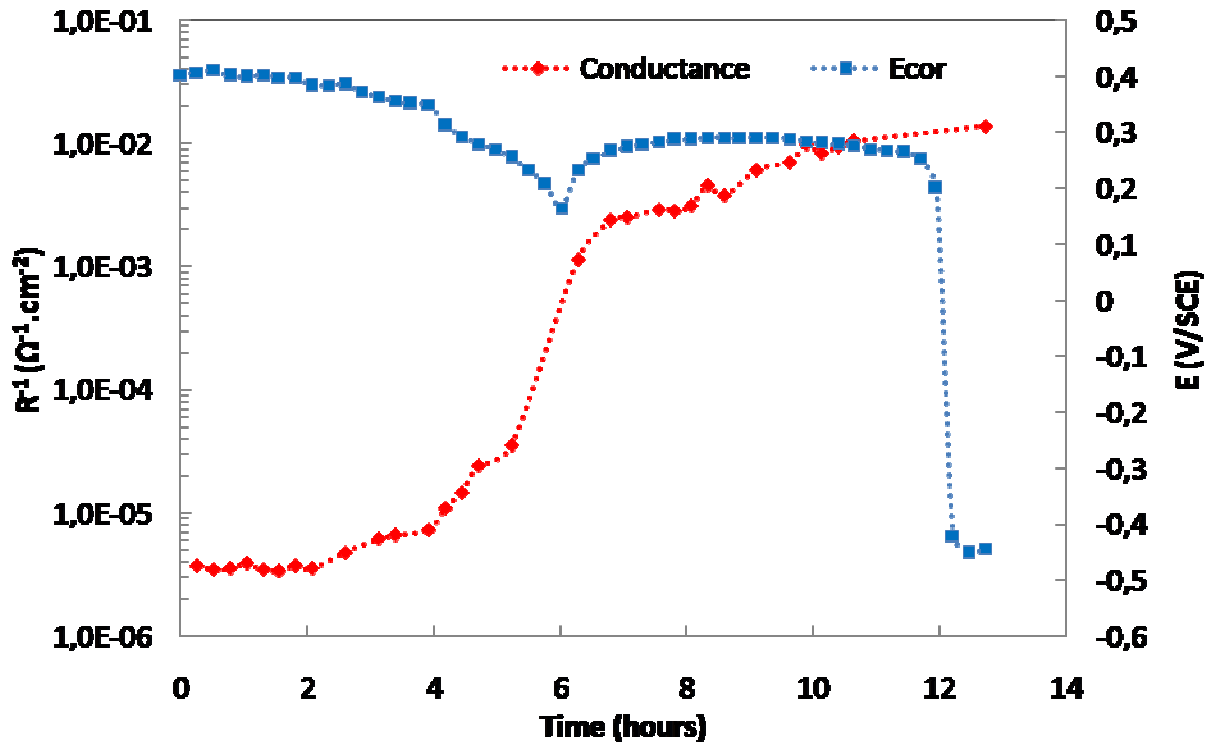


Figure IV. 6: Temporal evolution of inverse of the charge transfer resistance R^{-1} (conductance) and the corresponding corrosion potential during scale dissolution in 1M HCl acid solution at room temperature.

IV. 3. 3. 3. Evolution of CPE parameters

The variation of parameters Q and α are presented as a function of the immersion time in Figure IV. 7. The α values are in the range 0.8 to 0.9 within the duration of the experiment, indicating that the CPE can be attributed to a capacitance. Two domains are clearly observed for the Q values: during the first 6 hours, Q had a steady value of about $10^{-5} \text{ F} \cdot \text{s}^{\alpha-1} \cdot \text{cm}^{-2}$, a jump was observed, after which Q had a roughly constant value of $10^{-3} \text{ F} \cdot \text{s}^{\alpha-1} \cdot \text{cm}^{-2}$ until the end of the experiment. According to Figure IV. 4, the jump in Q occurs at the point in time where the hematite layer is dissolved and the magnetite layer becomes predominant on the sample surface. It is noticeable that no significant Q variation is observed before and after the potential jump at 12 hours.

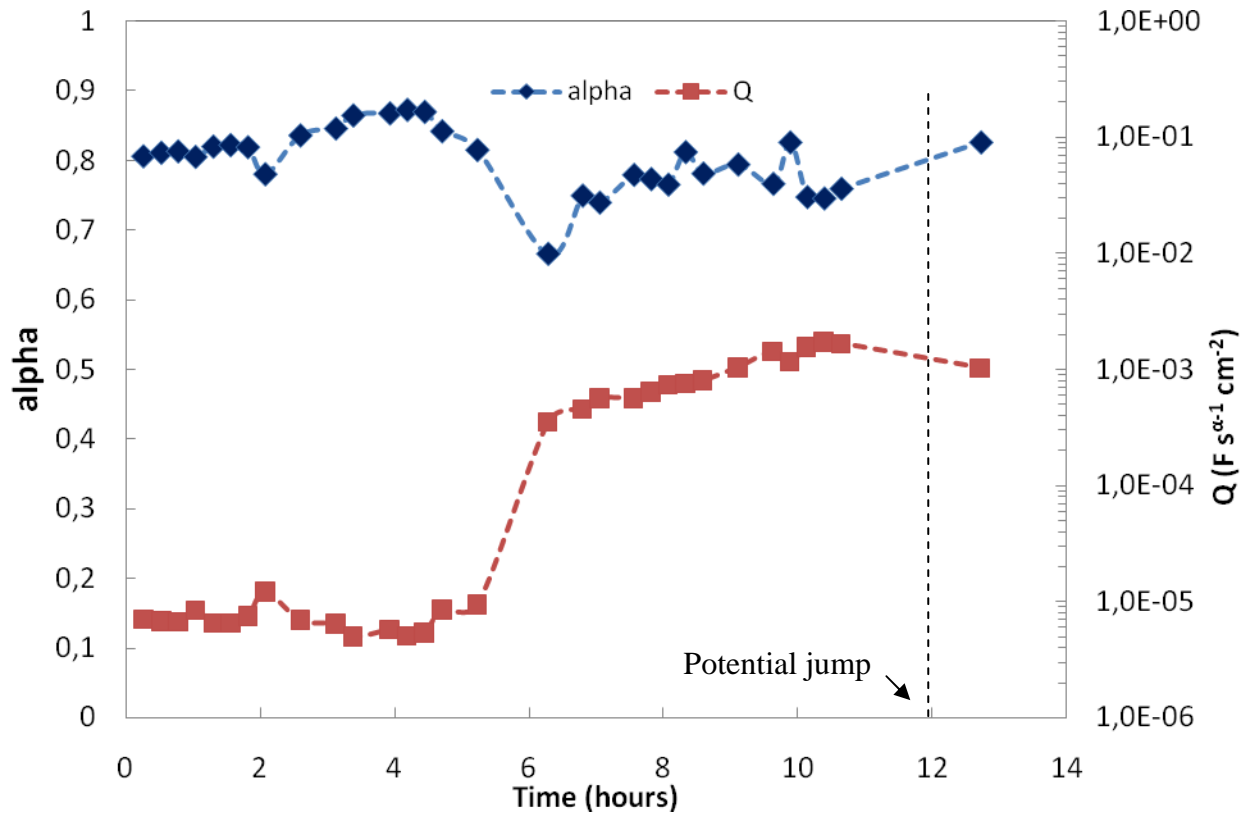


Figure IV. 7: Temporal evolution of regressed CPE parameters α and Q during scale dissolution in 1M HCl acid solution at room temperature.

IV. 3. 3. 4. Evolution of effective capacitance

According to the previous observations, the CPE measured by impedance must correspond to the capacitance of the hematite layer for $t < 6$ h, and to a double layer capacitance for larger immersion time. For each model the CPE analysis is different. In presence of the hematite layer, the time-constant distribution is through the hematite layer, and the power-law model described in chapter II can be applied. When the hematite layer is dissolved, an electrochemical dissolution of the magnetite and wüstite is assumed. In this case the CPE corresponds to a double layer capacitance and the time constant distribution is along the surface in agreement with the hypothesis of Brug's formula [113].

For an immersion time smaller than about 6 hours, the hematite layer is present (Figure IV. 4 and Figure IV. 6), and, according to the power law model (chapter II) the effective capacitance C can be estimated from the CPE parameters with equation:

$$C = (\epsilon\epsilon_0)^{1-\alpha} gQ\rho_\delta^{1-\alpha} \quad (\text{IV. 1})$$

The dielectric constant ϵ is known and has a value of 12 for hematite [123]. The function g is easily calculated with the experimental α value, and, following Orazem et al. [110], a value of 500 $\Omega\cdot\text{cm}$ can be assigned for ρ_δ .

Thus, from the experimental values of Q and α , values for the capacitance can be determined. The corresponding results are presented in Figure IV. 8. The capacitance increased from 10^{-7} $\text{F}\cdot\text{cm}^{-2}$ to 5×10^{-7} $\text{F}\cdot\text{cm}^{-2}$. Following equation (II. 24), these capacitance values correspond to a layer thickness which varies from 100 nm to 20 nm. The small values of film thickness can be used to explain why, in the SEM micrograph presented in Figure IV. 1, the hematite layer cannot be observed.

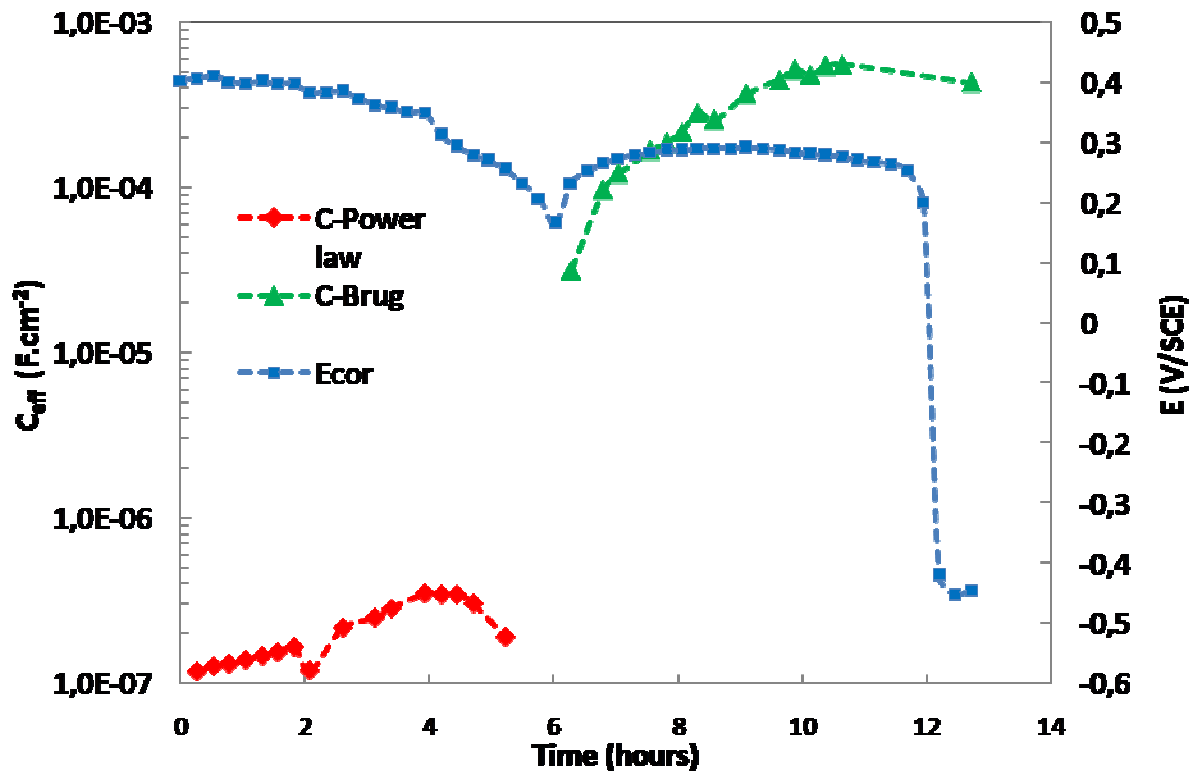


Figure IV. 8: Evolution of effective capacitance calculated with the power-law model [20] for a normal time-constant distribution and with Brug's model [22] for a surface time-constant distribution during dissolution of scale in 1M HCl at room temperature.

For immersion times higher than 6 hours, the hematite layer is no longer present, and the corresponding double layer capacitance was calculated by applying Brug's formula (chapter II).

The double layer capacitance varied from $6 \times 10^{-5} \text{ F.cm}^{-2}$ to $8 \times 10^{-4} \text{ F.cm}^{-2}$ (Figure IV. 8). These values are very large, but, if we assume that the solution penetrates inside the oxide layer, the active area can be significantly increased. So taking the usual value of $4 \times 10^{-5} \text{ F.cm}^{-2}$ for the double layer capacitance, the real active surface would be ascertained to have been 15 to 50 times larger than the geometrical area. This temporal evolution of the active area is in agreement with the increase of the corrosion current density value passing from $10 \mu\text{A.cm}^{-2}$ after 7 hours, to 1 mA.cm^{-2} after 12 h of immersion.

IV. 4. Total dissolution of scale

The dissolution rate of iron from the scale covered steel samples was measured by ICP-AES during the pickling process, and the overall variation with time is shown in Figure IV. 9. The evolution of the open-circuit potential (E(ICP)) was measured simultaneously. Its evolution is in agreement with the evolution observed during electrochemical measurements (E(EC)), which is also reported in Figure IV. 9. E(ICP) had a very anodic value (about 0.4V) at the beginning of the dissolution process, followed by an abrupt drop towards - 0.5 V after several hours. For easier comparison between electrochemical results and ICP measurements, a dimensionless time t_{dim} is reported on the abscissa of Figure IV. 9. It is defined as the ratio between the elapsed time and the time corresponding to the potential jump. Moreover, from the corrosion current densities reported in Figure IV. 4 the electrochemical dissolution rate calculated using Faraday's law (taking one electron as a first approximation) is also reported for comparison with the total rate of iron dissolution.

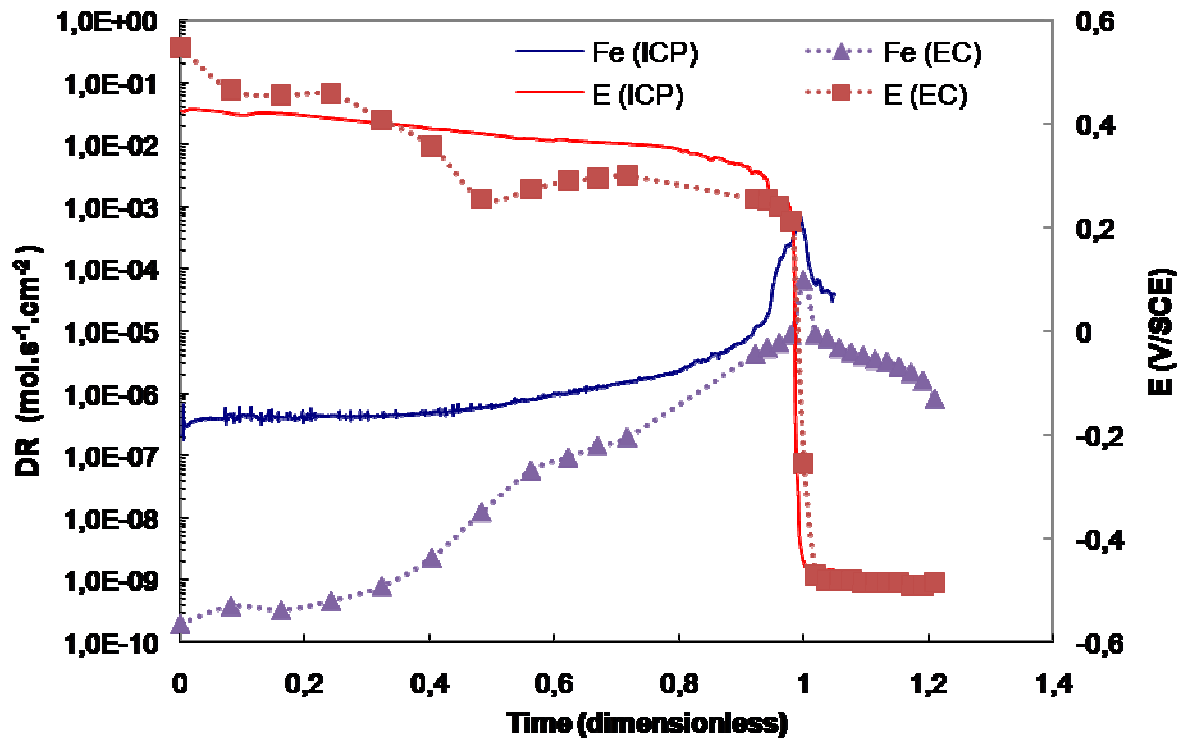


Figure IV. 9: Comparison between the total scale dissolution rate (DR) measured by ICP-AES and the electrochemical dissolution rate in 1 M HCl solution at room temperature.

At the beginning of pickling the total dissolution rate is very high compared to the electrochemical dissolution then the ratio between the two rates decreases while approaching the potential jump. The total dissolution rate decreases faster after the potential jump but remains above the electrochemical dissolution rate with few gap units.

IV. 5. Pickling and over-pickling mechanisms

IV. 5. 1. Pickling thermodynamics

Pickling and over-pickling of low carbon steels is assimilated to the dissolution of iron oxides and iron in an acid medium. The thermodynamics of this dissolution is studied with an E-pH or Pourbaix diagram where the different phases of the system are located according to their stability in potential and pH zones. The boundaries between the stability zones are plotted with Pourbaix's data on iron system in water [124] and presented in Figure IV. 10.

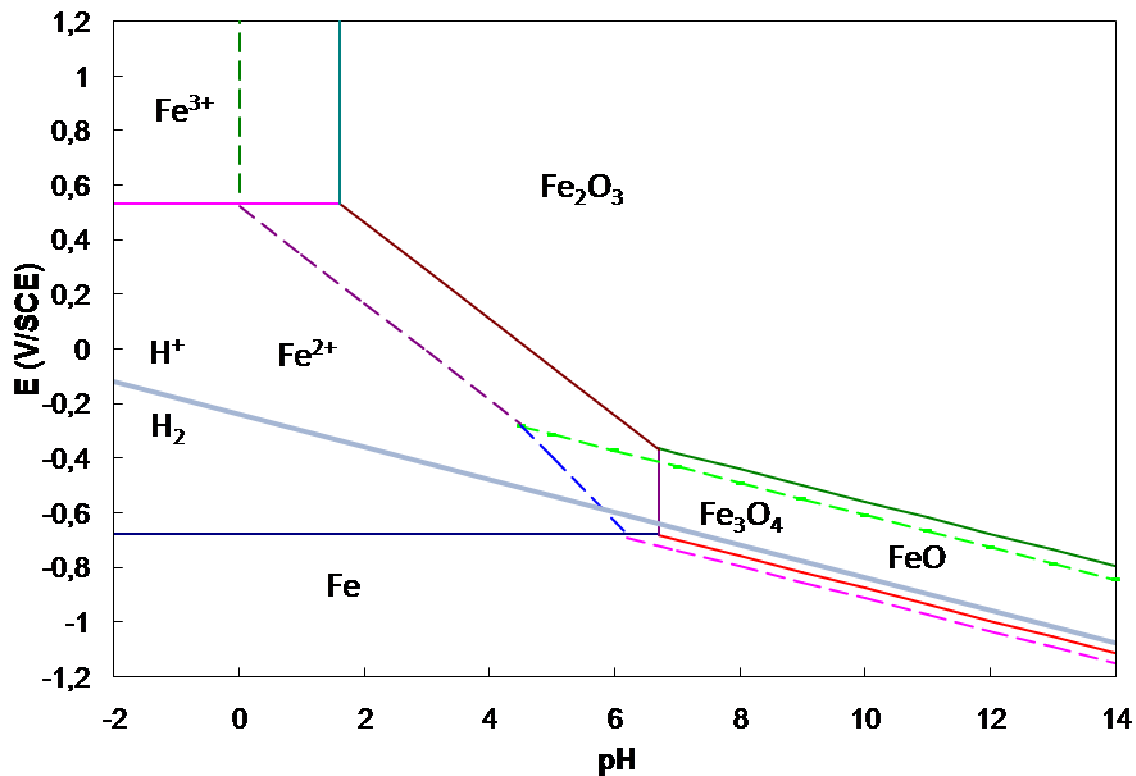


Figure IV. 10: E-pH diagram of iron system and protons in water according to Pourbaix's data [124].

The potential in E-pH diagram of Figure IV. 10 are expressed versus the SCE to simplify their comparison with the corrosion potential values during pickling and over-pickling. In general, the corrosion potential in pickling conditions (0.4 to -0.5 V/SCE) is in the stability zone of Fe^{2+} , this means only that this cation is the most thermodynamically stable specie in the pickling bath.

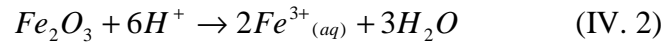
IV. 5. 2. Pickling steps and reactions

During the early stages of immersion, the OCP was about 0.4 V/SCE and the corrosion current density was very low, i.e., $5 \cdot 10^{-2} \mu\text{A} \cdot \text{cm}^{-2}$. The Raman spectra suggest that the oxide layer at this stage was coated by a very thin layer of hematite. In agreement with the positive value of the OCP and the low value of the corrosion current, the hematite behaves like a passivating layer, with field-assisted transfer of ions within the semiconducting non-stoichiometric layer [101].

The existence of some cracks in the hematite leading to a contact between the solution ($\text{HCl } 1 \text{ mol} \cdot \text{L}^{-1}$) and Fe_3O_4 and/or FeO cannot be excluded, but, since Fe_2O_3 and Fe_3O_4 layers

have very close OCP potential values in acid solutions [101], the contribution of each component cannot be determined. It clearly appears from Figure IV. 9 that at this stage of pickling the hematite layer mainly dissolves by a chemical process, with an electrochemical contribution of 0.1%, in close agreement with the results of Virtanen et al. [101].

During the first hours, $t_{\text{dim}} < 1$, the corrosion current density stayed at a very low level; whereas, the open-circuit potential and the overall leaching rate were roughly constant. This period of time could be characteristic of the vanishing of the hematite layer due to chemical dissolution according to

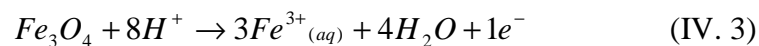


After this period, the increase in the electrochemical dissolution (v_{elec}) rate became much more significant than that of total dissolution rate (v_{total}), the ratio between $v_{\text{elec}}/v_{\text{total}}$ passing from 1/1000 to 1/4 after a pickling time close to $t_{\text{dim}} = 1$. Before $t_{\text{dim}} = 1$, the corrosion potential progressively decreases from 0.5 to 0.3 V, simultaneously with the increase of the electrochemical dissolution of the remaining phases beneath hematite, mainly magnetite and wüstite. The overall leaching rate varied from 3×10^{-10} to 3×10^{-9} mol Fe s^{-1} cm^{-2} for t_{dim} varying from 0 to 1, which is two orders of magnitude higher than the value reported by Virtanen et al. [101] for pure hematite and pure magnetite, showing that the reactivity of the present scale is different from that of pure oxides.

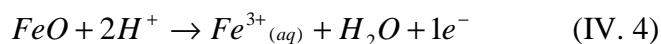
Potential jump at $t_{\text{dim}} = 1$

At $t_{\text{dim}} = 1$, the huge potential jump from 0.3 V/SCE to - 0.45 V/SCE indicates that the electrochemical reactions involved before the jump no longer fix the corrosion potential value after the jump. It is then necessary to propose two sets of electrochemical equations, one set for the anodic domain before the jump and one set after.

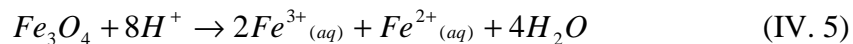
Before the jump, after dissolution of hematite, the layer under consideration is mainly composed of magnetite and wüstite. As mentioned previously, wüstite is unstable at room temperature and is partly decomposed into iron and magnetite. At this anodic potential (0.3 V/SCE), the anodic dissolution of iron is very fast but the quantity of iron is small. The electrochemical reactivity of the layer must therefore be attributed to the electrochemical oxidation of magnetite according to



or to oxidation of wüstite according to

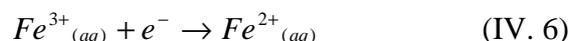


It has been suggested in the literature [101] on a pure sputtered magnetite layer that dissolution of magnetite is mainly chemical and that oxidative dissolution is not likely to occur. The main reaction leading to chemical dissolution of magnetite would then be



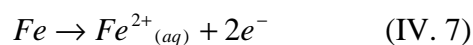
In the present work, the composition of the scale beneath the hematite is a poorly-defined mixture of magnetite, wustite, and iron. It can also be expected that this layer is heterogeneous and defective and that the composition of the scale/solution interface is modified throughout the dissolution. Figure IV. 9 shows clearly that chemical dissolution is significantly favored as compared to the electrochemical process, but this latter step cannot be neglected and becomes significant after a few hours of pickling. This observation is supported by the interfacial capacitance value shown in Figure IV. 8, which is in agreement with that of a double layer capacitance.

For the cathodic reaction, the potential is too anodic to consider the proton reduction, but, due to the parallel chemical dissolution of the oxides layer, the solution contains Fe^{3+} ions which can be reduced to Fe^{2+} .



IV. 5. 3. Over-pickling reactions

When the potential drop reaches the value of - 0.45 V/SCE, which is also the E_{corr} value for bare iron in the acidic medium; the solution has reached the metal. The anodic reaction is then expected to be mainly iron dissolution

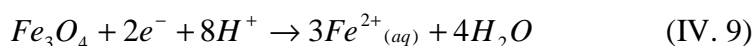


and the cathodic reaction is expected to be primarily proton reduction, i.e.,



Nevertheless visual observation of the surface of the sample shows that many spots of oxide are still present on the electrode even few hours after the potential jump, and Figure IV. 9 confirms that chemical dissolution still contributes to the total dissolution.

Additional cathodic reactions should therefore be considered. According to references [100, 102], reductive dissolution of magnetite is also expected in this potential range:



As before the potential drop the main cathodic reaction was assumed to be the reduction of Fe^{3+} ions coming from the chemical dissolution, the rate of this reaction should be highly enhanced at this cathodic potential. But since the contribution of the chemical process to the overall mechanism is significantly decreased, the concentration of Fe^{3+} near the surface is expected to be lowered too. The drastic decrease of the rate of chemical dissolution can be attributed to the fact that the rate of proton reduction is faster than the rate of chemical dissolution or to the fact that the production of hydrogen blocks the chemical dissolution of the oxide. The dissolution of iron is exclusively electrochemical and produces stable Fe^{2+} in this potential range.

The mechanism proposed above is in disagreement with the mechanisms proposed in the literature where the electrochemical dissolution corresponds to the reduction of iron oxides by iron in micro-electrochemical cells iron/acid/iron oxides in parallel with the chemical dissolution of wüstite [88, 89, 91].

These mechanisms are based on the galvanic coupling of iron and its oxides, which is probably a minor contribution and is not coherent with the high anodic corrosion potential values during pickling. During over-pickling, the reduction of protons is the dominant reaction versus the reduction of magnetite.

IV. 6. Influence of some parameters on pickling and O-P mechanism of LCS scales

The pickling and over-pickling mechanism described above concerns a model scale with the three iron oxide layers in soft pickling conditions. These conditions allow the monitoring of different pickling steps and give a sufficient time for their characterization.

To correlate the proposed mechanism with industrial conditions, a non exhaustive list of oxidation and pickling parameters closer to industrial conditions is studied to evaluate their effect on pickling mechanism and kinetics. The corrosion potential evolution of low carbon steel scale in some different pickling conditions is presented in Figure IV. 11.

As the potential drop corresponds to the contact between the acid and the metal and to the start of over-pickling, the time needed to reach it will be considered as the “pickling time” at a first approximation and used to compare the effect of oxidation and pickling conditions on pickling time (see §IV.6.1.).

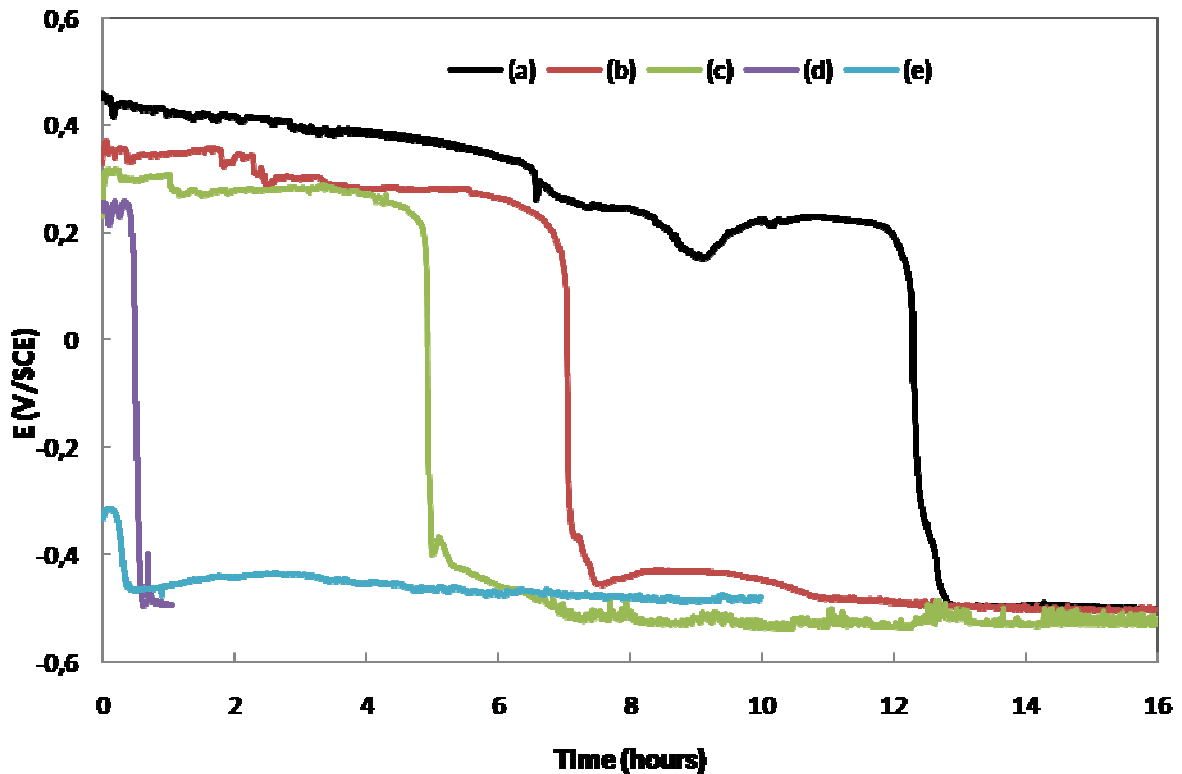


Figure IV. 11: Temporal evolution of corrosion potential during dissolution of low carbon steel scales in different conditions: (a) Si00-model scale with hematite outer layer in HCl 1 mol.L⁻¹ at room temperature, (b) Si00-model scale without hematite outer layer in HCl 1 mol.L⁻¹ at room temperature, (c) Si00-model scale without hematite outer layer in HCl 3 mol.L⁻¹ at room temperature, (d) Si00-model scale with hematite outer layer in HCl 1 mol.L⁻¹ at 50°C, (e) thin and cracked scale (similar to industrial black coil scale) in HCl 1 mol.L⁻¹ at room temperature .

IV. 6. 1. Scale composition and morphology

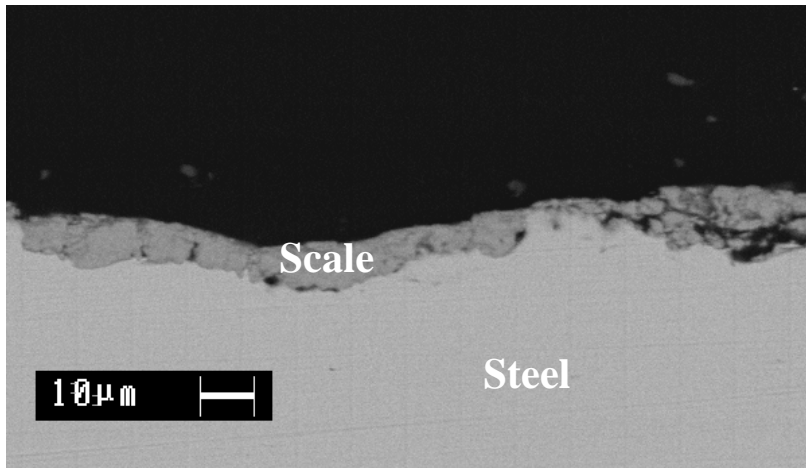
IV. 6. 1. 1. Influence of hematite on pickling

The pickling times were compared at room temperature in HCl 1 mol.L⁻¹ between a Si00-model scale with hematite and Si00-model scale without hematite. The presence of a hematite outer layer delays scale dissolution due to its passive-like behavior. The electrolyte must diffuse through micro-cracks of this layer to reach magnetite and wüstite. Pickling time without hematite is lowered up to 60% of the model scale pickling time (Figure IV. 11a and b).

IV. 6. 1. 2. Pickling of an industrial scale

Industrial scale is thin and, cracked (Figure IV. 12a). Pickling time of this kind of scale cannot be approximated by the corrosion potential drop since this occurs immediately after immersion in acid (Figure IV. 11e). ICP-AES is more adequate to monitor pickling of this kind of sample (Figure IV. 12b).

(a)



(b)

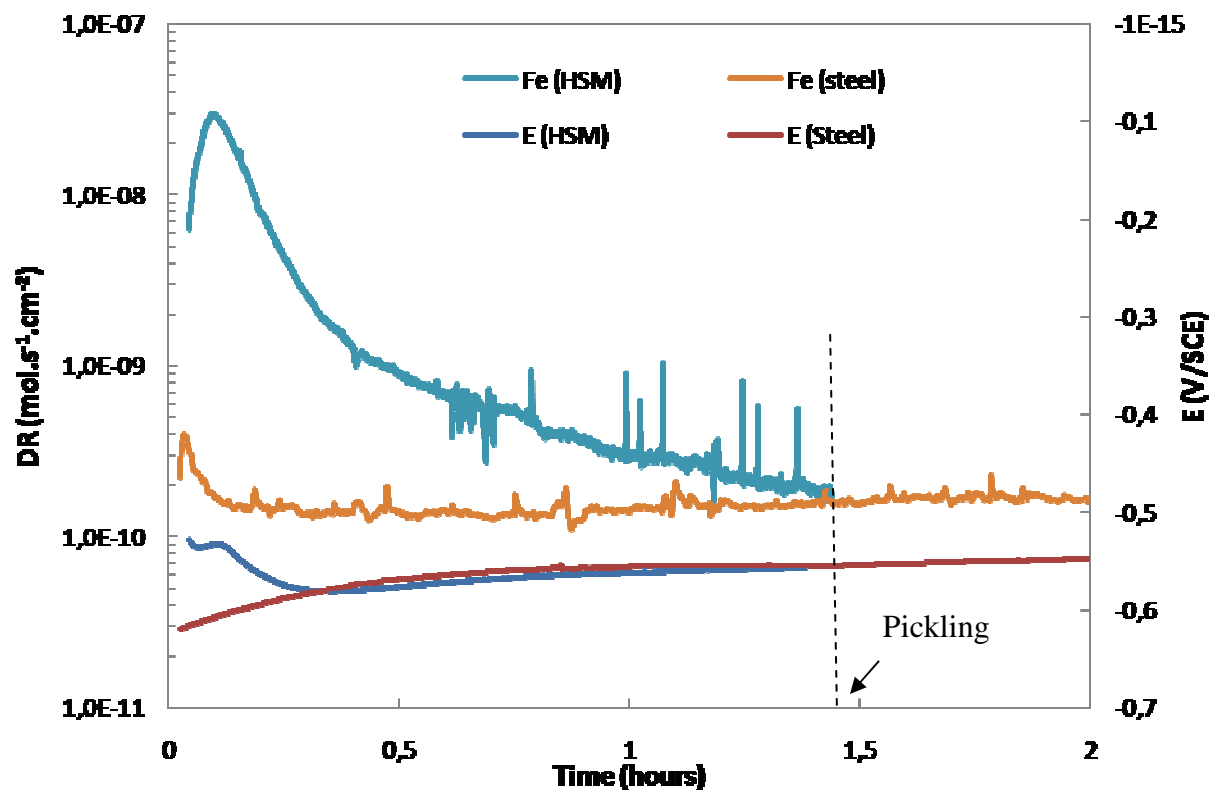


Figure IV. 12: (a) Cross section micro-graph of the low carbon steel oxidized in the hot strip mill (HSM). (b) Temporal evolution of iron dissolution rate and corrosion potential of a low

carbon steel scale from the hot strip mill (HSM) and a polished steel during dissolution in HCl 1 mol.L⁻¹ at room temperature.

For a **hot strip mill (industrial) scale**, the corrosion potential is negative immediately after immersion in the acid. This means that over-pickling starts also immediately. Indeed, pickling of black coils can be assimilated to an **over-pickling** with the electrochemical mechanism implying the oxidation of steel and the simultaneous reduction of magnetite and protons.

The pickling time for this kind of sample can be approximated by the intersection between the dissolution rate of iron from scale and iron from the bare steel (1.4 hour in Figure IV. 12)

IV. 6. 2. Influence of acid concentration

The pickling times of two Si00-model scales without hematite were compared at room temperature in HCl at two concentrations: 1 mol.L⁻¹ and 3 mol.L⁻¹. The pickling time decreased when acid concentration increased by a factor of about 30 % (Figure IV. 11 b and c). This confirms the accelerating effect of a lower pH of the solution.

IV. 6. 3. Influence of pickling bath temperature

The effect of temperature increase up to 50°C was significant on pickling time. Even with the presence of the hematite passive layer, the pickling time was reduced by almost 95 % (Figure IV. 11 a and d). This is due to the higher infiltration of the electrolyte (higher diffusion coefficient) and the reduction of the activation energy for all chemical and electrochemical reactions when temperature increases.

IV. 6. 4. Influence of a cathodic applied potential

A cathodic potential was applied on the model scale and its effect on pickling mechanism was evaluated by simultaneous monitoring of the total dissolution rate of iron by ICP-AES and the cathodic current density. (Figure IV. 13).

The applied cathodic potential was about 250 mV more negative than E_{corr} of iron (E_{ap} = - 700 mV/SCE), in order to neglect the anodic reactions.

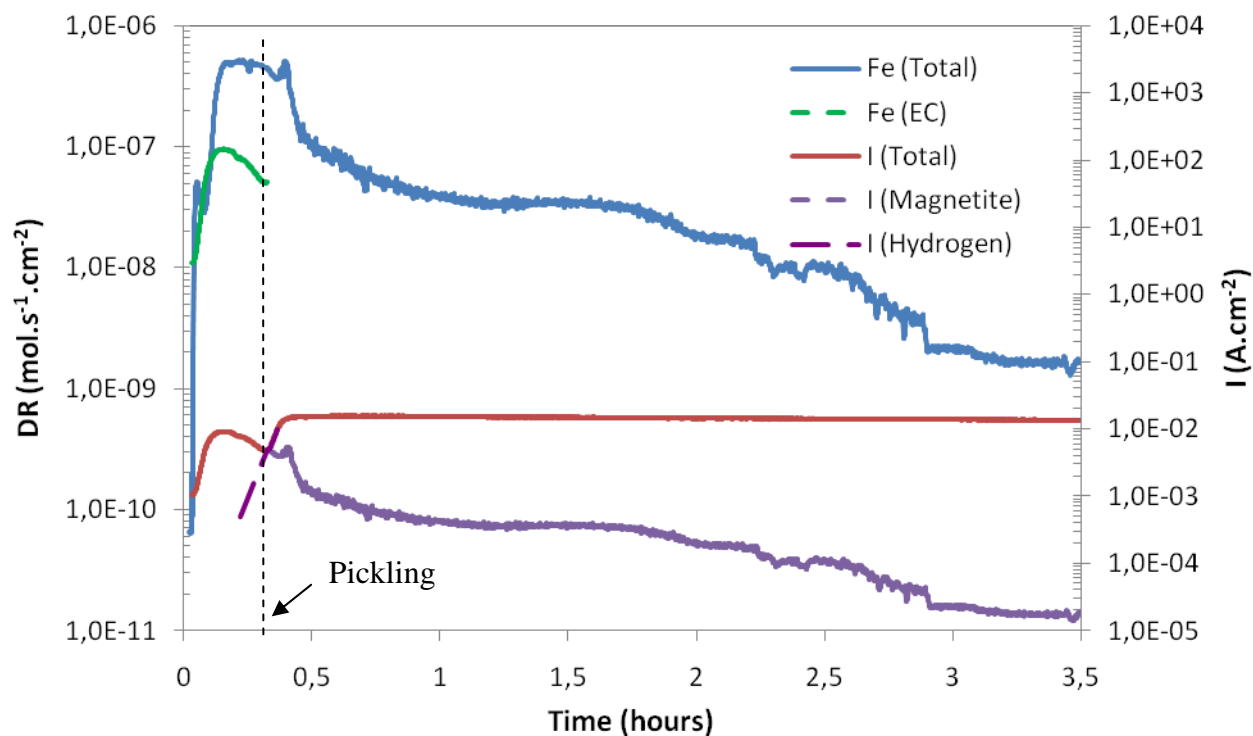


Figure IV. 13: Temporal evolution of total dissolution rate of iron and cathodic current density at an applied potential of - 700 mV/SCE in $\text{HCl } 1 \text{ mol.L}^{-1}$ at room temperature. Fe (EC) and I (Hydrogen) curves are deduced from I (Total) curve while I (Magnetite) curve is deduced from Fe (Total) curve.

The total amount of iron measured by ICP-AES (Fe (Total) in Figure IV. 13) at this cathodic potential comes from the electrochemical reduction of hematite and magnetite phases and from wüstite and iron particles which are mechanically detached and dissolved in the solution. The cathodic current I (Total) comes from the reduction of iron oxides and the protons depending on the phase in contact with the acid.

During the first 20 minutes of polarization, the cathodic current first increased up to a peak at 8 mA.cm^{-2} after nearly 10 minutes then decreased down to a local minimum at 3 mA.cm^{-2} . At the same time, the total dissolution rate of iron first followed the same tendency by increasing up to $5 \times 10^{-7} \text{ mol s}^{-1} \text{ cm}^{-2}$ then decreased slightly. These similar tendencies of the two curves in this period confirm the contribution of the reduction of iron oxides in scale dissolution at cathodic potential.

After 20 minutes of immersion, the cathodic current increased again up to $1.5 \times 10^{-2} \text{ A.cm}^{-2}$ and kept this value after 25 minutes of immersion. At the same time, the total dissolution rate of iron increased again slightly up to $5 \times 10^{-7} \text{ mol s}^{-1} \text{ cm}^{-2}$ after 25 minutes. Unlike the stable cathodic current after 25 minutes of immersion, the total dissolution rate

decreased slowly until the end of the experiment. These different tendencies imply the protons reduction as a dominant cathodic reaction once the acid reached the metal after 20 minutes of immersion.

The current density peak during the first 20 minutes was attributed to the reduction of iron oxides (mainly magnetite). The reduction of protons was neglected in this period and estimated by I (Hydrogen) curve in Figure IV. 13. The current density can then be converted into moles of dissolved iron from magnetite reduction using Faraday's law (approximation of 1.5 Fe for 1e⁻). The dissolution rate of iron attributed to magnetite reduction increased up to about 10⁻⁷ mol.s⁻¹.cm⁻² after 10 minutes of immersion then decreased down to 5 10⁻⁷ mol.s⁻¹.cm⁻² after 20 minutes of immersion. Based on these values, the contribution of the magnetite reduction in the total dissolution rate of scale varied from 1/5 to 1/9 after 10 and 20 minutes of immersion respectively. At the applied cathodic potential - 700 mV/SCE, the chemical reactions were supposed to be blocked and dominated by the reduction of magnetite. In this case the non electrochemical contribution in scale dissolution can only be attributed to the mechanical detachment of wüstite and iron particles of the decomposed wüstite or even some magnetite particles which did not had the time to dissolve.

After 20 minutes, the current density second increase and stabilization at 1.5 x 10⁻² A.cm⁻² corresponds to the over-pickling period where the acid is in contact with the steel. Neglected on the oxides surface, the H⁺ reduction becomes dominant on steel surface which explains the stable cathodic current during this period. The slow decrease of the total dissolution rate after the acid reaches the metal was attributed to the continuous dissolution of the decomposed wüstite by reduction of its magnetite particles. To estimate the cathodic current due to magnetite, the EC/total dissolution ratio (1/9) at the pickling to over-pickling transition at 20 minutes was taken as constant. By application of this ratio and Faraday's law on the total dissolution rate, the cathodic current due to magnetite was calculated (I (Magnetite) in Figure IV. 13). It represented the continuity of the cathodic current before the starting of over-pickling and confirmed the decreasing contribution of magnetite reduction in the total cathodic current (nearly 1/1000 after 3 hours of immersion). The domination of the electrochemical reactions especially the protons reduction during over-pickling will be confirmed in chapter 5.

In these pickling conditions, the pickling time can be approximated by the local minimum of the cathodic current after the first peak due to the reduction of iron oxides. It corresponds to 4% of the pickling time of the model scale in soft pickling conditions. The

cathodic potential is, so far, the most efficient pickling accelerator and at the same time a method to protect steel from over-pickling.

IV. 7. Steel surface after pickling and over-pickling

Steel surface was observed by SEM-EDS to identify its chemical composition after pickling and over-pickling. The optical interferometry was used to evaluate the effect of a long over-pickling on steel surface roughness.

IV. 7. 1. Steel surface after insufficient pickling

Steel surface of a pickled sample was observed after the potential drop to identify its chemical composition (Figure IV. 14).

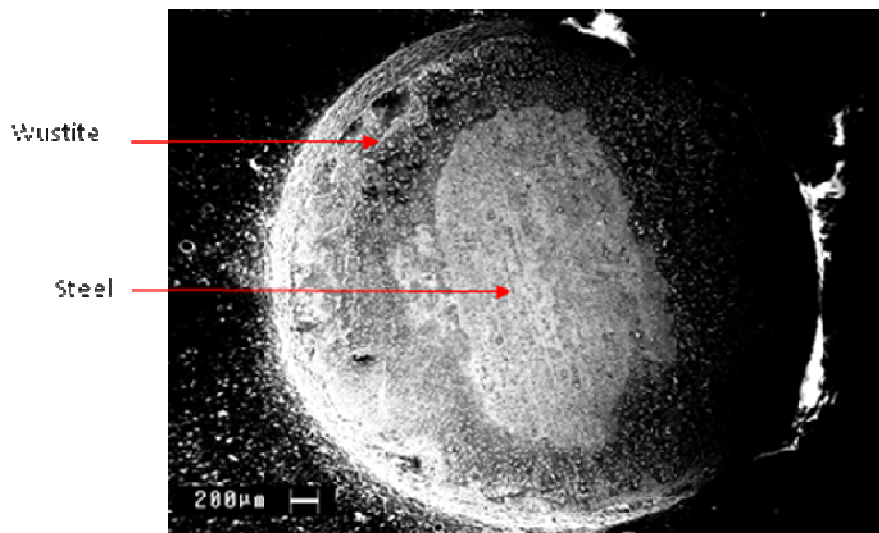


Figure IV. 14: SEM micrograph of a low carbon steel surface after pickling in HCl 1M at room temperature and at corrosion potential $E_{\text{corr}} = - 0.45 \text{ V/SCE}$.

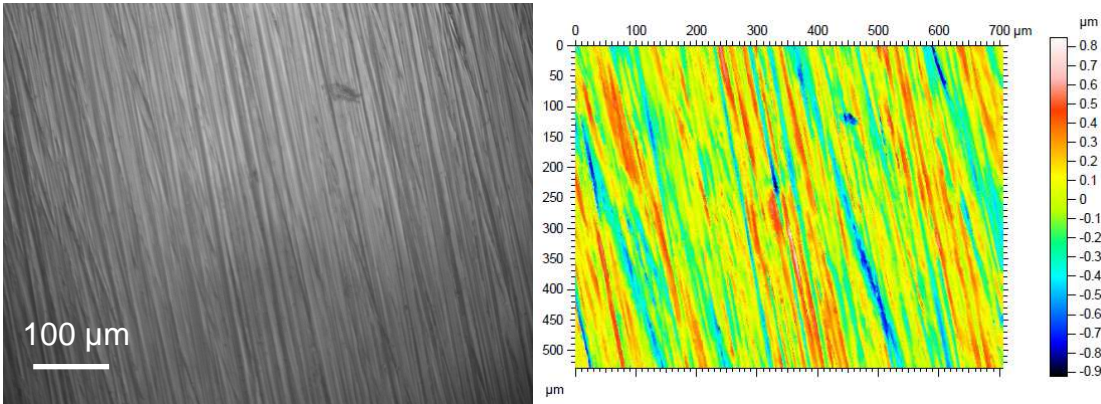
Even though the corrosion potential is negative, steel surface is not completely pickled since wüstite covers part of this surface. The corrosion potential drop gives an approximation of pickling time but does not indicate the end of pickling.

IV. 7. 2 Steel surface after long over-pickling:

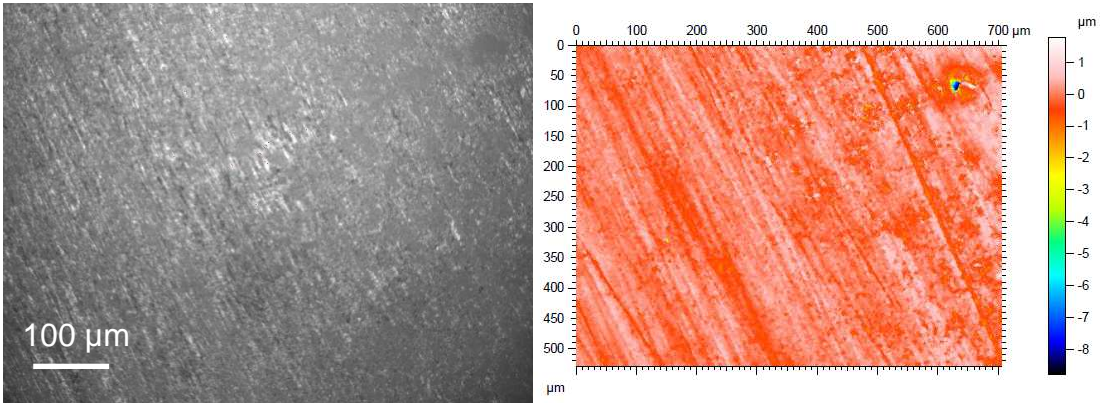
The roughness change of polished Si00 steel was observed with optical interferometry (chapter II). The roughness is estimated by the depth of holes (negative) and heights of summits (positive) relative to a medium plan of steel surface. They are expressed in μm and their intervals presented with colour codes cartographies. Examples of steel surface optical

micrographs at 2 different times of immersion in an acid bath at room temperature and pickling lines temperature (70°C) are presented in Figure IV. 15.

(a)



(b)



(c)

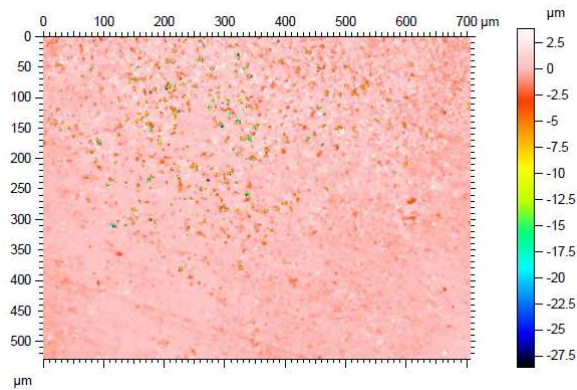


Figure IV. 15: Optical micrographs (0.7 x 0.55 mm) and 3D roughness cartographies of a polished Si00 steel surface (grit 800) after dissolution in HCl 1 mol.L⁻¹: (a) before immersion (b) after 10 minutes of immersion at room temperature and (c) after 10 minutes of immersion in a bath at 70°C (optical micrograph not available).

In addition to the surface cartography, two parameters were chosen to characterize the surface roughness: Sz and Sq representing the total height and average quadratic height respectively. They are expressed in μm and their evolution with over-pickling time and bath temperature is presented in Figure IV. 16.

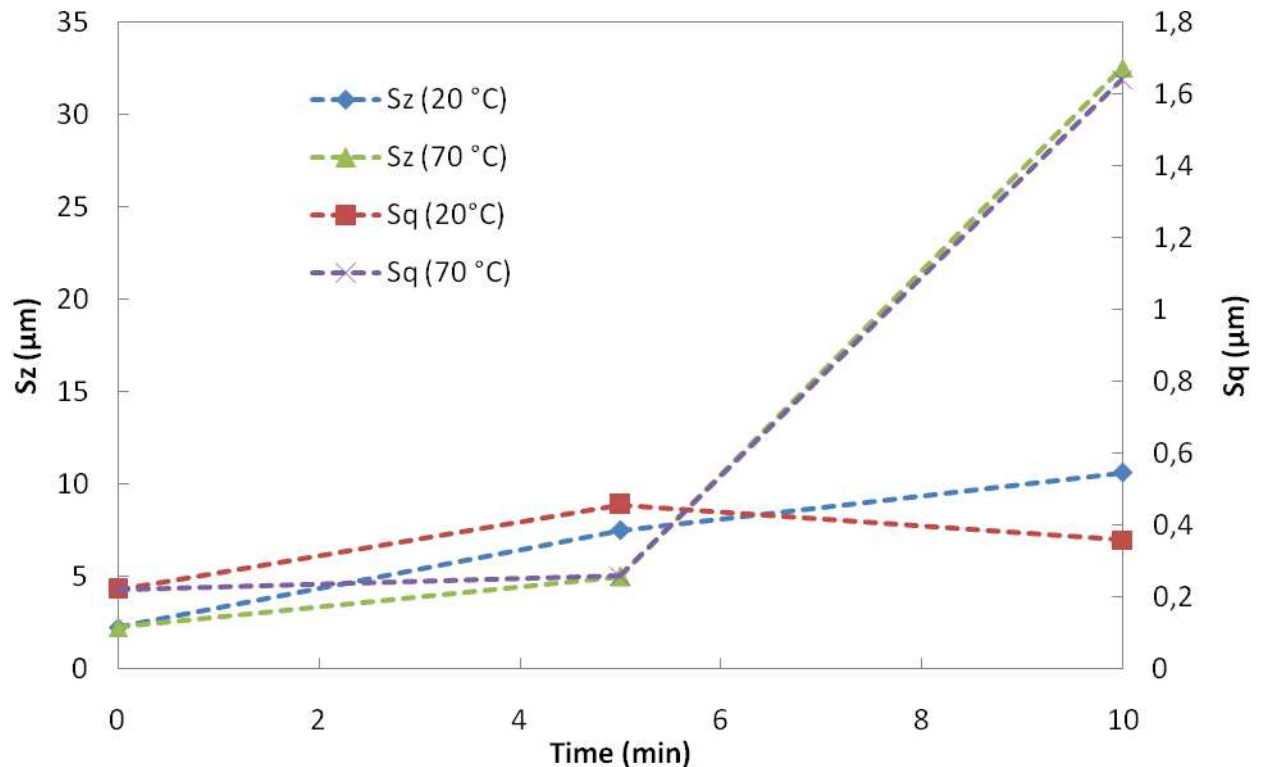


Figure IV. 16: Evolution of roughness parameters Sz and Sq after 5 and 10 minutes of dissolution Si00 polished (grit 800) in $\text{HCl } 1 \text{ mol.L}^{-1}$.

On Si00 surface before dissolution, the polishing traces are visible (grit 800). The roughness of this surface was taken as a reference (Figure IV. 15a).

The surface observations and evolution of roughness parameters of Si00 steel surface showed that the roughness increases significantly with over-pickling time and temperature. This can be due to absence of anti-corrosion alloying elements and high corrosion rate at grain boundaries.

IV. 8. Conclusions

In-situ ICP analyses of pickling solutions were performed simultaneously with electrochemical measurements on scales synthetically obtained on low carbon steels in order to determine the nature of the dissolution reactions.

It appears that dissolution of hematite is mainly of chemical nature, whereas the dissolution of magnetite and wüstite is both chemical and electrochemical.

A very positive open-circuit potential was measured in the presence of hematite and magnetite, but once the metallic substrate was reached by the pickling solution, a huge potential jump of more than 700 mV towards the cathodic region was observed. Such a jump is only possible if the nature of the determining electrochemical reactions is drastically modified.

Before the potential jump, at 0.4V, the main anodic reaction was the oxidation of magnetite and wüstite and the main cathodic reaction was the reduction of ferric ions formed by chemical dissolution. After the potential jump, at - 0.45V, the proton reduction is assumed to be the main cathodic reaction, whereas the oxidation of the iron substrate is the main anodic reaction. The reduction of ferric into ferrous ions must then become negligible, since the rate of chemical dissolution of iron oxide is significantly lowered in comparison with the electrochemical dissolution.

A noticeable result in this work was to show the key role played by ferric ions formed in the pickling bath by chemical dissolution of hematite and magnetite. They provide the cathodic reaction enabling anodic dissolution of the scale, in a potential range in which protons are not reduced.

For the scale model, the potential drop occurs simultaneously with the dissolution peak corresponding to a high dissolution rate of iron from the substrate at the transition time. While industrial scales are thinner and cracked, the negative corrosion potential and the dissolution peak are observed immediately at the beginning of pickling, this means that over-pickling starts simultaneously with pickling and the major part of scale is removed with over-pickling.

Pickling is accelerated by many parameters. They are ranked by their lower pickling times as follows: pH decrease, temperature increase, cathodic potential and scale cracking. The cathodic potential application is the most efficient parameter to accelerate pickling and protect the metal from corrosion at the same time.

V. Pickling and over-pickling mechanisms of high silicon alloyed steel grades

Summary

V. 1. Introduction	111
V. 2. Model scale characteristics before pickling	111
V. 3. Electrochemistry of scale dissolution	113
V. 3. 1. Corrosion potential E_{corr}	113
V. 3. 2. Corrosion current density I_{corr}	115
V. 3. 2. 1. Current-potential curves	115
V. 3. 2. 1. Evolution of the corrosion current density	117
V. 4. Total dissolution of scale	120
V. 4. 1. Total dissolution rate (TDR)	121
V. 4. 2. Electrochemical contribution in scale dissolution.....	122
V. 5. Pickling and over-pickling (O-P) mechanism	122
V. 5. 1. Pickling steps and reactions	123
V. 5. 2. Over-pickling steps and reactions	123
V. 6. Influence of some parameters on pickling and O-P mechanism	125
V. 6. 1. Scale morphology and composition	126
V. 6. 1. 1. Influence of fayalite morphology	126
V. 6. 1. 2. Behaviour of industrial scale	126
V. 6. 2. Influence of pickling bath temperature	127
V. 6. 3. Influence of acid concentration	128
V. 7. Steel surface after pickling and over-pickling	129
V. 7. 1. Steel surface after insufficient pickling.....	129
V. 7. 2. Steel surface after over-pickling.....	130
V. 8. Conclusions	133

V. 1. Introduction

After oxidation in the hot strip mill, silicon oxides (silica and fayalite) concentrate at the steel/scale interface in many forms; silica thin layer, fayalite grains in wüstite, fayalite layer and infiltrations and silica internal oxidation grains in steel substrate (chapter III).

The upper iron oxide layer dissolves easily in classical pickling baths but the low solubility of silicon oxides present at the steel/scale interface increases the pickling time. In the case of fayalite infiltrations and high internal oxidation, a long over-pickling step is necessary to suppress fayalite and oxides at the grain boundaries. In HCl media, the addition of nitric acid induces a more reactive bath towards the metallic surface. The addition of HF acid increases the pickling efficiency without increasing the metal dissolution, due to its efficiency to dissolve silicon oxides [80, 89, 103-105].

No pickling mechanism of silicon steels was found in the literature. Only empirical studies were done on industrial scales of silicon steels to evaluate the pickling time and to explore different conditions to remove the fayalite phase.

In this study, two model scales of high silicon alloyed steels with two different fayalite morphologies were chosen to model pickling mechanism of silicon alloyed steels in soft conditions.

As for the low carbon steel scale, a comparison of the dissolution mechanism of model scales with industrial scales in pickling line conditions will be presented.

V. 2. Model scale characteristics before pickling

As seen in chapter III, scale morphologies of silicon steels depend on oxidation temperature. Two scales with different morphologies formed at two different temperatures were chosen as model scales for a 1.6 wt% Si steel (Si16).

Scale formed at 1100°C is composed of three parallel layers: a magnetite layer, a decomposed wüstite layer and an internal layer composed of fayalite grains in a wüstite matrix (Figure V. 1). The total thickness of this scale is about 280 µm.

The hematite outer layer is absent in this scale and the magnetite and wüstite layers are thicker after 15 min of oxidation, their thickness was estimated to around 25 and 200 µm respectively versus 7 and 70 µm, in comparison with Si00-model scale sample (section IV. 2). The newly formed fayalite-wüstite layer has a thickness of about 55 µm. The higher thickness

of iron oxides was attributed to the higher oxidation temperature (1100 °C versus 850 °C during 15 minutes).

The sample will be called **Si16-fayalite grains** in this chapter.

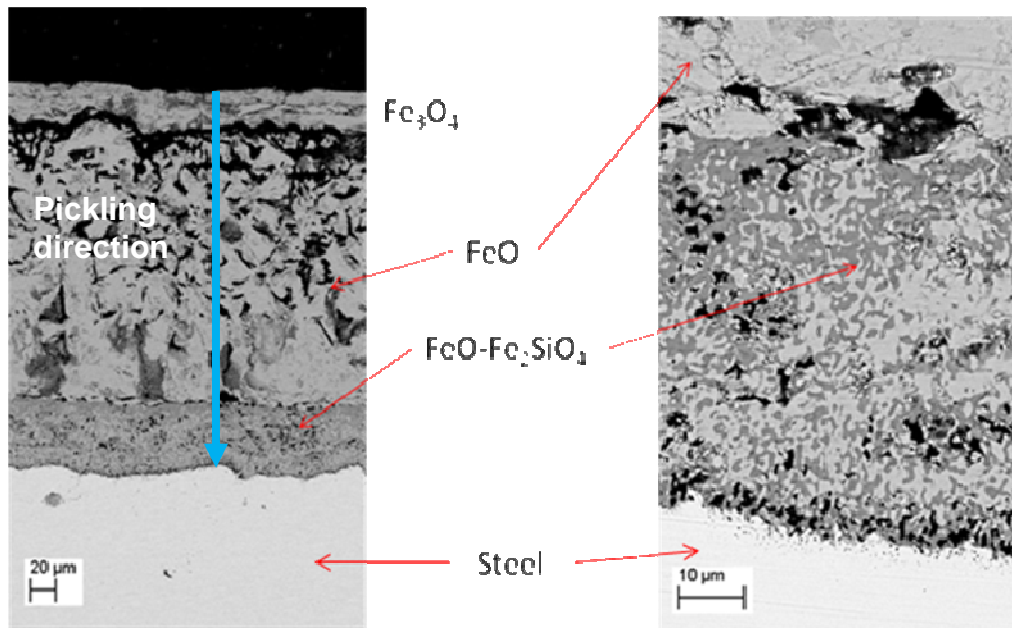


Figure V. 1: Cross-section SEM micrograph of the steel sample after oxidation at 1100°C in air with 15% relative humidity during 15 minutes.

Si16 scale formed at 1200°C is composed of three parallel layers: a wüstite layer, a fayalite internal layer containing wüstite small grains and a layer with fayalite infiltrations into the steel substrate (Figure V. 2). The total thickness of this scale is about 530 μm.

As for the previous sample (Si16-fayalite grains), hematite was absent at the top of the scale layer. But in the present case no magnetite external layer was obvious. After 1 min of oxidation the wüstite layer has a thickness of about 430 μm; this higher value is due to the enhanced iron diffusion through the melted fayalite-wüstite eutectic (Figure I. 7). Another important difference between the two samples is the morphology of the fayalite phase: there are grains embedded in wüstite for the Si16-fayalite grains sample, and a continuous layer in the present case with a thickness of about 100 μm.

This sample will be called **Si16-fayalite layer** in this chapter

For the two samples, the “wüstite” phase is a mixture of wüstite, and iron + magnetite eutectoid due to wüstite transformation below 570°C (Figure I. 9 and Chapter III), but for simplicity it will be called “wüstite” in this thesis report.

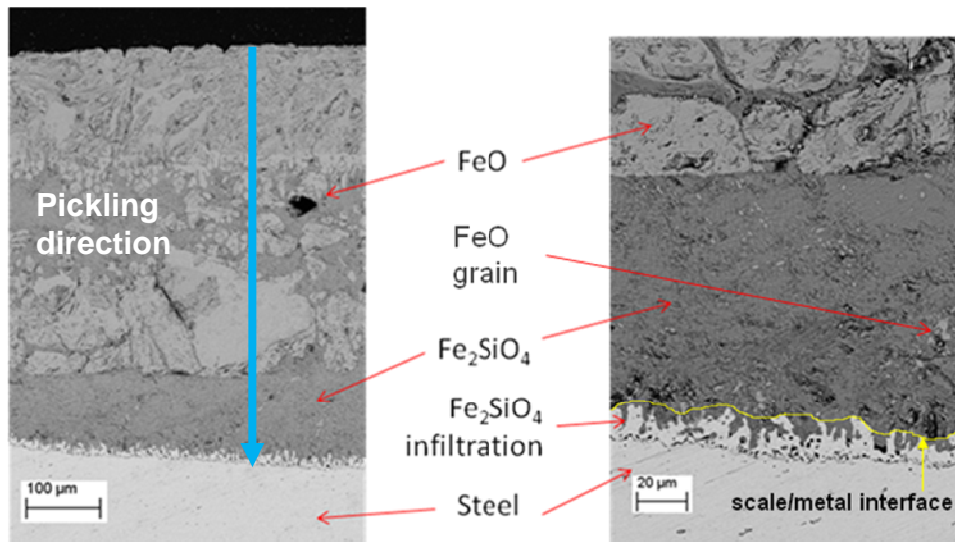


Figure V. 2: Cross-section SEM micrograph of the steel sample after oxidation at 1200°C in air with 15% relative humidity during 1 minute.

V. 3. Electrochemistry of scale dissolution

The electrochemical behaviour of **Si16-fayalite grains** and **Si16-fayalite layer** samples will be presented and compared to a Si00-model scale without hematite outer layer (Annex III) to have similar iron oxides outer layers for the three samples.

V. 3. 1. Corrosion potential E_{corr}

The corrosion potential evolution during pickling and over-pickling of Si00-model scale (reference sample without hematite), Si16-fayalite grains and Si16-fayalite layer samples (scale thicknesses in section V. 2.) are shown in Figure V. 3.

Si16-fayalite grains

In Figure V. 3a, at the beginning of immersion, the corrosion potential was well defined and had a value of about + 0.3 V/SCE then it decreases slowly until reaching + 0.15 V/SCE after nearly 3 hours. In comparison with Si00-model scale without hematite (Figure V. 3c), the E_{corr} value is less positive in Si16-fayalite grains scales, though the composition of the oxide is the same (magnetite and wüstite). At this stage, it is difficult to say whether this is due to the formation of silicon oxides in the scale internal layer or to the different heat treatments during the synthesis. The positive value was maintained for a period of 3.5 hours, after which an almost instantaneous jump was observed to a value of - 0.3 V/SCE, and then it decreases slowly during 1.5 hour to reach a value of - 0.45 V/SCE close to the corrosion

potential measured on bare steel in the same electrolyte. After nearly 5 hours the corrosion potential kept a roughly constant value.

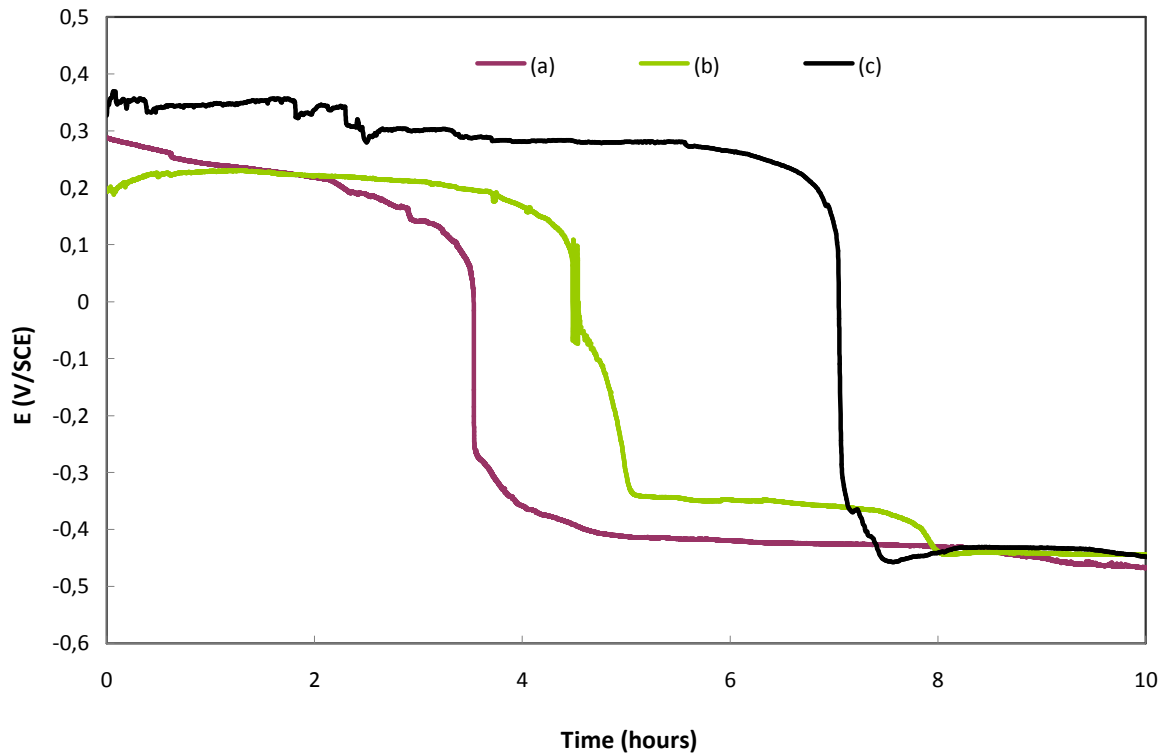


Figure V. 3: Evolution of corrosion potential during scale dissolution in 1M HCl acid solution at room temperature of (a) Si16-fayalite grains sample, (b) Si16-fayalite layer sample and (c) Si00-model scale without hematite outer layer sample.

The slow decrease of the corrosion potential after the jump, instead of the abrupt decrease observed for the Si00-model scale sample (Figure V. 3c) can be attributed to the presence of fayalite grains in the intermediate layer, which delays the corrosion potential from reaching the bare steel values after the potential jump.

Si16-fayalite layer

In Figure V. 3b, during the first 4 hours of immersion, the corrosion potential kept a stable value at 0.2 V/SCE then starts to decrease slowly during 30 minutes to a value of about 0 V/SCE where it oscillates during few minutes before descending to - 0.35 V/SCE after 5 hours. A corrosion potential pseudo-plateau is observed at this value during 2.5 hours before decreasing to the bare steel potential - 0.45 V/SCE after 8 hours of immersion.

The potential pseudo-plateau observed after the jump at -0.35V/SCE can be attributed to the presence of the continuous fayalite layer which acts like a passive layer and delays significantly the potential from reaching the corrosion potential value of the bare steel.

As mentioned previously, an obvious difference between Si16-fayalite grains and Si16-fayalite layer samples is the presence in the first sample of a well defined magnetite layer at the top of the scale. The progressive dissolution of magnetite can explain the monotonous decrease of E_{corr} during the first 3 hours, in comparison with the latter sample in which E_{corr} keeps a roughly constant value during this time. Moreover, for Si16-fayalite grains sample, the time necessary for the solution to reach the metallic substrate is lower than in Si16-fayalite layer sample, this can be attributed to the lower scale thickness ($280\ \mu\text{m}$ and $530\ \mu\text{m}$ respectively) and the presence of a wüstite matrix in the internal layer easier to dissolve in comparison with a fayalite layer.

The main difference between the two samples is observed after the potential jump; when fayalite grains are embedded in wüstite, the potential decreases progressively before reaching the E_{corr} value of the steel substrate. When fayalite constitutes a continuous layer, a potential plateau at -0.35V/SCE is observed during few hours, which delays significantly the overall process.

The electrochemical reactions sets fixing the corrosion potential at the successive scale dissolution phase will be discussed later in this chapter.

V. 3. 2. Corrosion current density I_{corr}

V. 3. 2. 1. Current-potential curves

As for Si00-model scale, potentiodynamic measurements were performed in the anodic and cathodic potential ranges on Si16-fayalite grains and Si16-fayalite layer samples, showing a Tafel behaviour in the cathodic range. The corrosion current (I_{corr}) could then easily be determined by extrapolating $\log I$ to the open circuit potential.

Examples of current-potential curves of Si16-fayalite grains and Si16-fayalite layer samples at different times of dissolution in $\text{HCl } 1\ \text{mol.L}^{-1}$ are presented in Figure V. 4 and Figure V. 5 respectively.

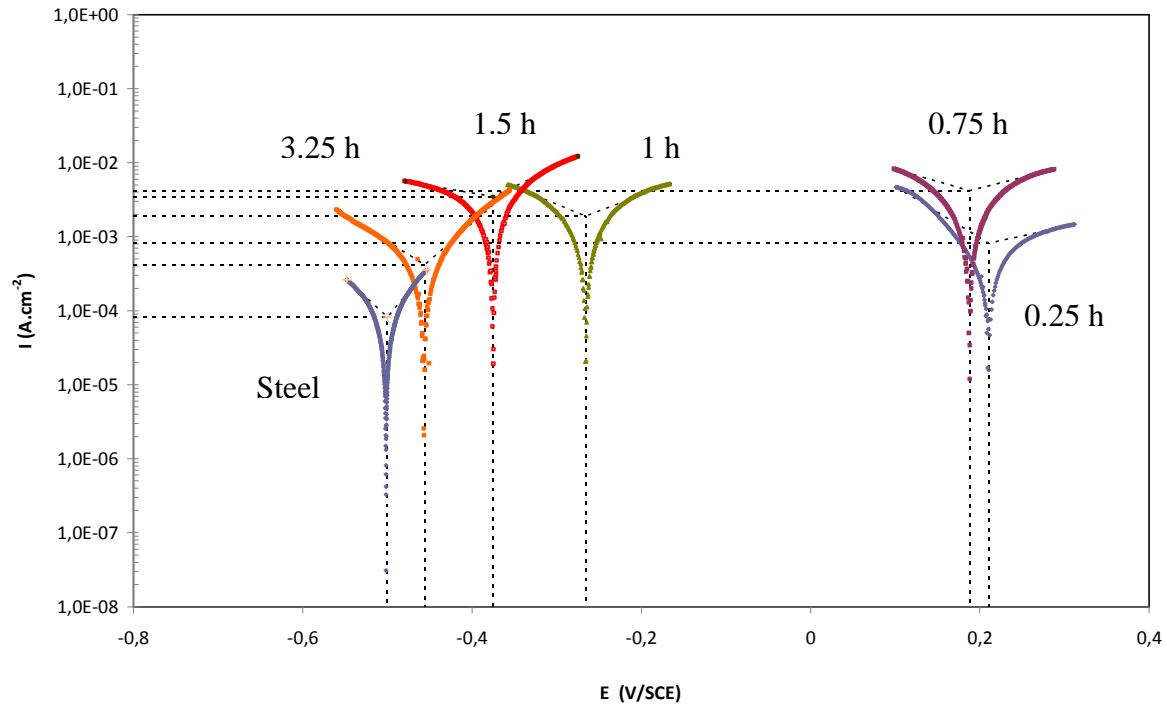


Figure V. 4: Current-potential curves (scan rate 1 mV/s) plotted for different immersion times (0.25 h, 0.75 h, 1 h, 1.5 h and 3.25 h), for Si16-fayalite grains sample and scale free steel electrodes.

The form of the current-potential curves of Si16-fayalite grains and Si16-fayalite layer samples are similar to those of Si00-model scale in the same potential range (Figure IV. 3). Indeed, the three samples have in common the conductive wüstite phase in contact with acid and a steel substrate in which iron is the main element.

The faster temporal evolutions of the discrete corrosion potential values reported in Figures V. 4 and V. 5 in comparison with the continuous corrosion potential of Figure V. 3, are likely to be due to the perturbation of the sample by the imposed polarization. This potential scan is necessary for the corrosion current determination by the Tafel method.

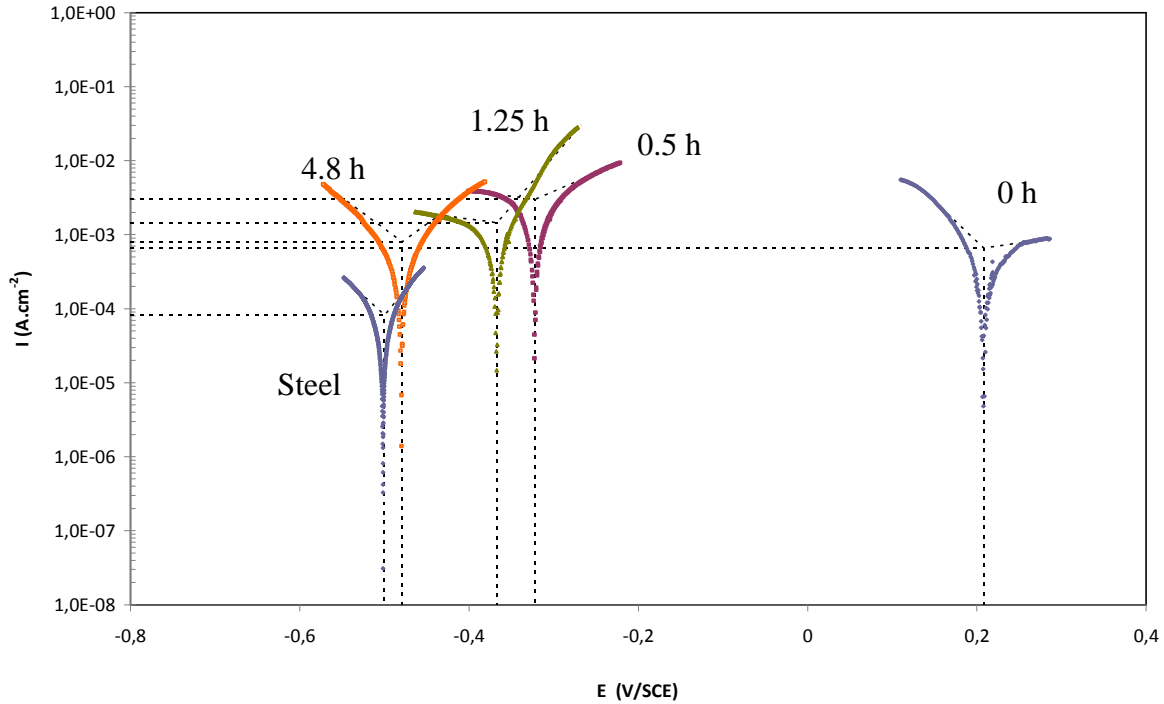


Figure V. 5: Current-potential curves (scan rate 1 mV/s) plotted for different immersion times (0 h, 0.5 h, 1.25 h and 4.8 h), for Si16-fayalite layer sample and scale free steel electrodes.

V. 3. 2. 1. Evolution of the corrosion current density

The corrosion current density determined from current-potential curves is plotted as a function of immersion time for Si16-fayalite grains and Si16-fayalite layer samples.

Si16-fayalite grains sample

The corrosion current density determined from current-potential curves is plotted as a function of immersion time in Figure V. 6. The corresponding corrosion potential value is also reported, and appears to vary similarly to the variations given in Figure V. 3. The shorter period of the positive potential is likely to be due to the perturbation of the sample by the polarization measurements imposed each 15 minutes for the corrosion current determination and a less cohesive or more decomposed wüstite in the presence of fayalite grains in the scale internal layer. This accelerates the infiltration and dissolution of the wüstite to reach the steel substrate.

At the beginning of immersion, the corrosion current density was very low, with a value of about 0.2 mA.cm^{-2} in agreement with a wüstite dissolution. The current increases monotonically, up to the potential jump which is observed after 0.7 hours. The increase in the corrosion current density is likely to be linked to the increase of the active surface in a wüstite

porous electrode. After 0.7 hours of immersion, the corrosion current density decreases by 2 units then reached a second peak after 1.5 hour with a value of $3.5 \text{ mA}\cdot\text{cm}^{-2}$. After this second peak the corrosion current decreases down to $0.5 \text{ mA}\cdot\text{cm}^{-2}$ and kept this value until the end of the measurement.

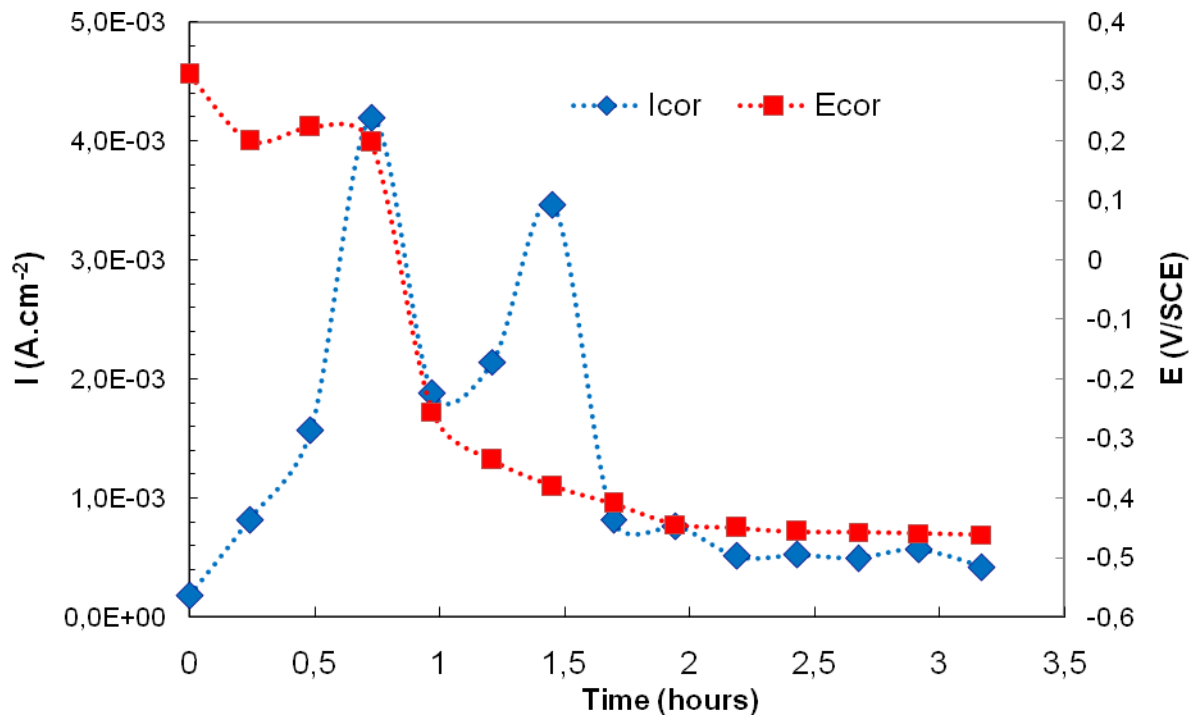


Figure V. 6: Evolution of corrosion potential and corrosion current density during Si16-fayalite grains scale dissolution in $\text{HCl } 1 \text{ mol}\cdot\text{L}^{-1}$ at room temperature.

The second current peak occurred while the potential was decreasing slowly which was attributed to the presence of the wüstite-fayalite grains internal layer. It was difficult to say if this peak was attributed to an artefact since only one experiment was made and its results treated or to a physical phenomenon. For this reason, this second peak will not be discussed.

This behaviour is different from the one observed for Si00-model scale with hematite outer layer (Figure IV. 4). The main differences appear before and after the potential jump. At first, the time needed to reach the potential jump is much lower in the Si16 model scale samples, indicating a less protective outer scale than for Si00-model scale. This observation is in agreement with the lower value of the corrosion potential of Si16 model scale samples in comparison with the Si00-model scale without hematite sample (Figure V. 3). The second difference is after the jump, the lower decrease of the corrosion current density in the

presence of fayalite in comparison with Si00-model scale. For Si16-fayalite grains sample, the corrosion current density decreased from 4 to 0.5 mA.cm⁻² during the 2 hours following the jump (the second peak was not considered) (Figure V. 6) while it decreased from 8 to 0.3 mA.cm⁻² for Si00-model scale samples (Figure IV. 4).

Si16-fayalite layer sample

The corrosion current density determined from current-potential curves is plotted as a function of immersion time in Figure V. 7. The corresponding corrosion potential value is also reported, and appears to vary similarly to the variations given in Figure V. 3. The shorter period of the positive potential is likely to be due to the perturbation of the sample by the polarization measurements imposed each 15 minutes for the corrosion current determination and a more fragile wüstite layer above the fayalite internal layer.

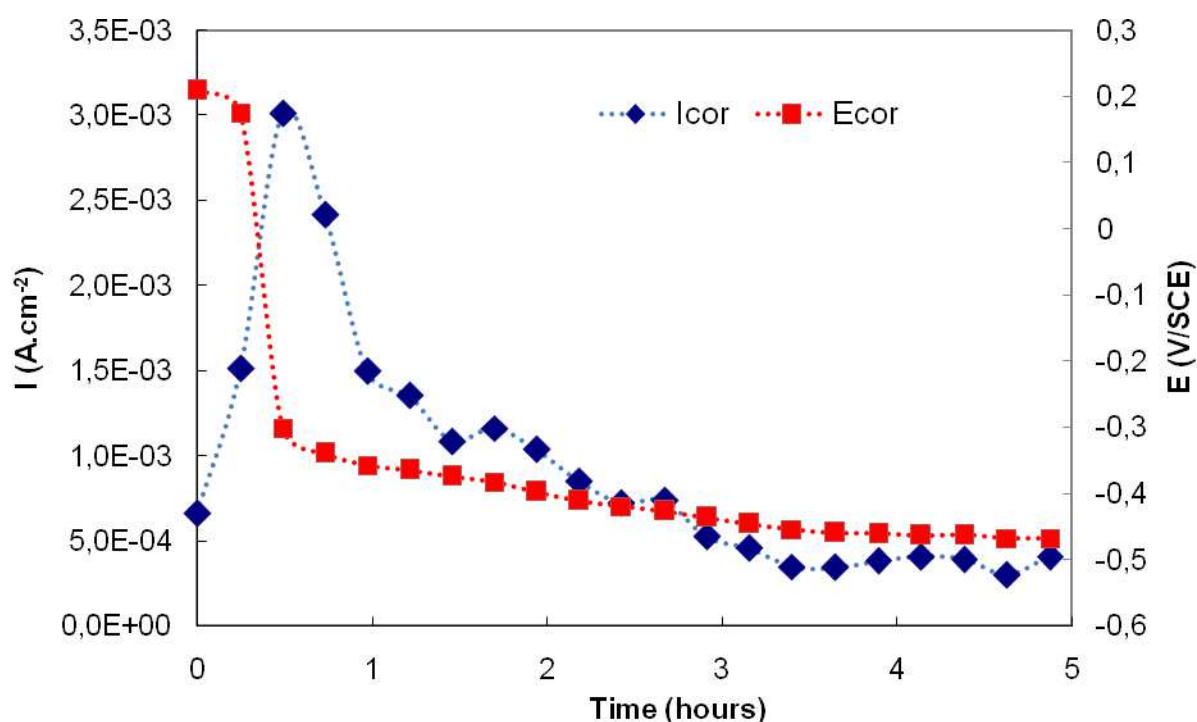


Figure V. 7: Evolution of corrosion potential and corrosion current during Si16-fayalite layer scale dissolution in HCl 1 mol.L⁻¹ at room temperature.

At the first 0.5 hours of immersion the positive corrosion potential is close to 0.2 V/SCE and the corrosion current increases from 0.6 mA.cm⁻² to a peak at 3 mA.cm⁻². This corresponds to the dissolution of wüstite in a porous electrode mode already observed for Si16-fayalite grains and Si00-model scale samples.

After the potential jump, the electrolyte is in contact with steel substrate through micro-cracks in fayalite. The slow decrease of the corrosion current occurs simultaneously

with the pseudo plateau of the corrosion potential during 3 hours. It can be attributed to a decrease of the reactive surface by removal of the remaining wüstite above the fayalite internal layer.

The higher values of the corrosion current at the beginning of immersion of Si16-fayalite grains and Si16-fayalite layer samples in comparison with Si00-model scale with hematite and magnetite outer layers confirms the more passivating behavior of the scale in the latter case. The increase of the corrosion current density in the wüstite phase of the three samples is attributed to the high reactive surface (porous electrode behavior). The corrosion current density peak is similar for the three samples and corresponds to the high electrochemical dissolution of the steel substrate at this high anodic potential, when the acid reaches the metal. The high corrosion current values after the potential jump confirm the presence of wüstite after this jump and the coexistence of pickling and over-pickling.

V. 4. Total dissolution of scale

The dissolution rate of iron and silicon was only followed for the Si16-fayalite layer sample using ICP-AES during the pickling process, and the overall variation with time is shown in Figure V. 8 . The evolution of the open-circuit potential E (ICP) was measured simultaneously. Its evolution is similar to the evolution observed during electrochemical measurements E (EC), which is also reported in Figure V. 8. E (ICP) had an anodic value (about 0.2 V/SCE) at the beginning of the dissolution process, followed by an abrupt drop towards - 0.5 V/SCE after several hours. For easier comparison between electrochemical results and ICP measurements, a dimensionless time t_{dim} is reported on the abscissa of Figure V. 8. It is defined as the ratio between the elapsed time and the time corresponding to the potential jump. Moreover, from the corrosion current densities reported in Figure V. 7, the electrochemical dissolution rate calculated using Faraday's law (taking one electron as a first approximation) is also reported for comparison with the total dissolution rate of iron.

As for Si00-Model scale, the method above will be used to evaluate the electrochemical contribution in the total dissolution of scale.

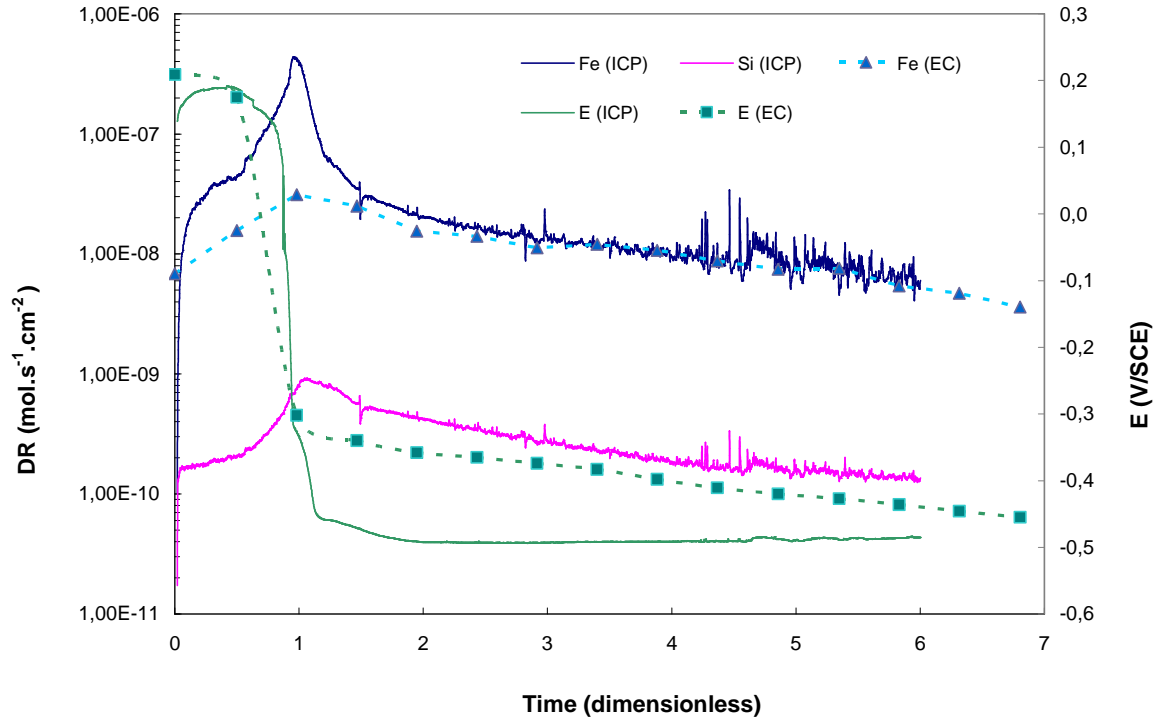


Figure V. 8: Comparison between the electrochemical and total dissolution rates of Si16-fayalite layer sample measured by ICP-AES in 1 M HCl solution at room temperature.

V. 4. 1. Total dissolution rate (TDR)

During scale dissolution at the positive corrosion potential, the total dissolution rate of iron increased to reach a peak at the potential drop with a value of $300 \mu\text{mol.s}^{-1}.\text{cm}^{-2}$. After the peak, the dissolution rate of iron decreased rapidly then slowly with successive short time peaks after $t_{\text{dim}} = 4$.

The silicon dissolution rate follows a similar evolution with a delay due to the dissolution first of the wüstite layer. The dissolution peak of silicon is only reached after the potential drop with a value of $1 \mu\text{mol.s}^{-1}.\text{cm}^{-2}$. After the peak, the silicon dissolution rate decreased slowly and shows also short time peaks after $t_{\text{dim}} = 4$.

The dissolution peak of iron is attributed to the wüstite layer dissolution and the silicon to the liberation of fayalite particles in the pickling bath. The slow decrease of the total dissolution rate of iron and silicon can be attributed to the continuous dissolution of the remaining wüstite and the removal of fayalite and wüstite particles (small peaks after $t_{\text{dim}} = 4$).

V. 4. 2. Electrochemical contribution in scale dissolution

As fayalite is an insulating layer, its electrochemical dissolution was neglected. The electrochemical dissolution of this sample concerns mainly iron oxides (wüstite and magnetite from wüstite decomposition) and the steel substrate.

An average ratio $v_{EC}/v_{tot} = 1/4$ was observed before the potential jump. This ratio is similar to the one observed for Si00-model scale after the removal of its hematite and magnetite layers (dissolved mainly chemically) and during the wüstite dissolution just before the potential jump. Since these outer layers are absent in Si16-fayalite layer, the 1/4 ratio corresponds to the dissolution of the decomposed wüstite present in both Si16-fayalite layer and Si00 model scale samples (see chapter IV).

At the potential drop, v_{EC}/v_{tot} ratio decreased to 1/10. At this stage, mechanical detachment of wüstite and fayalite particles can explain the increase in iron dissolution rate detected by the ICP-AES when the acid reaches the metal.

After the potential jump, the total dissolution rate decreased faster in comparison with the electrochemical rate making the v_{EC}/v_{tot} ratio tend to 1 after $t_{dim} = 3$. This value shows that when the acid is in contact with the steel substrate the electrochemical process becomes dominant in over-pickling but also in the dissolution of the remaining oxides. These oxides are dissolved electrochemically or removed as particles (small peaks) by corrosion of the steel substrate.

The observations above confirmed the pickling mechanism of wüstite just before the potential jump (chapter IV). The presence of the silicon peak showed that the fayalite layer is not completely passive and continuous. It can be infiltrated by the acid through micro-cracks or the wüstite small grains. It is liberated in the pickling bath as small particles.

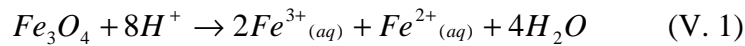
V. 5. Pickling and over-pickling (O-P) mechanism

As for the Si00 model scale, the transition between pickling and over-pickling will be considered at the potential drop from positive to negative values in the cases of Si16-fayalite grains and Si16-fayalite layer samples, though at this stage oxide layers are not completely removed.

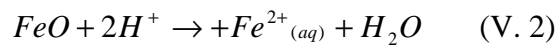
V. 5. 1. Pickling steps and reactions

As the outer scale for both Si16-fayalite grains and Si16-fayalite layer samples is composed mainly of the decomposed wüstite and its electrochemical and total dissolution behaviour is similar to the one observed for Si00 model scale after the removal of the hematite and magnetite external layers, the pickling steps and reactions during wüstite dissolution proposed in chapter IV can be applied in the present case.

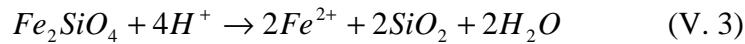
The **chemical reactions** concerns **magnetite**:



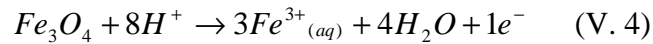
wüstite:



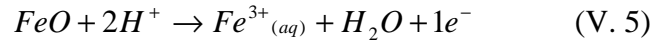
and also **fayalite** but with a slow dissolution rate and before the acid reaches the steel substrate:



The positive corrosion potential is the result of the **anodic reactions** of **magnetite**:



and **wüstite**:



and the **cathodic reaction** is the reduction of **Fe³⁺**:



The dissolution mechanism of the internal layers depends on its morphology

Si16-fayalite grains sample

After dissolution of the magnetite and wüstite layers, the acid dissolves the wüstite matrix of the internal layer and liberates the fayalite grains in the solution.

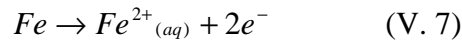
Si16-fayalite layer sample

After dissolution of the outer wüstite layer, the acid infiltrates the fayalite layer through micro-cracks or wüstite grains to reach the steel/scale interface.

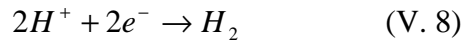
V. 5. 2. Over-pickling steps and reactions

For both samples, when the acid reaches the internal layer/steel substrate interface, the potential drop implies the same new set of electrochemical reactions.

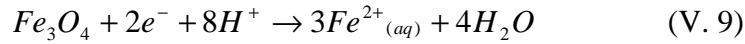
The **anodic reaction** becomes the corrosion of **iron** from the steel substrate:



And the **cathodic reactions** correspond to the reduction of H^{+} on steel substrate only:



and **magnetite** from the remaining decomposed wüstite:



The over-pickling mechanism depends on the internal layer morphology.

Si16-fayalite grains sample

When the acid reaches the steel substrate after dissolution of the wüstite matrix, the metal is corroded. At the same time, the remaining wüstite matrix continues its dissolution by reduction of its magnetite. The low solubility of fayalite grains delays the removal of the intermediate layer.

If the reduction of protons is assumed to be on steel surface exclusively, the slow decrease of the corrosion potential after the potential jump can be explained by the evolution of the cathodic current (or surface) of magnetite versus the cathodic current (or steel surface) of the protons. Indeed, the magnetite surface (or cathodic current of magnetite) decreases slowly due to the presence of fayalite grains while at the same time the steel surface (anodic current of iron and cathodic current of protons) increases by removal of scale. The potential stabilizes after removal of the major part of scale.

Si16-fayalite layer sample

When the acid reaches the steel substrate after infiltration of the fayalite layer through micro-cracks and wüstite small grains, the metal is corroded. At the same time, the remaining wüstite above the fayalite layer continues its dissolution by reduction of its magnetite particles. The low solubility of fayalite layer delays the removal of the intermediate layer.

As for the other sample, the reduction of protons was assumed to be on steel surface exclusively. The pseudo plateau of the corrosion potential after the potential jump can also be explained by the evolution of the cathodic current (or surface) of magnetite versus the cathodic current (or steel surface) of the protons adapted to the fayalite layer. Indeed, the magnetite surface (or cathodic current of magnetite) in the remaining upper wüstite layer decreases slowly while the low soluble fayalite layer covers the major surface of steel (anodic current of iron and cathodic current of protons). The potential stabilizes after removal of the major part of the fayalite layer. Fayalite infiltrations resist to pickling and reduce the reactive surface for over-pickling for this sample.

In comparison with Si00, two main differences are evidenced:

- The oxide layer made of wüstite (and/or decomposed wüstite) shows a higher reactivity in the case of Si alloyed scale, even when fayalite grains are embedded in the oxide.
- Once the electrolyte has reached the metal, over-pickling is necessary to remove progressively the fayalite layer. According to Figure V. 8, the dissolution rate of Si is still significant during over-pickling.

For all samples, when the acid is contact with iron oxides and fayalite phases only, chemical and electrochemical reactions occur and once the acid reaches the steel substrate, the remaining scale and steel substrate dissolution is electrochemical. Particles mechanical detachment occurs during both pickling and over-pickling.

V. 6. Influence of some parameters on pickling and O-P mechanism

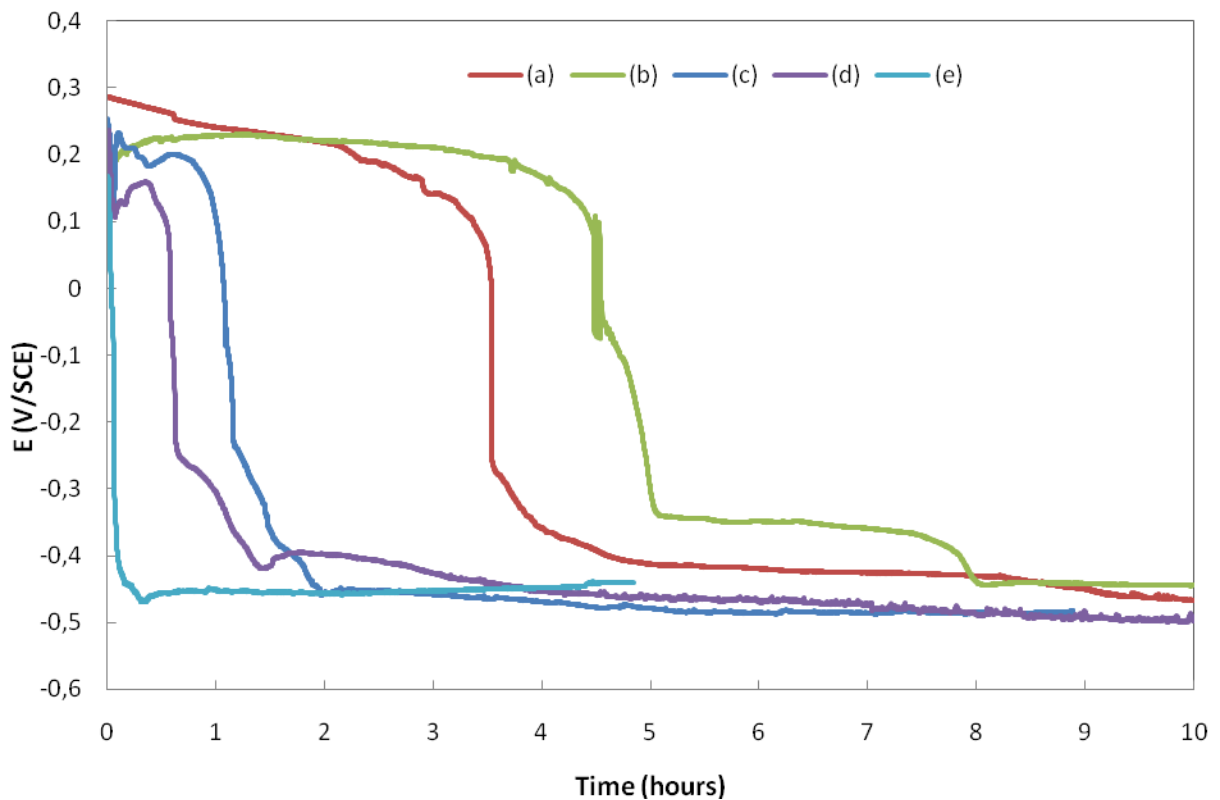


Figure V. 9: Temporal evolution of corrosion potential during dissolution of low carbon steel scales in different conditions: (a) Si16-fayalite grains in HCl 1 mol.L⁻¹ at room temperature (b) Si-16 fayalite layer in HCl 1 mol.L⁻¹ at room temperature (c) Si16-fayalite grains in HCl 3 mol.L⁻¹ at room temperature (d) Si16-fayalite grains in HCl 1 mol.L⁻¹ at 50°C and (e) Si16-fayalite layer in HCl 1 mol.L⁻¹ at 50°C.

The pickling and over-pickling mechanisms described above concern a model scale with the fayalite grains or continuous layer in soft pickling conditions. These conditions allow the monitoring of different pickling steps and offer enough time for their characterization.

To correlate the proposed mechanism with industrial conditions, a non exhaustive list of oxidation and pickling parameters closer to industrial conditions is studied to evaluate their effect on pickling mechanism and kinetics. The corrosion potential evolution of Si16 steel scales in some different pickling conditions is presented in Figure V. 9.

Due to the presence of fayalite at wüstite/steel interface, the “pickling time” for silicon steels was chosen as the time needed to reach the corrosion potential of steel as a first approximation.

V. 6. 1. Scale morphology and composition

V. 6. 1. 1. Influence of fayalite morphology

The pickling times at room temperature in HCl 1M for Si16-fayalite grains and Si16-fayalite layer samples were compared (Figure V. 9 a and b). In both cases, the presence of fayalite delays the reaching of the corrosion potential of the bare metal after the potential jump in comparison with Si00 model scale (Figure V. 3). For Si16-fayalite layer sample, the negative plateau after the potential jump takes nearly three hours while a slow decrease of the potential during nearly 1 hour after the potential jump is observed for Si16-fayalite grains sample.

V. 6. 1. 2. Behaviour of industrial scale

The evolution of the dissolution rates of iron and silicon of both industrial scales formed in the hot strip mill (HSM) on a 1.8 wt.% Si (0.003 wt.% C) steel and a Si16 model steel are reported in Figure V. 10.

A dissolution peak of both iron and silicon and a negative corrosion potential are observed immediately after immersion in the acid. This confirms that scale of industrial samples is thin and cracked, and therefore the over-pickling starts immediately.

The intersection between the curves of the iron dissolution from scale and from steel corresponds to the time needed to remove the wüstite phase. Similarly, the intersection between the curves of the silicon dissolution from scale and from steel corresponds to the time needed to remove the fayalite phase. After the intersections the dissolution rate of the steel substrate under scale is lower than that of polished due to the presence of fayalite infiltrations.

This can be due to a lower reactive surface of metal and showing a partially blocked electrode behaviour or to the silicon depletion underneath scale to form silica and fayalite during thermal oxidation.

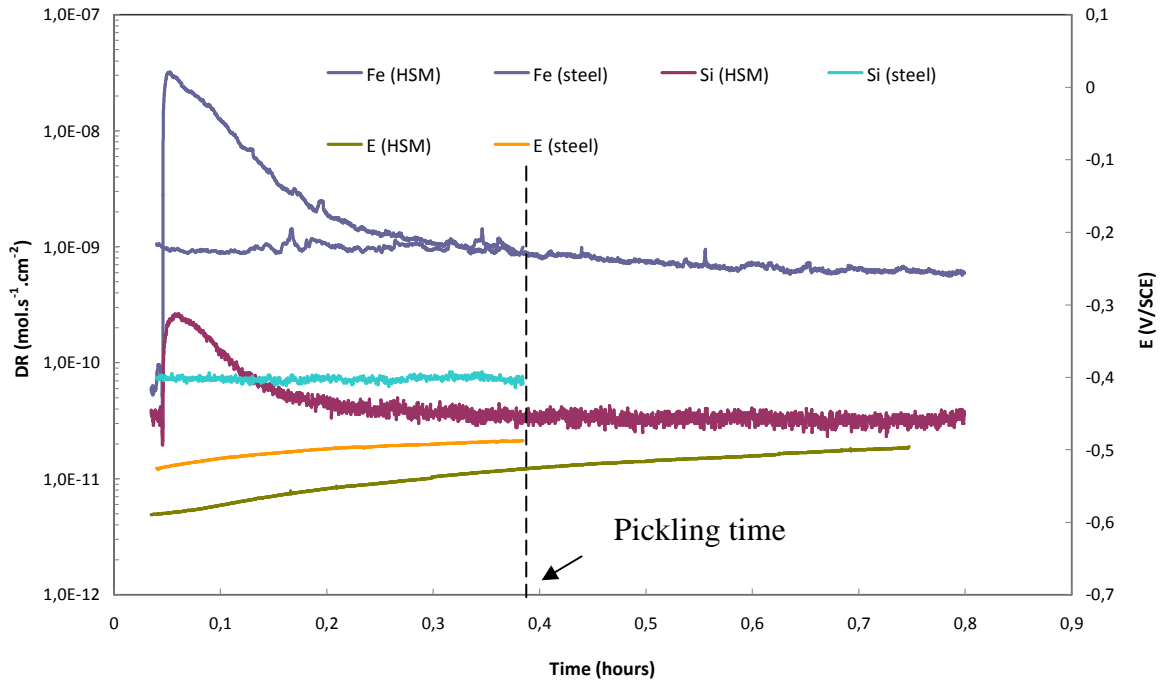


Figure V. 10: Temporal evolution of total iron and silicon dissolution rate and corrosion potential of a 1.8 wt% Si (0.003 wt% C) steel industrial scale (HSM) and polished Si16 steel (model steel) during dissolution in HCl 1 mol.L⁻¹

V. 6. 2. Influence of pickling bath temperature

For Si16-fayalite grains sample, the comparison of the time needed to reach the potential jump in HCl 1 mol.L⁻¹ at room temperature and 50 °C (Figure V. 9 b and d) showed that the pickling time decreased by nearly 80 % from 3.5 hours to 0.7 hours respectively.

The dissolution rate evolution of iron and silicon of Si16-fayalite layer sample during its dissolution in HCl 1 mol.L⁻¹ at 50°C is reported in Figure V. 11.

For Si16-fayalite layer, the comparison of the time needed to reach the potential drop and the dissolution peak of iron and silicon at room temperature (1.3 hour in Figure V. 8) and at 50°C (0.5 hour in Figure V. 11), showed a decrease of pickling time of about 60 % in the ICP-AES cell conditions. The dissolution rate peak values (0.5 and 0.3 μmol.s⁻¹.cm⁻² at 50°C and 20 °C respectively) are similar at the two temperatures.

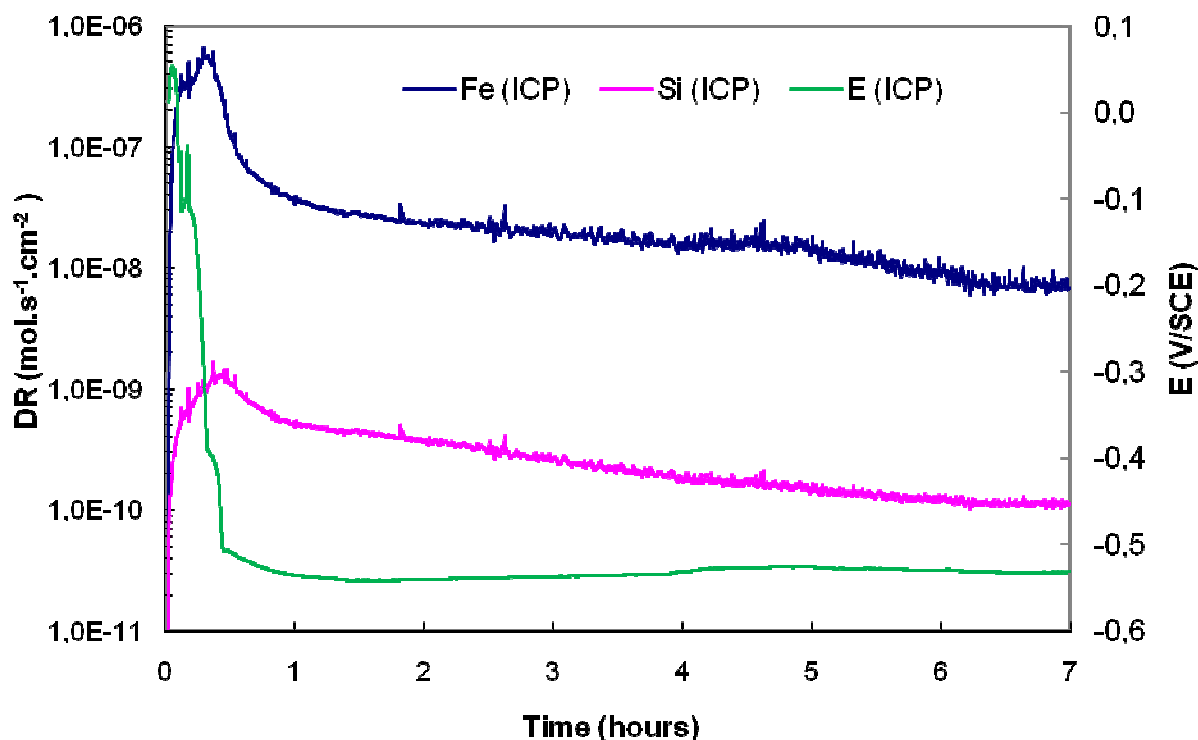


Figure V. 11: Temporal evolution of iron and silicon dissolution rates and corrosion potential of Si16-fayalite layer sample during dissolution in HCl 1 mol.L⁻¹ at 50°C.

V. 6. 3. Influence of acid concentration

For Si16-fayalite grains, the comparison of the time needed to reach the potential jump at room temperature in HCl 1 and 3 mol.L⁻¹ (Figure V. 9 b and c) showed that the pickling time decreased by nearly 63 % from 3.5 hours to 1.3 hours respectively.

The evolution of the dissolution rates of iron and silicon of Si16-fayalite layer during its dissolution in HCl 3 mol.L⁻¹ at room temperature is reported in Figure V. 12.

For Si16-fayalite layer sample, the comparison of the time needed to reach the potential drop and the dissolution peak of iron and silicon at room temperature in HCl 1 mol.L⁻¹ (1.3 hour in Figure V. 8) and at room temperature in HCl 3 mol.L⁻¹ (0.8 hour in Figure V. 12), showed a decrease of pickling time of about 40 % in the ICP-AES cell conditions.

As a conclusion, compared to the samples pickled at room temperature and in HCl 1M, higher temperature and acid concentration decrease the time needed for the solution to reach the metallic substrate, but the overall dissolution rates do not seem to be affected by a modification of these two factors in the conditions of the present work.

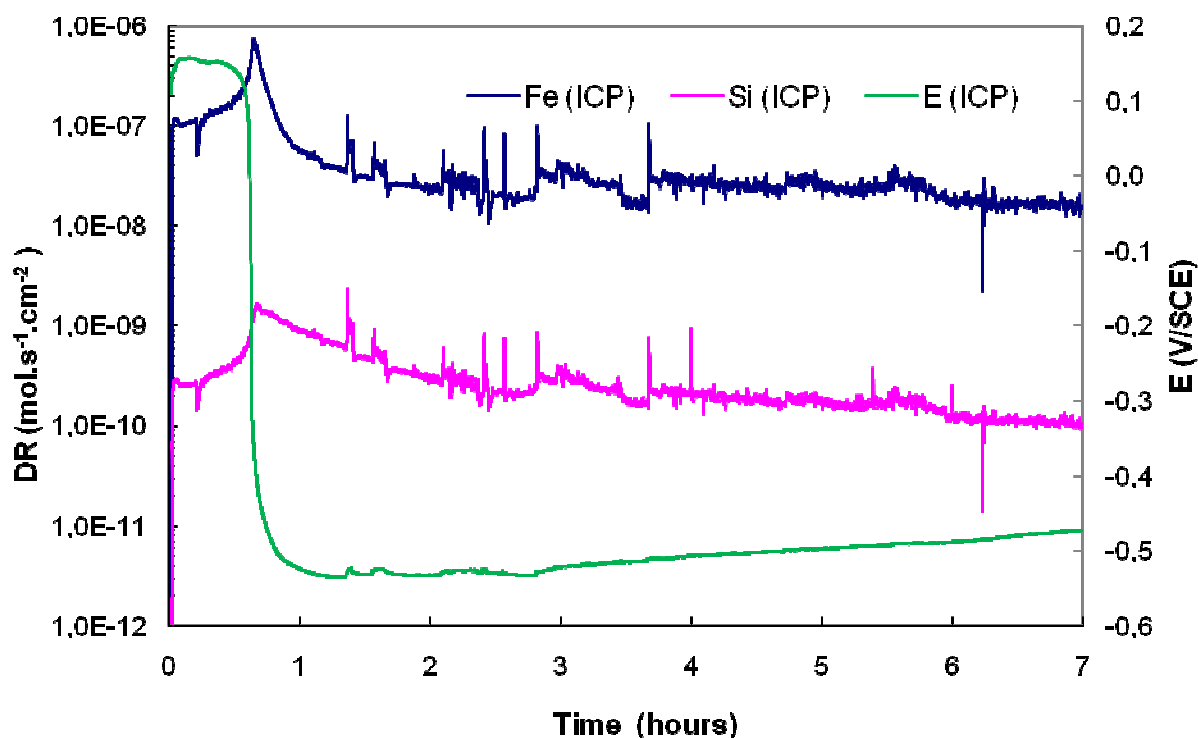


Figure V. 12: Temporal evolution of iron and silicon dissolution rates and corrosion potential of Si16-fayalite layer sample during dissolution in $\text{HCl } 3 \text{ mol.L}^{-1}$ at room temperature.

V. 7. Steel surface after pickling and over-pickling

Steel surface was observed by SEM-EDS to identify its chemical composition after pickling and over-pickling. The optical interferometry was used to evaluate the effect of a long over-pickling on steel surface roughness.

V. 7. 1. Steel surface after insufficient pickling

Steel surface of a pickled Si16-fayalite layer sample was observed after the negative potential plateau (Figure V. 3b) to identify its chemical composition (Figure V. 13). Even though the corrosion potential is negative with bare steel values, steel surface is not completely pickled since wüstite and fayalite covers part of this surface. The corrosion potential drop gives an approximation of pickling time but does not indicate the end of pickling.

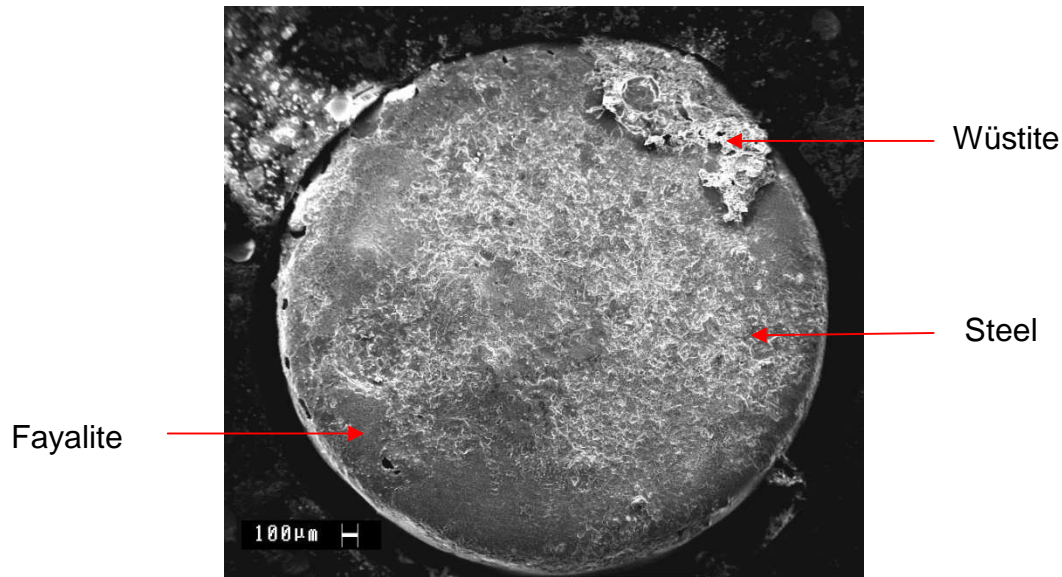


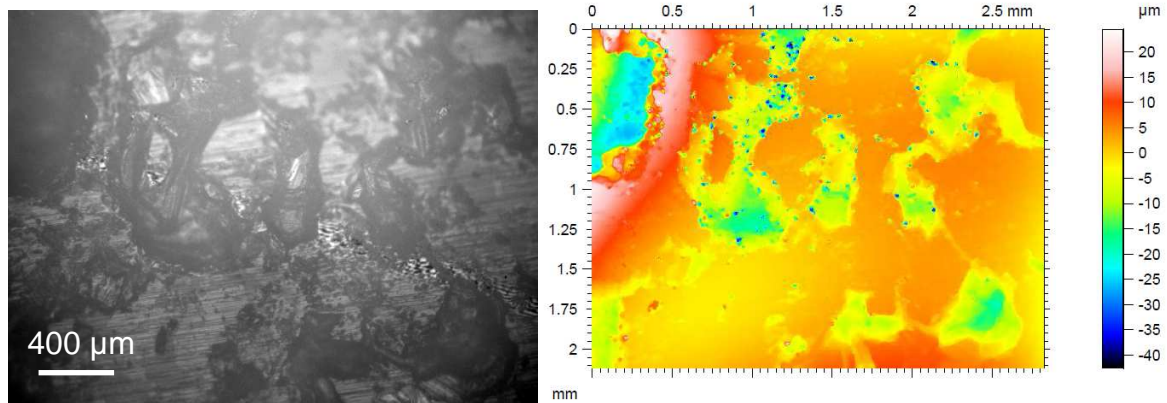
Figure V. 13: SEM micrograph of Si16-fayalite layer sample after 10 hours of pickling in HCl 1M at corrosion potential $E_{cor} = -0.45$ V/SCE.

V. 7. 2. Steel surface after over-pickling

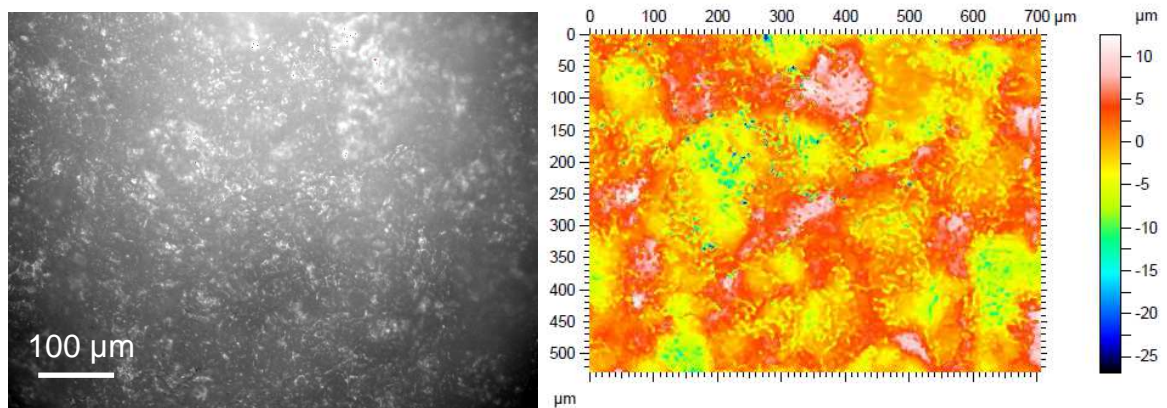
As for Si00 steel, the roughness change of polished (few seconds with a grit 800 to remove the fayalite internal layer) Si16-fayalite layer sample was observed with optical interferometry (chapter II) to reveal the effect of the fayalite infiltrations in the steel substrate after few minutes of immersion in the acid. This sample will be called Si16-fayalite infiltrations steel. Examples of Si16-fayalite infiltrations steel surface optical micrographs and roughness cartographies at 2 different times of immersion in an acid bath at room temperature, pickling lines temperature (70°C) and anodic potential are presented in Figure V. 14.

In addition to the surface cartography, two parameters were chosen to characterize the surface roughness: S_z and S_q representing the total height and average quadratic height respectively. They are expressed in μm and their evolution with over-pickling time, bath temperature and applied potential is presented in Figure V. 15.

(a)



(b)



(c)

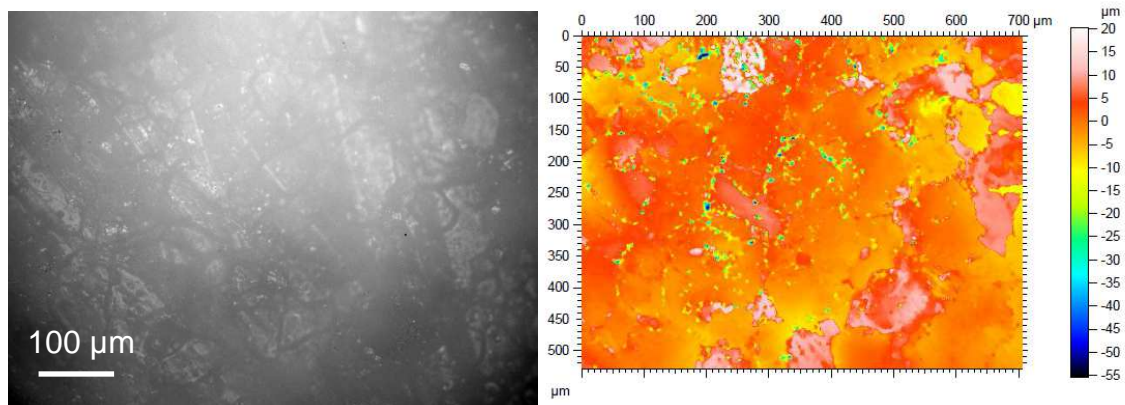


Figure V. 14: Examples of optical micrographs and roughness cartographies of a polished S16-fayalite surface (grit 800) after dissolution in $\text{HCl } 1 \text{ mol.L}^{-1}$: (a) before immersion (b) after 10 minutes of immersion at 70°C and (c) after 10 minutes of immersion at room temperature at anodic potential 0V/SCE .

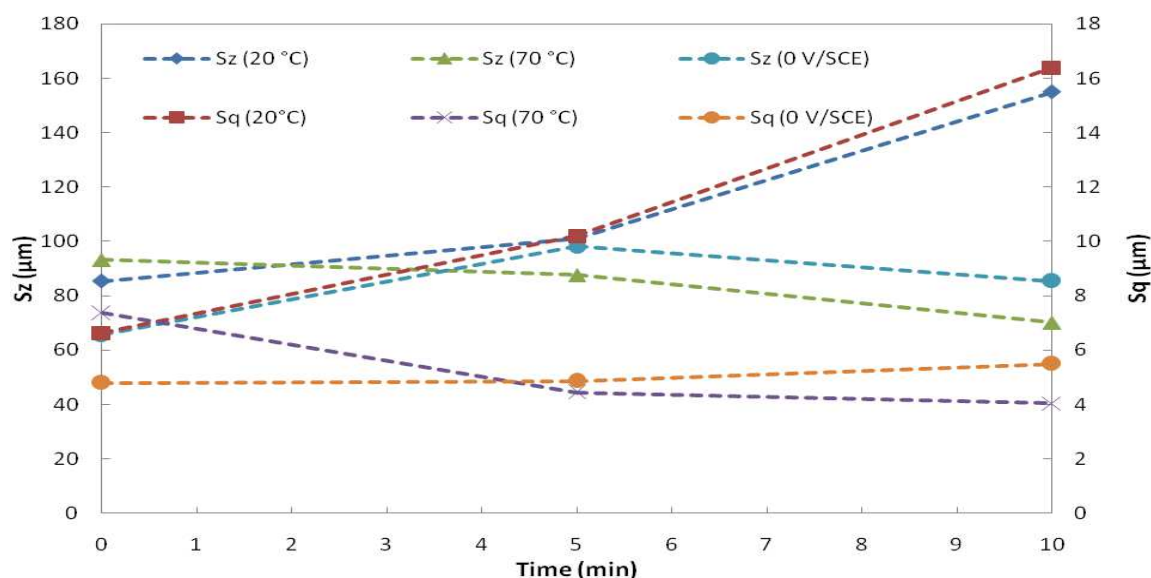


Figure V. 15: Evolution of roughness parameters Sz and Sq after 5 and 10 minutes of dissolution of Si16-fayalite layer sample polished (grit 800) in HCl 1 mol.L⁻¹

On Si16-fayalite infiltrations steel surface before dissolution, the dark zones corresponding to high fayalite infiltrations concentration are visible. The roughness of this surface was taken as a reference (Figure V. 14a).

The surface observations and evolution of roughness parameters of Si16-fayalite infiltrations steel surface (Figure V. 15) showed that the roughness increases significantly with over-pickling at room temperature. This can be due to the higher corrosion of the metal zones (holes) and the very low dissolution of the fayalite zones (heights). As for Si00 steel, the preferential corrosion at grains boundaries in metal zones can also contribute to the roughness increase. The differences in roughness parameters values of the 3 samples before immersion is due to the heterogeneity of their surface due to the fayalite infiltrations.

The roughness decreases slightly in the case of pickling at 70 °C. This can be due to a higher infiltration of the acid through fayalite and higher corrosion rate of the surrounding steel in this range of temperature. The removal of fayalite particles can contribute to the smoothing of the surface.

The roughness is almost constant at the 0 V/SCE applied potential. This anodic potential for iron was applied to accelerate the corrosion of iron surrounding the fayalite infiltrations. Indeed, the surface after 10 minutes is brighter which suppose the removal of more iron-fayalite particles and keeping the same roughness. A similar roughness can also come from less efficient dissolution at this applied potential.

V. 8. Conclusions

Iron oxides phases of silicon alloyed steel model scales were crossed by the acid faster than model scale of the low carbon steel even though they had higher thickness. This was attributed to a more fragile structure or wüstite decomposition due to the formation of fayalite grains or internal layer.

The external scale layers composed essentially of the decomposed wüstite were dissolved following the same mechanism of low carbon steel scale model by holes widening and removal of particles. The fayalite grains in the internal layer were mechanically detached in the solution by dissolution of the wüstite matrix. The fayalite layer was infiltrated slowly by the acid through micro-cracks or wüstite small grains and detached in the solution after a long corrosion of the steel substrate.

Before the acid reaches the metal, magnetite and wüstite are dissolved chemically and electrochemically. They represent the anodic reactions while reduction of Fe^{3+} coming from the chemical dissolution of magnetite initially represents the cathodic reaction. Fayalite can dissolve chemically but with a very low dissolution rate. The electrochemical contribution varied from 1/4 to 1/10 during scale dissolution. This ratio was similar to the one observed for the wüstite dissolution for the low carbon steel model scale since this phase is common in both grades.

The dissolution of the remaining scale internal layer with fayalite continues after the acid reaches the metal but with a different mechanism. The magnetite switches to a cathodic reaction in parallel with protons reduction while the anodic reaction is the corrosion of the steel substrate. The continuous reduction of magnetite and the low steel substrate surface available for protons reduction due to fayalite covering is responsible for the cathodic intermediate potential after the jump.

The electrochemical dissolution becomes dominant at bare steel corrosion potential. This means that the cathodic potential indirectly blocks the chemical reaction. The rest of scale is removed by particles.

For industrial scales, the cathodic potential is observed immediately after immersion in the acid and is not affected by the presence of silicon oxides since they are insulating. Pickling of these samples is also essentially electrochemical. The use of electrochemical methods to deal with the low soluble fayalite and its infiltrations can therefore be a good perspective for optimisation of pickling of silicon steels.

General Conclusion

The study of the mechanisms of pickling and over-pickling required synthesizing well defined scales which reproduce industrial scales usually obtained on steel in a hot strip mill. This was the aim of the first part of this work. Different oxidizing conditions were applied and the obtained scales were characterized using SEM, Raman spectrometry, XPS and Auger spectroscopies.

The main results on non alloyed carbon steels confirmed the mechanisms and scale characteristics found in the literature. Scale growth follows first linear then parabolic laws. The linear step corresponds to the oxidation of steel surface and the parabolic to iron ions oxidation after diffusion in scale. Model scales of low carbon steel grades are composed mainly of iron oxides layers with increasing oxidation degree for iron: wüstite (FeO), magnetite (Fe₃O₄) and hematite (Fe₂O₃). Wüstite is unstable below 570°C, it transforms partially into iron and magnetite eutectoid. Industrial scales are composed of thin and brittle wüstite due to mechanical pressure in the hot strip mill.

For silicon alloyed steel grades, the presence of silicon is expected to slow down the oxidation rate. In this work silicon contents between 1.6 and 3.2 wt.%, oxidation temperatures between 850 and 1200°C and humidity of the oxidizing atmosphere of 15% H₂O were explored. In comparison with non alloyed steels, the presence of silicon introduces a passivation period between the linear and parabolic steps of scale growth. This passivation period appeared for temperatures lower than 1177°C and disappeared at higher oxidation temperatures. The passivation period is due to the formation of a silica thin layer with a barrier effect for iron diffusion towards oxygen rich atmosphere, lowering the overall dissolution rate. Silica can also appear in the steel substrate, due to internal oxidation at grains boundaries. The presence of silica phase during passivation period was confirmed in this work by crossing different characterization methods. During oxidation, silica and wüstite are transformed into fayalite Fe₂SiO₄ and form a fayalite-wüstite internal layer. Above 1177°C, molten fayalite enhances iron diffusion and oxidation rate, and after cooling forms an internal layer with infiltrations in steel.

Silicon oxides or iron-silicon oxides were concentrated at the steel/scale interface and their morphology was depending on the oxidation temperature and time. Fayalite grains in wüstite matrix appeared between 900°C and 1100°C and continuous layer of fayalite-wüstite eutectic above 1177°C. For silicon content of 3.2 wt.% the passivation effect was so high that

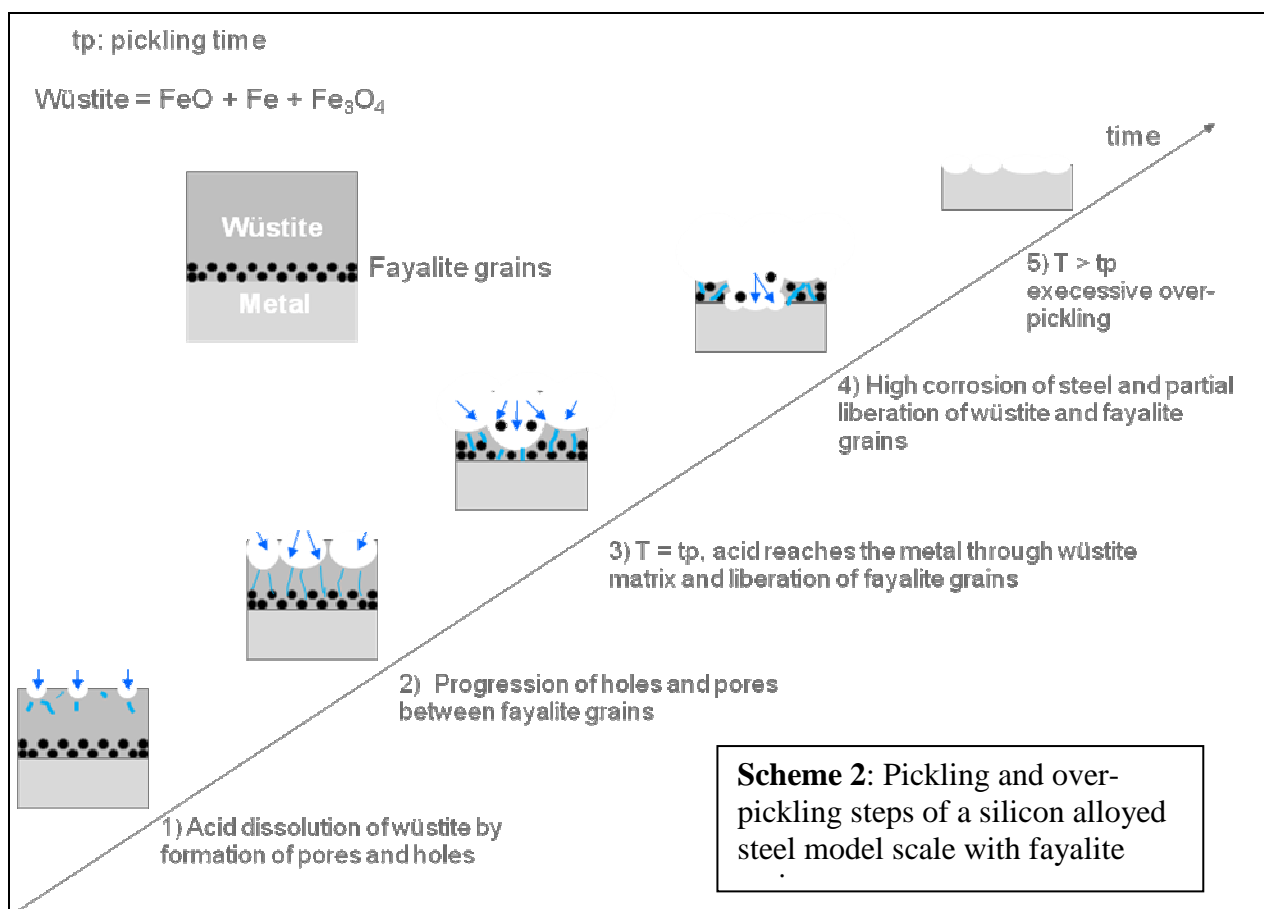
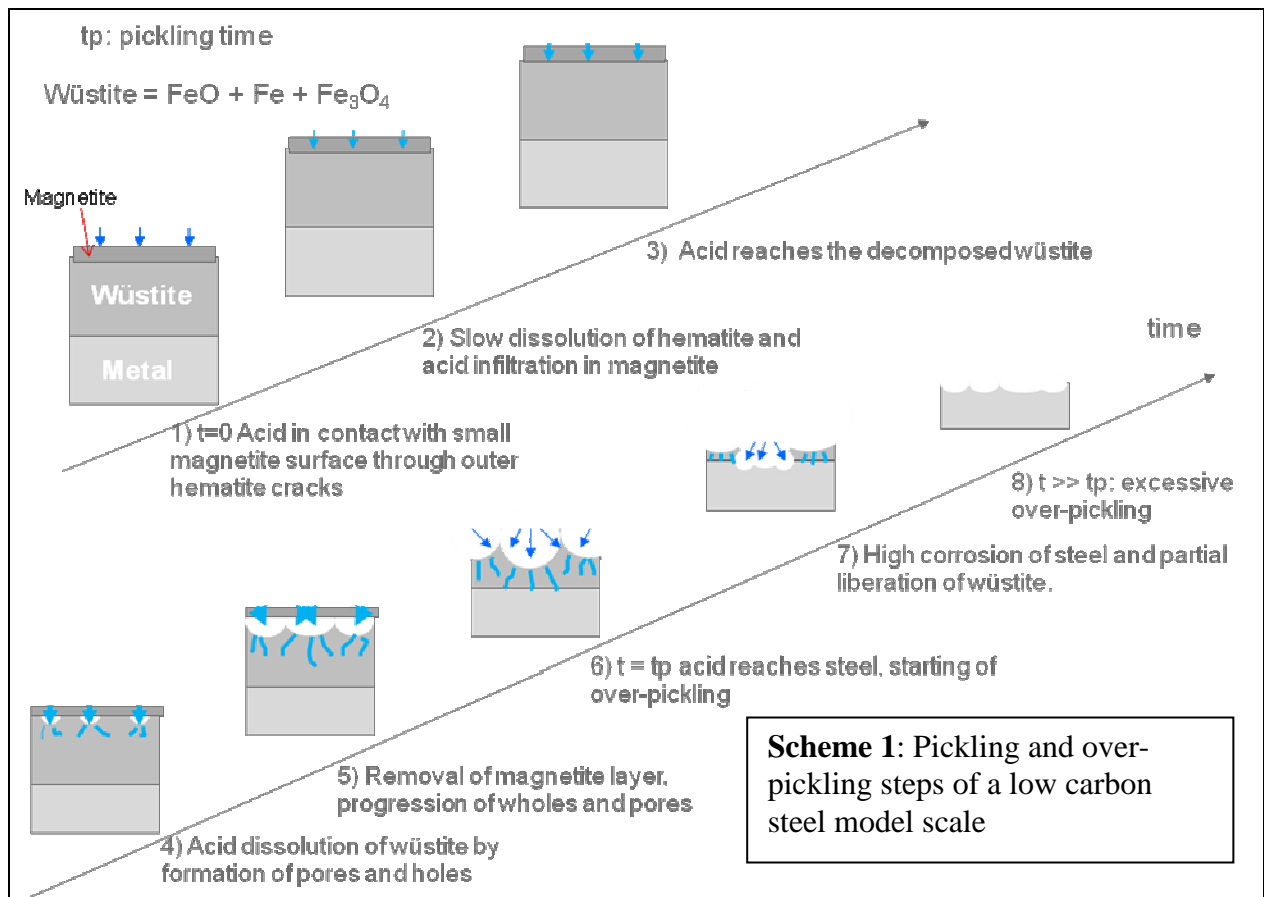
the resulting scale was discontinuous with islands composed of a wüstite external layer and an internal layer composed of grains of fayalite in wüstite matrix surrounded by a silica layer.

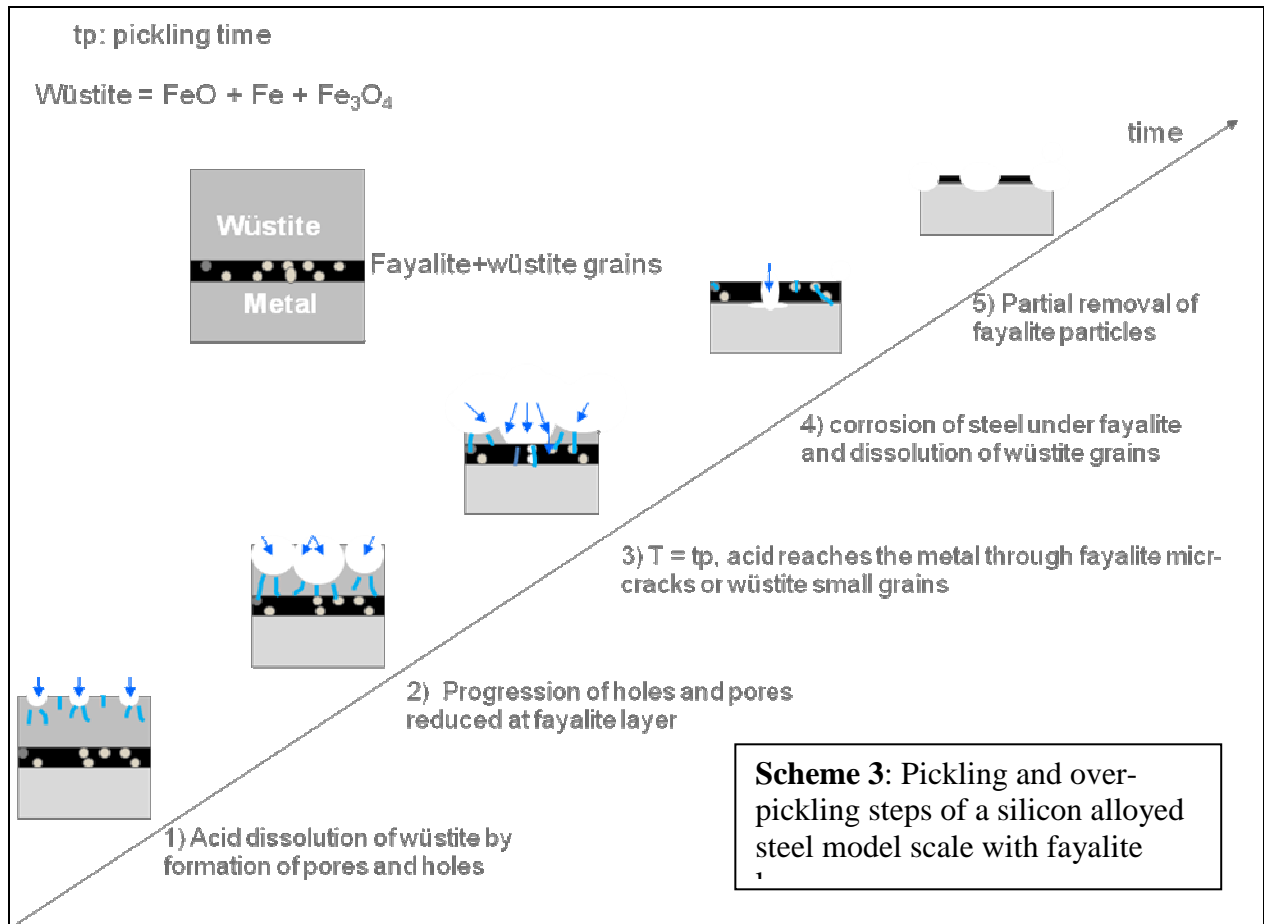
In the second part of this work, the pickling and over-pickling kinetics and reactions were followed for three model scale samples obtained at 850°C for the low carbon steel and at 1100°C and 1200°C for the silicon alloyed steel. A hematite very thin outer layer was present at the surface of the low carbon steel model scale only while wüstite and magnetite were common phases for all samples. Fayalite was present in the internal layer of silicon alloyed samples as grains or continuous layer after oxidation at 1100°C and 1200°C respectively. Industrial scales of similar steel grades were also studied. The electrolyte used was 1 M in HCl (instead of 3M in industrial conditions) and the temperature was 20°C (instead of 80-90°C) in order to allow electrochemical measurements in a reasonable time scale.

Pickling and over-pickling mechanisms in the literature were limited to low carbon steels and were deduced from open circuit potential values and microscopic observations of scales at different stages of pickling. Accordingly the open circuit potential was positive and stable during scale dissolution and dropped significantly when the acid reached the steel substrate. It is usually admitted that dissolution of the insulating scale is mainly chemical, though a well defined open-circuit potential can be measured from the beginning of immersion in the pickling solution, indicating an electrochemical contribution from the beginning. To the best of our knowledge, it is the first time that electrochemical dissolution rates are measured *in situ* during the whole pickling process, using potentiodynamic and impedance measurements.

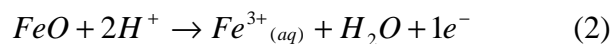
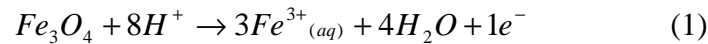
In this study, combination of different electrochemical and real time quantification methods, and the interpretation and correlation of the different results lead to richer and more accurate description of pickling mechanisms of representative models for industrial scales. The corrosion potential values could be associated with well identified electrochemical reactions and the combination of ICP-AES and corrosion current gave an estimation of the contribution of electrochemical dissolution during pickling and over-pickling.

From the different experiments, the following mechanisms were suggested:

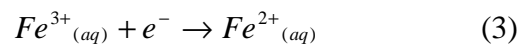




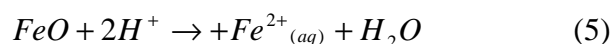
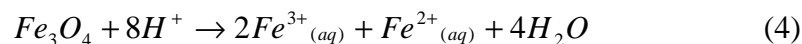
Before the acid reached the steel substrate, simultaneously with the slow dissolution of hematite, the main anodic reactions was the oxidations of magnetite (1) and wüstite (2)



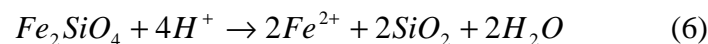
and the main cathodic reaction was the reduction of ferric ions (3) formed by chemical dissolution of magnetite (4).



The chemical dissolution of magnetite (4) and wüstite (5) is maintained



Chemical dissolution of fayalite can be also considered, but this reaction is very slow comparatively to the time of pickling experiments performed in this work:



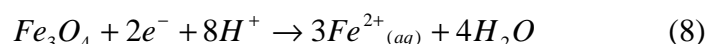
During this phase the protons are not reduced into H₂ on iron oxides but they are consumed by the oxides dissolution according to reactions (1), (2), (4), (5) and (6).

The external scale layers composed essentially of the decomposed wüstite were dissolved following the same mechanism for low carbon steel by holes widening and removal of particles. The fayalite grains in the internal layer were mechanically detached in the solution by dissolution of the wüstite matrix. The fayalite layer was infiltrated slowly by the acid through micro-cracks or wüstite small grains and detached in the solution simultaneously with dissolution of the steel substrate.

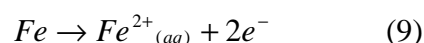
Iron oxide phases of silicon alloyed steel model scales were crossed by the acid faster than model scale of the low carbon steel, even though the latter had higher thickness. This was attributed to a more fragile structure or wüstite decomposition due to the formation of fayalite grains or internal layer

A noticeable result in this work was to show the key role played by ferric ions formed in the pickling bath by chemical dissolution of hematite and magnetite. They provide the species for cathodic reaction enabling anodic dissolution of the scale, in a potential range in which protons are not reduced.

After the acid reached the steel substrate, the proton (7) and magnetite (8) reductions were assumed to be the main cathodic reactions,



whereas the oxidation of the iron substrate (9) was the main anodic reaction.



The protons reduction occurred only on the steel substrate. The reduction of ferric into ferrous ions must then become negligible, since the rate of chemical dissolution of iron oxide is significantly lowered in comparison with the electrochemical dissolution.

The presence of fayalite as grains or thin layer at steel/scale interface had an effect on the continuous scale dissolution after the acid reached the steel substrate. Indeed, the continuous reduction of magnetite and the low steel substrate surface available for protons reduction due to fayalite covering was responsible for the cathodic intermediate potential after the jump.

A dissolution peak was observed when the acid reached the steel substrate, simultaneously with the significant potential jump. The electrochemical dissolution becomes

dominant at bare steel corrosion potential. This means that the cathodic potential indirectly blocks the chemical reaction. The rest of scale is removed in form of particles.

Electrochemical impedance spectroscopy (EIS) was used for the first time as a method to follow scale dissolution and gave more information on scale characteristics at different pickling and over-pickling times. According to EIS results, scale was described with an electrochemical model composed of a Constant Phase Element (CPE) in parallel with a charge transfer resistance. The capacitance of the insulating hematite outer layer was estimated by a Power-Law model, while a double layer capacitance was measured on the conductive magnetite and decomposed wüstite. This double layer capacitance was estimated by Brug's model and their huge values allowed estimating the real active surface of the porous oxide.

The high corrosion current values calculated by a Tafel method confirmed the porous electrode behaviour during dissolution of the decomposed wüstite observed with EIS.

The Tafel and EIS methods gave compatible results for the evolution of the corrosion current and the active surface but the EIS seems more appropriate since its perturbation of the solid/solution interface is very weak. It is well adapted for in situ studies of slow corrosion processes like pickling in soft conditions.

Pickling is accelerated by many parameters. They are ranked by their effect on the decrease of pickling time as follows: pH decrease, temperature increase, cathodic potential and scale cracking. The cathodic potential application is the most efficient parameter to accelerate pickling and protect the metal from corrosion at the same time.

For the scale model, the potential drop occurs simultaneously with the dissolution peak corresponding to a high dissolution rate of iron from the substrate at the transition time. While industrial scales are thinner and cracked, the negative corrosion potential and the dissolution peak are observed immediately at the beginning of pickling, this means that over-pickling starts simultaneously with pickling and the major part of scale is removed with over-pickling. The use of electrochemical methods to deal with the low soluble fayalite and its infiltrations can therefore be a good perspective for optimisation of pickling of silicon steels.

Annexes

Annex I

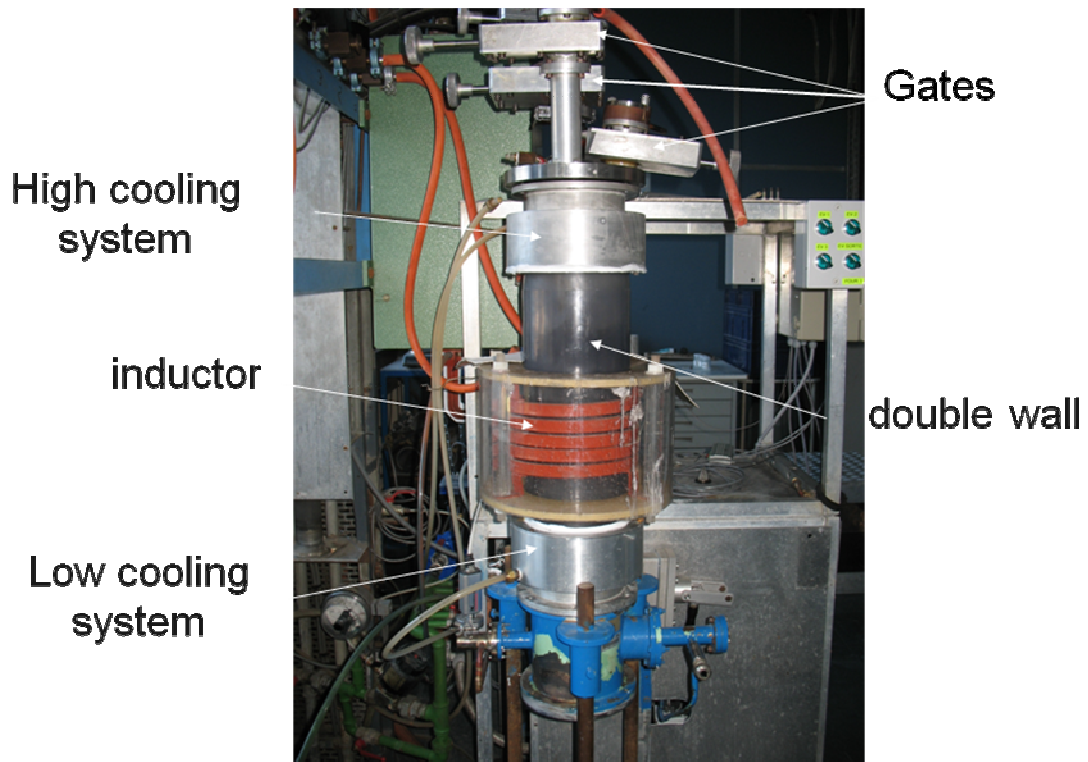
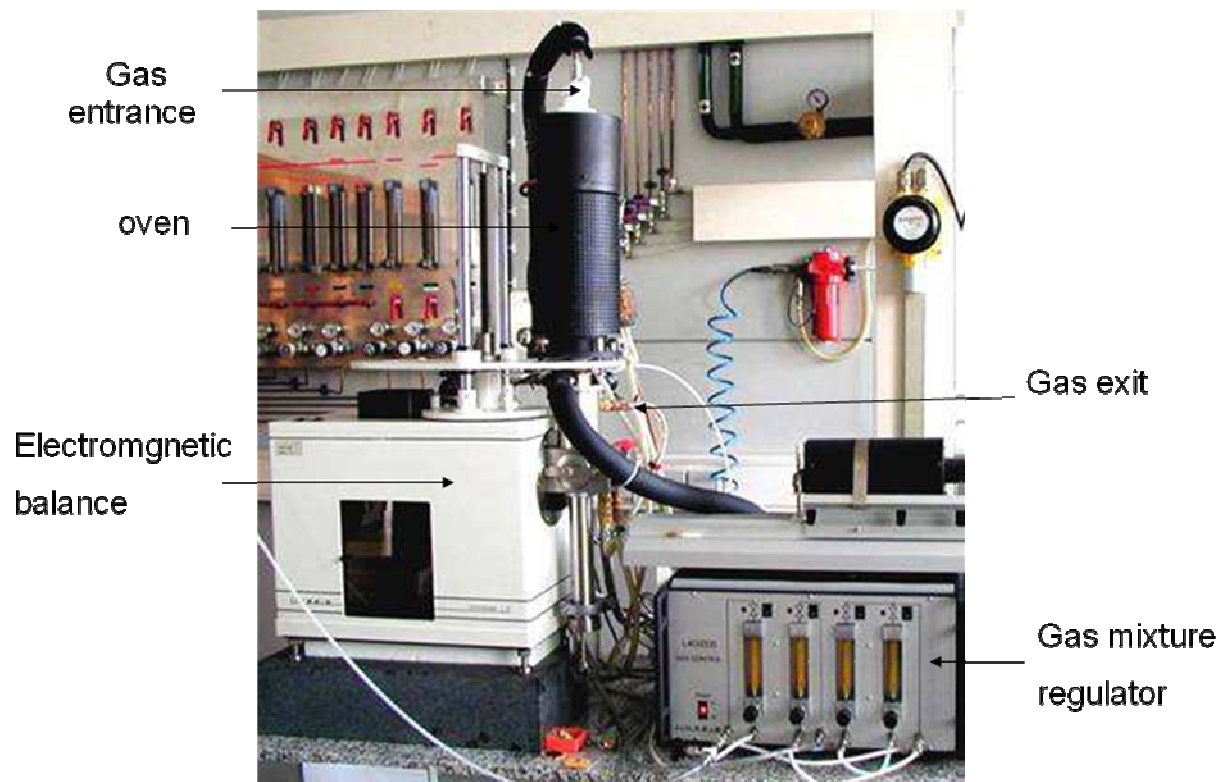


Photo of the 1 kg induction furnace before the heating experiment



Photo of the 1 kg induction furnace during the metallic charge melting (yellow to orange light)

Annex II



Thermogravimetric analyzer set-up

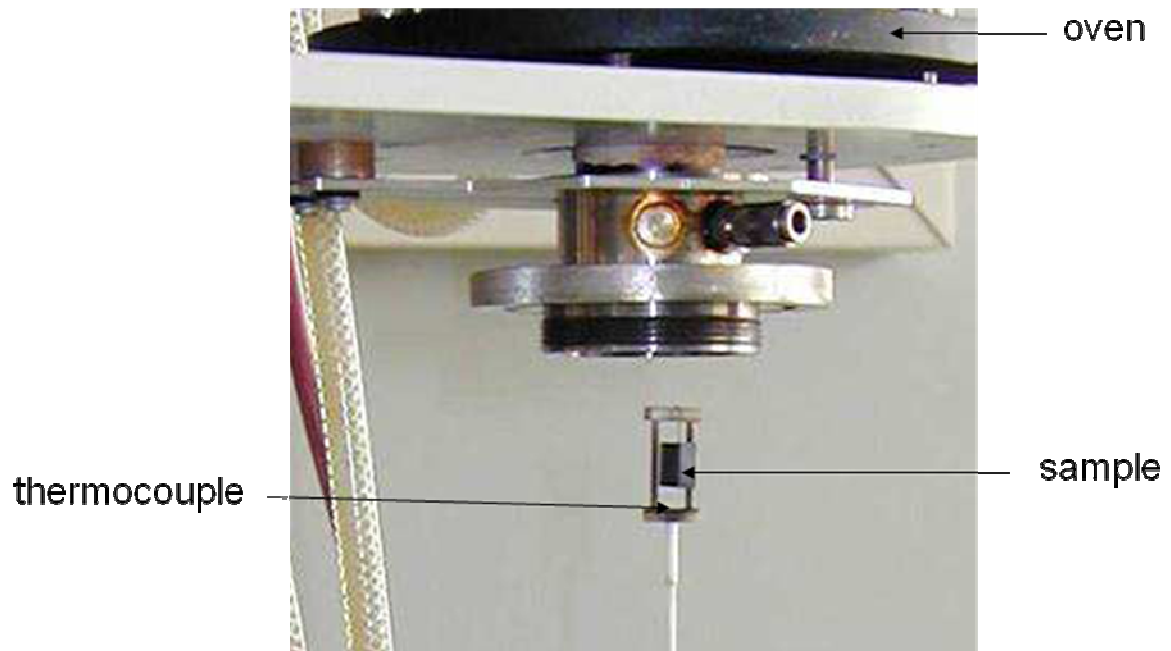
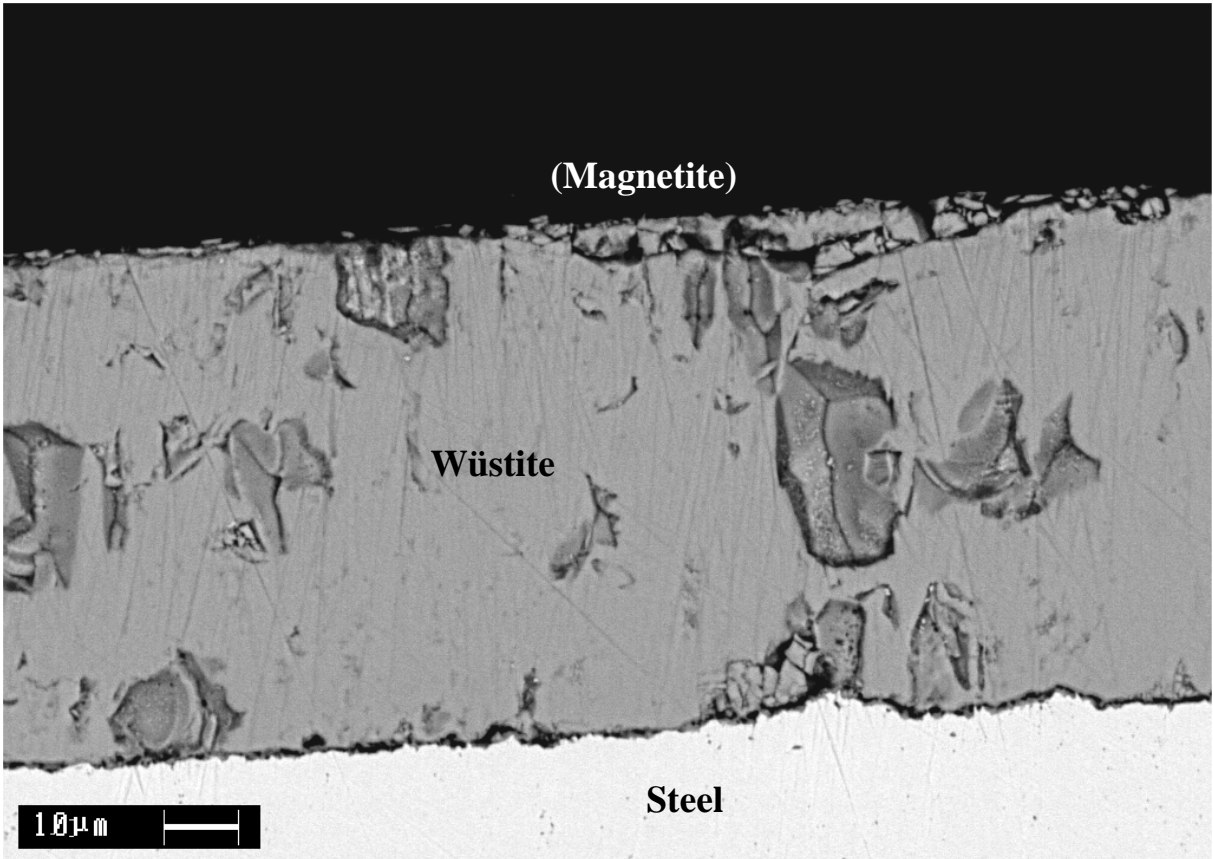


Photo of the thermogravimetric analyser sample holder

Annex III



Cross-section SEM micrograph of the Si00 steel sample after oxidation at 850°C in air with 15% relative humidity during 15 minute then few seconds of polishing to remove the hematite outer layer.

References

- [1] E. Ahtoy, Effect of alloying elements (Si, P, Al, B) on low carbon steel oxidation in process at high temperatures: mechanisms and modelling, Université de Grenoble Thesis, 2010.
- [2] M. Picard, Oxidation of Steel, ArcelorMittal Internal Document, 2010.
- [3] K.-T. Park, Y.-S. Kim, J.G. Lee, D.H. Shin, Thermal stability and mechanical properties of ultrafine grained low carbon steel, *Materials Science and Engineering: A*, 293 (2000) 165-172.
- [4] N. Tsuji, R. Ueji, Y. Minamino, Y. Saito, A new and simple process to obtain nano-structured bulk low-carbon steel with superior mechanical property, *Scripta Materialia*, 46 (2002) 305-310.
- [5] L. Holappa, V. Ollilainen, W. Kasprzak, The effect of silicon and vanadium alloying on the microstructure of air cooled forged HSLA steels, *Journal of Materials Processing Technology*, 109 (2001) 78-82.
- [6] V. Ollilainen, W. Kasprzak, L. Holappa, The effect of silicon, vanadium and nitrogen on the microstructure and hardness of air cooled medium carbon low alloy steels, *Journal of materials processing technology*, 134 (2003) 405-412.
- [7] H.-W. Hsu, W.-T. Tsai, High temperature corrosion behavior of siliconized 310 stainless steel, *Materials chemistry and physics*, 64 (2000) 147-155.
- [8] S. Giordana, C. Fiaud, Corrosion behaviour of low-Si alloyed steels in neutral reducing conditions at 90° C, *Electrochimica acta*, 47 (2002) 1683-1689.
- [9] T. Ros-Yanez, Y. Houbaert, O. Fischer, J. Schneider, Production of high silicon steel for electrical applications by thermomechanical processing, *Journal of materials processing technology*, 143 (2003) 916-921.
- [10] F. Galdon, Aspects fondamentaux de l'oxydation du fer et des aciers, in: *LES CAHIERS DU CESSID - LE DÉCAPAGE DES PRODUITS PLATS*, IRSID, 1983.
- [11] M. Picard, La calamine fine et adhérente, ArcelorMittal Internal Document, 2010.
- [12] R. Chen, W. Yuen, Oxidation of low-carbon, low-silicon mild steel at 450–900 C under conditions relevant to hot-strip processing, *Oxidation of Metals*, 57 (2002) 53-79.
- [13] H. Utsunomiya, S. Doi, K.-i. Hara, T. Sakai, S. Yanagi, Deformation of oxide scale on steel surface during hot rolling, *CIRP Annals-Manufacturing Technology*, 58 (2009) 271-274.
- [14] Q. Zhu, H. Zhu, A. Tieu, M. Reid, L. Zhang, In-situ investigation of oxidation behaviour in high-speed steel roll material under dry and humid atmospheres, *Corrosion Science*, 52 (2010) 2707-2715.
- [15] E. Ahtoy, Study of Alloying Element Effect Silicon and Manganese, Arcelor Internship report, 2007.
- [16] P. Sarrazin, J. Fouletier, A. Galerie, Les mécanismes de la corrosion sèche: une approche cinétique, *SOFEDIS*, 2012.
- [17] U. Evans, The oxidation of metals, *Rev. Pure and Appl. Chem*, 5 (1955) 1.
- [18] P. Kofstad, D.M. Etherington, B. Boucher, *High temperature corrosion*, Elsevier applied science London, 1988.
- [19] R. Chen, W. Yeun, Review of the high-temperature oxidation of iron and carbon steels in air or oxygen, *Oxidation of Metals*, 59 (2003) 433-468.
- [20] R.Y. Chen, W. Yuen, Oxidation of Low-Carbon Steel in 17 H₂O N₂ at 900° C, *Metallurgical and Materials Transactions A*, 40 (2009) 3091-3107.
- [21] R.Y. Chen, W.Y. Yuen, Short-time Oxidation Behavior of Low-carbon, Low-silicon Steel in Air at 850–1,180° C—I: Oxidation Kinetics, *Oxidation of Metals*, 70 (2008) 39-68.

- [22] S. Mrowec, A. Stokłosa, Calculations of parabolic rate constants for metal oxidation, *Oxidation of Metals*, 8 (1974) 379-391.
- [23] J. Paidassi, Sur la cinétique de l'oxydation du fer dans l'air dans l'intervalle 700–1250° C, *Acta Metallurgica*, 6 (1958) 184-194.
- [24] A. Talekar, D. Chandra, R. Chellappa, J. Daemen, N. Tamura, M. Kunz, Oxidation kinetics of high strength low alloy steels at elevated temperatures, *Corrosion Science*, 50 (2008) 2804-2815.
- [25] C. Tuck, M. Odgers, K. Sachs, The oxidation of iron at 950 C in oxygen/water vapour mixtures, *Corrosion Science*, 9 (1969) 271-285.
- [26] J. Baud, A. Ferrier, J. Manenc, J. Bénard, The oxidation and decarburizing of Fe-C alloys in air and the influence of relative humidity, *Oxidation of Metals*, 9 (1975) 69-97.
- [27] J. Bénard, *Oxydation des métaux*, Guathier-Villars, 1962.
- [28] J. Bénard, J. Bardolle, *L'oxydation des métaux*, Gauthier-Villars, 1964.
- [29] S. Hallström, L. Höglund, J. Ågren, Modeling of iron diffusion in the iron oxides magnetite and hematite with variable stoichiometry, *Acta Materialia*, 59 (2011) 53-60.
- [30] L. Himmel, R. Mehl, C. Birchenall, Self diffusion of iron in iron oxides and the Wagner theory of oxidation, *Trans. AIME*, 197 (1953) 827.
- [31] Y. Sayadyaghoubi, S. Sun, S. Jahanshahi, Determination of the chemical diffusion of oxygen in liquid iron oxide at 1615 °C, *Metallurgical and Materials Transactions B*, 26 (1995) 795-802.
- [32] Y. Li, R.J. Fruehan, J.A. Lucas, G.R. Belton, The chemical diffusivity of oxygen in liquid iron oxide and a calcium ferrite, *Metallurgical and Materials Transactions B*, 31 (2000) 1059-1068.
- [33] C. Tuck, Non-protective and protective scaling of a commercial 1¾% silicon-iron alloy in the range 800 C-1000 C, *Corrosion Science*, 5 (1965) 631-643.
- [34] I. Svedung, N.G. Vannerberg, The influence of silicon on the oxidation properties of iron, *Corrosion Science*, 14 (1974) 391-399.
- [35] A. Atkinson, A theoretical analysis of the oxidation of Fe-Si alloys, *Corrosion Science*, 22 (1982) 87-102.
- [36] T. Adachi, G. Meier, Oxidation of iron-silicon alloys, *Oxidation of Metals*, 27 (1987) 347-366.
- [37] S. Basu, G. Yurek, Effect of alloy grain size and silicon content on the oxidation of austenitic Fe-Cr-Ni-Mn-Si alloys in pure O₂, *Oxidation of Metals*, 36 (1991) 281-315.
- [38] S.-A. Lin, J.-T. Lee, W.-T. Tsai, Microstructural aspects and oxidation behavior of laser surface clad silicon-containing stainless steels, *Scripta Materialia*, 38 (1998) 559-563.
- [39] M. Fukumoto, S. Maeda, S. Hayashi, T. Narita, Effect of Water Vapor on the Oxidation Behavior of Fe–1.5 Si in Air at 1073 and 1273 K, *Oxidation of Metals*, 55 (2001) 401-422.
- [40] A.-R. Lashin, O. Schneeweiss, Y. Houbaert, Effect of ambient air pressure on the oxidation kinetics of Fe–6at.% Si alloy, *Corrosion Science*, 50 (2008) 2580-2587.
- [41] Y.-L. Yang, C.-H. Yang, S.-N. Lin, C.-H. Chen, W.-T. Tsai, Effects of Si and its content on the scale formation on hot-rolled steel strips, *Materials Chemistry and Physics*, 112 (2008) 566-571.
- [42] F. Velasco, A. Bautista, A. González-Centeno, High-temperature oxidation and aqueous corrosion performance of ferritic, vacuum-sintered stainless steels prealloyed with Si, *Corrosion Science*, 51 (2009) 21-27.
- [43] L. Suárez, P. Rodríguez-Calvillo, Y. Houbaert, R. Colás, Oxidation of ultra low carbon and silicon bearing steels, *Corrosion Science*, 52 (2010) 2044-2049.
- [44] S. Saunders, M. Monteiro, F. Rizzo, The oxidation behaviour of metals and alloys at high temperatures in atmospheres containing water vapour: A review, *Progress in Materials Science*, 53 (2008) 775-837.

- [45] A. Atkinson, J. Gardner, The diffusion of Fe^{3+} in amorphous SiO_2 and the protective properties of SiO_2 layers, *Corrosion Science*, 21 (1981) 49-58.
- [46] K. Muehlenbachs, H. Schaeffer, Oxygen diffusion in vitreous silica; utilization of natural isotopic abundances, *The Canadian Mineralogist*, 15 (1977) 179-184.
- [47] E.W. Sufov, Diffusion of oxygen in vitreous silica, *Journal of the American Ceramic Society*, 46 (1963) 14-20.
- [48] C. Wagner, Theoretical analysis of the diffusion processes determining the oxidation rate of alloys, *Journal of the electrochemical Society*, 99 (1952) 369-380.
- [49] R.Y. Chen, W. Yuen, Oxidation of a Low Carbon, Low Silicon Steel in Air at 600-920°C, in: *Materials science forum*, Trans Tech Publ, 2006, pp. 77-86.
- [50] L. Darken, Melting points of iron oxides on silica; Phase equilibria in the system Fe-Si-O as a function of gas composition and temperature, *Journal of the American Chemical Society*, 70 (1948) 2046-2053.
- [51] D. Genève, Etude physico-chimique superficielle de l'oxydation de l'acier. Influence des éléments résiduels (cuivre, nickel, étain,...) sur l'adhérence de la couche d'oxyde, Institut National Polytechnique de Lorraine Thesis, 1996.
- [52] P. Wang, Y. Feng, W. Roth, J. Corbett, Diffusion behavior of implanted iron in fused silica glass, *Journal of non-crystalline solids*, 104 (1988) 81-84.
- [53] L. Yang, C.Y. Chien, G. Derge, Self-Diffusion of Iron in Iron Silicate Melt, *The Journal of Chemical Physics*, 30 (1959) 1627-1627.
- [54] E.M. Levin, C.R. Robbins, H.F. MacMurdie, K. Reser, N.b.o. standards, A.C. Society, NBS., *Phase Diagrams for Ceramists*, 1969.
- [55] J. Baud, A. Ferrier, J. Manenc, Study of magnetite film formation at metal-scale interface during cooling of steel products, *Oxidation of Metals*, 12 (1978) 331-342.
- [56] D. Quantin, J. Becot, Caractéristiques des calamines de tôles à chaud, in: *LES CAHIERS DU CESSID - LE DÉCAPAGE DES PRODUITS PLATS*, IRSID, 1983.
- [57] H. Abuluwefa, R. Guthrie, J. Root, F. Ajersch, Real-time observations of the oxidation of mild steel at high temperature by neutron diffraction, *Metallurgical and Materials Transactions B*, 27 (1996) 993-997.
- [58] R. Chen, W. Yuen, A study of the scale structure of hot-rolled steel strip by simulated coiling and cooling, *Oxidation of Metals*, 53 (2000) 539-560.
- [59] R. Chen, W. Yuen, Examination of oxide scales of hot rolled steel products, *ISIJ international*, 45 (2005) 52-59.
- [60] H. Bolt, *The Properties of Oxide Scales on Hot Rolled Steels: A Literature Review*, Corus Research, Development & Technology, Ijmuiden Technology Centre, (2000).
- [61] P.H. Bolt, Understanding the properties of oxide scales on hot rolled steel strip, *Steel research international*, 75 (2004) 399-404.
- [62] L. Chang, S.N. Lin, Analytical electron microscopy study of interfacial oxides formed on a hot-rolled low-carbon steel, *Oxidation of Metals*, 63 (2005) 131-144.
- [63] W.M.C. Melfo, Analysis of hot rolling events that lead to ridge-buckle defect in steel strips, University of Wollongong Thesis, 2006.
- [64] P. Schmuki, M. Büchler, S. Virtanen, H. Böhni, R. Müller, L. Gauckler, Bulk metal oxides as a model for the electronic properties of passive films, *Journal of the Electrochemical Society*, 142 (1995) 3336-3342.
- [65] M. Büchler, P. Schmuki, H. Böhni, T. Stenberg, T. Mäntylä, Comparison of the Semiconductive Properties of Sputter-Deposited Iron Oxides with the Passive Film on Iron, *Journal of The Electrochemical Society*, 145 (1998) 378-385.
- [66] S. Virtanen, P. Schmuki, H. Böhni, P. Vuoristo, T. Mäntylä, Artificial Cr-and Fe-Oxide Passive Layers Prepared by Sputter Deposition, *Journal of the Electrochemical Society*, 142 (1995) 3067-3972.

- [67] R.M. Cornell, U. Schwertmann, The iron oxides: structure, properties, reactions, occurrences and uses, Wiley-vch, 2003.
- [68] D.S. Tannhauser, Conductivity in iron oxides, Journal of Physics and Chemistry of Solids, 23 (1962) 25-34.
- [69] J. Wielant, V. Goossens, R. Hausbrand, H. Terryn, Electronic properties of thermally formed thin iron oxide films, Electrochimica Acta, 52 (2007) 7617-7625.
- [70] R. Higginson, B. Roebuck, E. Palmiere, Texture development in oxide scales on steel substrates, Scripta materialia, 47 (2002) 337-342.
- [71] S. Taniguchi, K. Yamamoto, D. Megumi, T. Shibata, Characteristics of scale/substrate interface area of Si-containing low-carbon steels at high temperatures, Materials Science and Engineering: A, 308 (2001) 250-257.
- [72] S. Lecourt, Décapage, in: Le livre de l'acier, 1997.
- [73] M. WERY, Décapage des métaux, Techniques de l'ingénieur. Matériaux métalliques, (2001) M1455. 1451-M1455. 1456.
- [74] S. Jacques, Bibliographic report on pickling of alloyed steels (AHSS) and corrosion inhibition, ArcelorMittal Internal Document, 2009.
- [75] F. Kop, R. Nicolle, C. Allely, Pickling productivity, Revue de Métallurgie, 100 (2003) 993-1001.
- [76] G. Zaparty, Décapage des aciers plats au carbone, Arcelor internship report, 2003.
- [77] S. Yamaguchi, T. Yoshida, T. Saito, IMPROVEMENT IN DESCALING OF HOT STRIP BY HYDROCHLORIC ACID, ISIJ international, 34 (1994) 670-678.
- [78] P. Desjardins, Phénomènes physico-chimiques au décapage, in: LES CAHIERS DU CESSID – LAMINAGE DES ACIERS, IRSID, 1983.
- [79] M. Gines, G. Benitez, T. Perez, E. Merli, M. Firpo, W. Egli, Study of the picklability of 1.8 mm hot-rolled steel strip in hydrochloric acid, Latin American applied research, 32 (2002) 281-288.
- [80] D. Quantin, Aspects généraux de l'influence des caractéristiques des calamines sur leur décapabilité, in: LES CAHIERS DU CESSID - LE DÉCAPAGE DES PRODUITS PLATS, IRSID, 1983.
- [81] C. Tuck, The effect of scale microstructure on the pickling of hot-rolled steel strip, Anti-Corrosion Methods and Materials, 16 (1969) 22-27.
- [82] D. Quantin, Fissuration des calamines en vue d'améliorer le décapage, in: LES CAHIERS DU CESSID - LE DÉCAPAGE DES PRODUITS PLATS, IRSID, 1983.
- [83] W.F. Leite, D.B. Santos, Dissolução de Óxidos Formados a Altas Temperaturas nos Aços Elétricos Variando-se a Temperatura e Concentração da Solução Ácida na Decapagem, UNIVERSIDADE FEDERAL DE MINAS GERAIS, 2008.
- [84] B. Gaur, T.B. Singh, D.D.N. Singh, Beneficial Role of Chloride Ions During Pickling of Steel in Sulfuric Acid, Corrosion, 52 (1996) 154-159.
- [85] C. Fiaud, R. Chahroui, Les inhibiteurs de corrosion, Proc. 8th. Int. Cong. Metall. Corr., Mainz, 1 (1981) 18.
- [86] B. Goode, R. Jones, J. Howells, Kinetics of pickling of low carbon steel, Ironmaking & steelmaking, 23 (1996) 164-170.
- [87] P. Kittisupakorn, P. Thitiyasook, M.A. Hussain, W. Daosud, Neural network based model predictive control for a steel pickling process, Journal of Process Control, 19 (2009) 579-590.
- [88] J. Baud, A. Ferrier, Etudes expérimentales du décapage sulfurique et du décapage chlorhydrique en fonction de la nature des calamines à enlever, in: Internal Documents, ArcelorMittal 1980.

- [89] D. Quantin, Mécanisme et caractéristiques des calamines en liaison avec leur décapabilité, in: LES CAHIERS DU CESSID - LE DÉCAPAGE DES PRODUITS PLATS, IRSID, 1983.
- [90] M. WERY, Décapage chimique des surfaces métalliques, Techniques de l'ingénieur. Matériaux métalliques, (2001) M1456. 1451-M1456. 1416.
- [91] W. Bullough, PICKLING, DESCALING, AND DERUSTING OF STEELS, International Materials Reviews, 2 (1957) 391-406.
- [92] B. Migaud, Réflexions sur la dissolution électrochimique du protoxyde, in: LES CAHIERS DU CESSID - LE DÉCAPAGE DES PRODUITS PLATS, IRSID, 1983.
- [93] T. Kaiser, Fundamentals of hot mill scale and pickling, ArcelorMittal Internal Document.
- [94] P.D. Allen, N.A. Hampson, G.J. Bignold, The electrodisolution of magnetite: Part I. The electrochemistry of Fe₃O₄/C discs-potentiodynamic experiments, Journal of Electroanalytical Chemistry and Interfacial Electrochemistry, 99 (1979) 299-309.
- [95] P.D. Allen, N.A. Hampson, G.J. Bignold, The electrodisolution of magnetite: Part II. The oxidation of bulk magnetite, Journal of Electroanalytical Chemistry and Interfacial Electrochemistry, 111 (1980) 223-233.
- [96] P. Sidhu, R. Gilkes, R. Cornell, A. Posner, J. Quirk, Dissolution of iron oxides and oxyhydroxides in hydrochloric and perchloric acids, Clays and Clay Minerals, 29 (1981) 269-276.
- [97] E. Baumgartner, M. Blesa, H. Marinovich, A. Maroto, Heterogeneous electron transfer as a pathway in the dissolution of magnetite in oxalic acid solutions, Inorganic Chemistry, 22 (1983) 2224-2226.
- [98] W.W. Frenier, F.B. Growcock, Mechanism of iron oxide dissolution-A review of recent literature, Corrosion, 40 (1984) 663-668.
- [99] M.A. Blesa, H.A. Marinovich, E.C. Baumgartner, A.J. Maroto, Mechanism of dissolution of magnetite by oxalic acid-ferrous ion solutions, Inorganic Chemistry, 26 (1987) 3713-3717.
- [100] P. Schmuki, S. Virtanen, A.J. Davenport, C.M. Vitus, In Situ X-Ray Absorption Near-Edge Spectroscopic Study of the Cathodic Reduction of Artificial Iron Oxide Passive Films, Journal of the Electrochemical Society, 143 (1996) 574-582.
- [101] S. Virtanen, P. Schmuki, A.J. Davenport, C.M. Vitus, Dissolution of Thin Iron Oxide Films Used as Models for Iron Passive Films Studied by In Situ X-Ray Absorption Near-Edge Spectroscopy, Journal of the Electrochemical Society, 144 (1997) 198-204.
- [102] V.B. Fetisov, A.N. Ermakov, G.M. Belysheva, A.V. Fetisov, V.M. Kamyshev, K.Z. Brainina, Electrochemical dissolution of magnetite in acid solutions, Journal of Solid State Electrochemistry, 8 (2004) 565-571.
- [103] B. Osdoit, Le décapage des tôles d'acier au silicium, in: LES CAHIERS DU CESSID - LE DÉCAPAGE DES PRODUITS PLATS, IRSID, 1983.
- [104] N. Asrar, C. Thakur, Pickling silicon steels in mixed acid solutions, Met. Finish.(USA), 93 (1995) 70-72.
- [105] A. Chattopadhyay, N. Bandyopadhyay, A. Das, M. Panigrahi, Oxide scale characterization of hot rolled coils by Raman spectroscopy technique, Scripta materialia, 52 (2005) 211-215.
- [106] Y.N. Chang, Roles of silicon and aluminium in pickling behaviour of low alloy hot rolled steel, British Corrosion Journal, 29 (1994) 136-139.
- [107] C. Lefrou, P. Fabry, J.C. Poignet, L'électrochimie: Fondamentaux avec exercices corrigés, EDP sciences, 2009.
- [108] B. Hirschorn, M.E. Orazem, B. Tribollet, V. Vivier, I. Frateur, M. Musiani, Constant-Phase-Element Behavior Caused by Resistivity Distributions in Films I. Theory, Journal of The Electrochemical Society, 157 (2010) C452-C457.

- [109] B. Hirschorn, M.E. Orazem, B. Tribollet, V. Vivier, I. Frateur, M. Musiani, Constant-Phase-Element Behavior Caused by Resistivity Distributions in Films II. Applications, *Journal of The Electrochemical Society*, 157 (2010) C458-C463.
- [110] M.E. Orazem, I. Frateur, B. Tribollet, V. Vivier, S. Marcelin, N. Pébère, A.L. Bunge, E.A. White, D.P. Riemer, M. Musiani, Dielectric properties of materials showing constant-phase-element (CPE) impedance response, *Journal of The Electrochemical Society*, 160 (2013) C215-C225.
- [111] M.E. Orazem, B. Tribollet, *Electrochemical impedance spectroscopy*, Wiley-Interscience, 2011.
- [112] B. Hirschorn, M.E. Orazem, B. Tribollet, V. Vivier, I. Frateur, M. Musiani, Determination of effective capacitance and film thickness from constant-phase-element parameters, *Electrochimica Acta*, 55 (2010) 6218-6227.
- [113] G. Brug, A. Van Den Eeden, M. Sluyters-Rehbach, J. Sluyters, The analysis of electrode impedances complicated by the presence of a constant phase element, *Journal of electroanalytical chemistry and interfacial electrochemistry*, 176 (1984) 275-295.
- [114] D. Hamm, K. Ogle, C.-O. Olsson, S. Weber, D. Landolt, Passivation of Fe–Cr alloys studied with ICP-AES and EQCM, *Corrosion science*, 44 (2002) 1443-1456.
- [115] K. Ogle, A. Tomandl, N. Meddahi, M. Wolpers, The alkaline stability of phosphate coatings I: ICP atomic emission spectroelectrochemistry, *Corrosion science*, 46 (2004) 979-995.
- [116] K. Ogle, S. Weber, Anodic dissolution of 304 stainless steel using atomic emission spectroelectrochemistry, *Journal of the Electrochemical Society*, 147 (2000) 1770-1780.
- [117] M. Danielewski, *Kinetics of gaseous corrosion processes*, Materials Park, (2003).
- [118] D. Genève, Etude physico-chimique superficielle de l'oxydation de l'acier. Influence des éléments résiduels (cuivre, nickel, étain,...) sur l'adhérence de la couche d'oxyde, Institut National Polytechnique de Lorraine Thesis Collection, (1996).
- [119] M. Hanesch, Raman spectroscopy of iron oxides and (oxy) hydroxides at low laser power and possible applications in environmental magnetic studies, *Geophysical Journal International*, 177 (2009) 941-948.
- [120] A. Guedes, B. Valentim, A. Prieto, A. Sanz, D. Flores, F. Noronha, Characterization of fly ash from a power plant and surroundings by micro-Raman spectroscopy, *International Journal of Coal Geology*, 73 (2008) 359-370.
- [121] B. Kolesov, C. Geiger, A temperature-dependent single-crystal Raman spectroscopic study of fayalite: evidence for phonon-magnetic excitation coupling, *Physics and chemistry of minerals*, 31 (2004) 155-161.
- [122] C.D. Wagner, G.E. Muilenberg, *Handbook of x-ray photoelectron spectroscopy: a reference book of standard data for use in x-ray photoelectron spectroscopy*, Physical Electronics Division, Perkin-Elmer Corp., 1979.
- [123] H. Frederikse, Permittivity (Dielectric Constant) of Inorganic Solids, in: *CRC Handbook of Chemistry and Physics 2012-2013*, CRC press, 2012.
- [124] M. Pourbaix, *Atlas d'Equilibres Electrochimiques à 25°C*, Gauthier-Villars et Cie, Paris, 1963.

Résumé:

Les mécanismes d'oxydation, de décapage et sur-décapage d'un acier bas carbone et d'un acier fortement allié au silicium (1,6 et 3.2 % en masse de silicium) ont été étudiés. Le suivi de l'oxydation par thermogravimétrie et la caractérisation de la calamine des aciers fortement alliés au silicium a montré un effet très marquant de passivation de la couche de silice. Les calamines des échantillons modèles sont composées de couches d'hématite, magnétite et wüstite partiellement décomposée en fer et magnétite pour l'acier bas carbone. Pour l'acier au silicium, la fayalite est présente à l'interface acier/wüstite sous forme de grains ou d'une couche interne. Le suivi du potentiel de circuit ouvert pendant le décapage et sur-décapage de ces échantillons a montré un potentiel de corrosion stable et anodique pour les oxydes de fer et une chute drastique de ce potentiel au contact de l'acide avec le métal. Le suivi du taux de dissolution totale par ICP-AES combiné avec des mesures de courant de corrosion par la méthode de Tafel a montré une contribution importante de la dissolution électrochimique par oxydation de la wüstite et la magnétite et réduction de Fe^{3+} issu de la dissolution chimique de l'hématite et la magnétite. La fayalite est libérée dans la solution par dissolution de la wüstite ou du métal adjacents. Après le contact acide/métal, toutes les dissolutions sont exclusivement électrochimiques par corrosion du métal et réduction de la magnétite (cas des calamines industrielles). La spectroscopie d'impédance électrochimique a été utilisée pour la première fois pour ce type d'étude. L'estimation des valeurs de capacité a montré un comportement pseudo passif pour la couche d'hématite et d'électrode poreuse pour la wüstite.

Mots-clés :

Acier au silicium, oxydation, décapage et sur-décapage, ICP-AES, impédance

Abstract:

Oxidation, pickling and over-pickling mechanisms of a low carbon steel and a high alloyed steel (1.6 and 3.2 wt.% Si) were investigated. The monitoring of oxidation with thermogravimetry and characterization of scale showed a very important passivating effect of the silica layer. Model scales are composed of layers of hematite, magnetite and partially decomposed wüstite into iron and magnetite for the low carbon steel. For the silicon steel, fayalite is present in the steel/wüstite interface as grains or an internal layer. Open circuit potential measurements during pickling and over-pickling of these samples showed a stable and anodic corrosion potential for iron oxides and a significant potential jump once the acid reaches the metal. The monitoring of the total dissolution rate with ICP-AES coupled with corrosion current measurements with the Tafel method showed an important contribution of electrochemical dissolution by oxidation of wüstite and magnetite and reduction of Fe^{+3} from chemical dissolution of hematite. Fayalite is liberated in the solution by dissolution of the surrounding wüstite or metal. After the contact acid/metal, all dissolutions are exclusively electrochemical by corrosion of the metal and reduction of magnetite (case for industrial scales). Electrochemical impedance spectroscopy was used for the first time for this kind of studies. The estimation of the capacitance values showed a passive like behaviour for hematite and a porous electrode one for wüstite.

Key-words:

Silicon steels, oxidation, pickling, over-pickling, ICP-AES, impedance.